

Metal-line absorption around $z \approx 2.4$ star-forming galaxies in the Keck Baryonic Structure Survey*

Monica L. Turner,^{1†} Joop Schaye¹, Charles C. Steidel²,
Gwen C. Rudie³, and Allison L. Strom²

¹*Leiden Observatory, Leiden University, PO Box 9513, 2300 RA Leiden, The Netherlands*

²*California Institute of Technology, MS 249-17, Pasadena, CA 91125, USA*

³*Carnegie Observatories, 813 Santa Barbara Street, Pasadena, CA 91101, USA*

22 October 2021

ABSTRACT

We study metal absorption around 854 $z \approx 2.4$ star-forming galaxies taken from the Keck Baryonic Structure Survey (KBSS). The galaxies examined in this work lie in the fields of 15 hyper-luminous background QSOs, with galaxy impact parameters ranging from 35 proper kpc (pkpc) to 2 proper Mpc (pMpc). Using the pixel optical depth technique, we present the first galaxy-centred 2-D maps of the median absorption by OVI, NV, CIV, CIII, and SiIV, as well as updated results for HI. At small galactocentric radii we detect a strong enhancement of the absorption relative to randomly located regions that extend out to at least 180 pkpc in the transverse direction, and ± 240 km s⁻¹ along the line-of-sight (LOS, ~ 1 pMpc in the case of pure Hubble flow) for all ions except NV. For CIV (and HI) we detect a significant enhancement of the absorption signal out to 2 pMpc in the transverse direction, corresponding to the maximum impact parameter in our sample. After normalising the median absorption profiles to account for variations in line strengths and detection limits, in the transverse direction we find no evidence for a sharp drop-off in metals distinct from that of HI. We argue instead that non-detection of some metal line species in the extended circumgalactic medium is consistent with differences in the detection sensitivity. Along the LOS, the normalised profiles reveal that the enhancement in the absorption is more extended for OVI, CIV, and SiIV than for HI. We also present measurements of the scatter in the pixel optical depths, covering fractions, and equivalent widths as a function of projected galaxy distance. Limiting the sample to the 340 galaxies with redshifts measured from nebular emission lines does not decrease the extent of the enhancement along the LOS compared to that in the transverse direction. This rules out redshift errors as the source of the observed redshift-space anisotropy and thus implies that we have detected the signature of gas peculiar velocities from infall, outflows, or virial motions for HI, OVI, CIV, CIII, and SiIV.

Key words: intergalactic medium – quasars: absorption lines – galaxies: formation

1 INTRODUCTION

The exchange of baryons between galaxies and their surroundings remains a poorly understood problem in galaxy formation theory. Currently, hydrodynamical cosmological simulations suffer from large uncertainties in their implementations of sub-grid physics, particularly those related to feedback from star formation and active galactic nuclei

* Based on data obtained at the W.M. Keck Observatory, which is operated as a scientific partnership among the California Institute of Technology, the University of California, and NASA, and was made possible by the generous financial support of the W.M. Keck Foundation.

† E-mail: turnerm@strw.leidenuniv.nl

(AGN). Variations within these recipes can create vast differences in the resulting galaxy properties (e.g., Haas et al. 2013a,b), which manifest themselves also in the distribution of cosmic metals (e.g., Wiersma et al. 2011). Metals in different ionisation states hold clues to the structure, kinematics, temperature, and composition of the gas in which they reside, and they are therefore an important observational tool for comparison with simulations.

Observations have shown that the movements of these metals through the circumgalactic and intergalactic medium (CGM and IGM, respectively) are influenced by galactic-scale outflows, which are commonly observed in star-forming galaxies at $z \sim 2-3$ (e.g., Steidel et al. 1996; Pettini et al. 2000; Quider et al. 2009; Steidel et al. 2010); but also in nearby galaxies ($z < 2$) (e.g., Heckman et al. 1990, 2000; Martin 2005; Rupke et al. 2005; Tremonti et al. 2007; Weiner et al. 2009) as well as in those at higher redshifts (e.g., Franx et al. 1997; Steidel et al. 1999; Ajiki et al. 2002; Shapley et al. 2003; Jones et al. 2012). These outflows are often metal-rich, with velocities of up to 800–1000 km s⁻¹.

Aguirre et al. (2001), Oppenheimer & Davé (2008), and Oppenheimer et al. (2010) studied such winds in cosmological simulations, and found that they are likely responsible for metal pollution in the IGM. Furthermore, Oppenheimer et al. (2010) determined that these outflows are often bound to the galaxies and fall back in, with most star forming gas at $z \sim 1$ coming from such recycled material. Simulations by Booth et al. (2012) suggest that galaxies residing in low-mass ($M_{\text{tot}} < 10^{10} M_{\odot}$) haloes are required to account for the observed CIV absorption associated with relatively weak HI absorption (Schaye et al. 2003). However, Wiersma et al. (2010) found that only half of intergalactic metals originated from $M_{\text{tot}} \lesssim 10^{11} M_{\odot}$ haloes. The authors also noted that in their simulations, half of the intergalactic metals at $z = 2$ were ejected between $2 < z < 3$. This prediction is consistent with observations by Simcoe (2011) that suggested that 50% of metals observed in the IGM at $z \sim 2.4$ have been there since $z \sim 4.3$ (1.3 Gyrs). In general, many questions still remain about the masses of the galaxies responsible for metal pollution, as well as the epoch(s) at which the bulk of it may have occurred.

To search for intergalactic metals, observations of absorption-line systems are often used. Bahcall & Spitzer (1969) first suggested that intervening absorbers could be associated with galaxy haloes; indeed, it has been shown that MgII (e.g., Bergeron & Boissé 1991; Zibetti et al. 2005; Nielsen et al. 2013), CIV (e.g., Chen et al. 2001), and OVI (e.g., Stocke et al. 2006; Chen & Mulchaey 2009; Prochaska et al. 2011; Tumlinson et al. 2011) absorbers are found to occur near galaxies. Adelberger et al. (2003, 2005b) found evidence for metals out to 300 proper kpc using CIV-galaxy cross-correlation studies at $z \sim 3$, while Steidel et al. (2010) used galaxy pairs to observe the equivalent widths (EWs) of various ions near $\sim L_{*}$ galaxies at $z \sim 2-3$, galaxies, and showed that these galaxies have metal-enriched gas out to ~ 125 proper kpc.

Theoretical studies of metals around simulated galaxies have also been undertaken. For example, Ford et al. (2013)

examined the distribution of the absorption of various ions around $z = 0.25$ galaxies with halo masses $10^{11}-10^{13} M_{\odot}$, and found that all ions examined showed enhanced absorption near the galaxy centres, with lower ions arising in denser gas closer to the galaxies and higher ions found further away. A similar effect was seen by Shen et al. (2013), who analysed a zoom-in simulation of a $z \sim 3$, $\sim 10^{11} M_{\odot}$ galaxy. They found that low ions were predominantly tracing cool ($T < 10^5$ K) gas at radii less than the galaxy virial radius R_{vir} , while higher ions trace hotter gas out to beyond $2 \times R_{\text{vir}}$.

In this work, we study the distribution of metals around galaxies using data from the Keck Baryonic Structure Survey (KBSS, Rudie et al. 2012; Steidel et al. 2014). This survey consists of a combination of high-quality quasi-stellar object (QSO) spectra, and a survey focused on redshifts below those of the QSOs. We combine these two components in order to use a galaxy-centred approach to study metals in the CGM, by examining metal optical depths and EWs in the QSO spectra as a function of galaxy impact parameter and line-of-sight (LOS) distances. The metal ions examined here are, ordered by decreasing ionisation energy, OVI, NV, CIV, CIII, and SiIV. Additionally, we revisit the results for HI previously examined in Rakic et al. (2012) using the updated KBSS galaxy sample. Thanks to observations with MOSFIRE (McLean et al. 2012), not only has the total sub-sample size grown from 679 to 854 galaxies, but both the fraction and total number of galaxies with redshifts measured using nebular emission lines have increased substantially from 10% (71 galaxies) to 45% (381 galaxies).

The structure of the paper is as follows: we first describe our galaxy and QSO samples in § 2, while in § 3 we discuss the pixel optical depth recovery for the various ions. The results are presented in § 4, where in particular we examine optical depth maps in § 4.1; cuts through these maps in § 4.2; optical depths as a function of 3-dimensional (3-D) Hubble distance in § 4.3; the optical depth distributions in § 4.5; EWs in § 4.6; covering fractions in § 4.4; and the effects of the galaxy redshift measurement errors in § 4.7. Finally, we present our conclusions in § 5. Throughout the paper, we quote proper rather than comoving units (denoted as pkpc and pMpc), and have used cosmological parameters determined from the Planck mission (Planck Collaboration et al. 2013), i.e. $H_0 = 67.1$ km s⁻¹ Mpc⁻¹, $\Omega_m = 0.318$, and $\Omega_{\Lambda} = 0.683$.

2 GALAXY SAMPLE

The sample of galaxies used in this work comes from a subset of the KBSS, which consists of ~ 2550 (z) ~ 2.3 galaxies selected to lie in the fields of 15 hyper-luminous ($L_{\text{bol}} \gtrsim 10^{14} L_{\odot}$) redshift 2.5–2.85 QSOs which all have extremely high-quality, i.e., high resolution and signal-to-noise (S/N) Keck/HIRES spectra. The galaxies in each QSO field were chosen primarily using ultraviolet (UV) colour selection techniques (Steidel et al. 2003, 2004; Adelberger et al. 2004) with the purpose of tuning the galaxy redshift selection functions to optimise overlap with the range probed

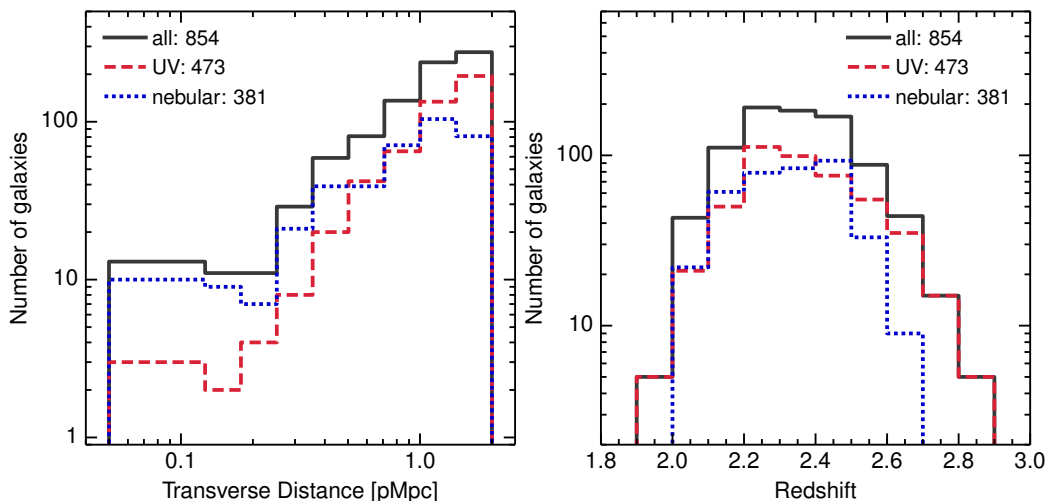


Figure 1. Histograms of the sub-sample of KBSS galaxies used in this work, selected to have redshifts in the Ly α forest and impact parameters ≤ 2 pMpc. The left panel shows the distribution as a function of impact parameter, and the right as a function of galaxy redshift. The values for the impact parameter histogram are given in Table 1.

Table 1. Number of galaxies per impact parameter bin. Except for the innermost bin (which has been extended in order to include the smallest impact parameter galaxies), the bins are spaced logarithmically and are 0.15 dex in size.

| Bin # | Lower edge (pMpc) | Upper edge (pMpc) | Total # of galaxies | # with nebular z |
|-------|-------------------|-------------------|---------------------|--------------------|
| 1 | 0.04 | 0.13 | 13 | 10 |
| 2 | 0.13 | 0.18 | 11 | 9 |
| 3 | 0.18 | 0.25 | 11 | 7 |
| 4 | 0.25 | 0.36 | 29 | 21 |
| 5 | 0.36 | 0.50 | 59 | 39 |
| 6 | 0.50 | 0.71 | 81 | 39 |
| 7 | 0.71 | 1.00 | 136 | 71 |
| 8 | 1.00 | 1.42 | 238 | 104 |
| 9 | 1.42 | 2.00 | 276 | 81 |

by the QSO spectra. Galaxies with apparent magnitude $m_R \leq 25.5$ were then followed up spectroscopically using Keck/LRIS, NIRSPEC, and/or MOSFIRE, with priority given to those likely to have redshifts in the QSO Ly α forest and those near the QSO sightline. For more details on the observations, see § 2.1 of Rudie et al. (2012).

Typically, the galaxies in the full survey sample have dynamical masses of $\sim 7 \times 10^{10} M_{\odot}$ (Erb et al. 2006c), and reside in halos with masses $\sim 10^{12} M_{\odot}$ (Adelberger et al. 2005b; Conroy et al. 2008; Trainor & Steidel 2012; Rakic et al. 2013). This corresponds to virial radii and circular velocities of ≈ 90 pkpc and ≈ 217 km s $^{-1}$, respectively. They tend to have median star formation rates $\sim 25 M_{\odot} \text{ yr}^{-1}$ (Erb et al. 2006b; Steidel et al. 2014), gas-phase metallicities $\sim 0.5 Z_{\odot}$ (Erb et al. 2006a) and stellar ages ~ 0.7 Gyr (Erb et al. 2006c).

The sub-sample that we use satisfies two constraints. Firstly, we require that the galaxies have impact param-

eters ≤ 2 pMpc (or $\simeq 4'$ at $z \sim 2.4$), so that the range in common is covered in all 15 KBSS fields. Secondly, we only use galaxies that have a redshift within the range of the Ly α forest, since our pixel optical depth recovery is limited to this region (see § 3). We define the redshift of the Ly α forest as follows:

$$(1 + z_{\text{qso}}) \frac{\lambda_{\text{Ly}\beta}}{\lambda_{\text{Ly}\alpha}} - 1 \leq z \leq z_{\text{qso}} - (1 + z_{\text{qso}}) \frac{3000 \text{ km s}^{-1}}{c} \quad (1)$$

where $\lambda_{\text{Ly}\alpha} = 1215.7 \text{ \AA}$ and $\lambda_{\text{Ly}\beta} = 1025.7 \text{ \AA}$ are the H I Ly α and Ly β rest wavelengths, respectively. The lower limit on the galaxy redshifts is set by the beginning of the Ly β forest in H I, and a cut is made 3000 km s^{-1} bluewards of the redshift z_{qso} to avoid proximity effects (i.e., these regions can be affected by ejecta and/or the ionising radiation field originating from the QSO). We note that in our analysis (§ 4), we search for absorption within $\pm 1350 \text{ km s}^{-1}$ of galaxies. Therefore, in practice, our sample contains galaxies that have redshifts extending 1350 km s^{-1} above or below the Ly α forest limits given above.

Figure 1 shows histograms of the galaxy impact parameters (left panel) and redshifts (right panel) for the 854 galaxies that satisfy the above constraints. We also show the distributions separately for the galaxies whose redshifts were measured from rest-frame UV features (using LRIS; 473 galaxies) and from rest-frame optical nebular emission lines (using NIRSPEC and MOSFIRE; 381 galaxies). Since the impact parameter binning shown in this figure is used throughout this paper, we have included the bin edge values as well as the number of galaxies in each bin in Table 1. The two smallest impact parameter bins exhibit the strongest optical depth enhancement for the metals studied in this work, so many of our results are based on the nearest 24 galaxies, of which 19 have nebular redshifts. As the volume sampled in these inner bins is comparably small, the number of galaxies at small impact parameters is somewhat re-

duced compared to the larger bins. The median redshifts of the three galaxy samples shown (all galaxies, UV-only, and nebular-only) are $\langle z \rangle = 2.34, 2.35, \text{ and } 2.33$, respectively.

2.1 QSO Spectra

The 15 quasars that are part of the KBSS were all observed with Keck/HIRES, and their spectra have a typical resolution of $R \approx 36000$. A detailed description of the data is given in Rudie et al. (2012); briefly, the spectra were reduced using T. Barlow’s MAKEE package where each spectral order was continuum normalised using low-order spline interpolation, and the final spectra were rebinned to pixels of 2.8 km s^{-1} . The final continua were fitted by hand, with an automated iterative correction procedure applied redwards of the quasar’s Ly α emission line (described in Appendix A). Based on tests done in Aguirre et al. (2002), we expect the errors induced due to continuum fits to be $\lesssim 1\%$. We also test the effects of the automated continuum fit that we apply redwards of Ly α in Appendix B.

Six of the spectra contain damped Ly α systems (DLAs) in the Ly α forest region, which have been fitted with Voigt profiles and had their damping wings divided out (as described in Rudie et al. 2012). The saturated portions of the six Ly α forest region DLAs were masked and not used for the recovery of optical depths for ions in this region (our masking procedure is described more fully in Appendix A). For more information about the QSOs, see Table 1 of Rakic et al. (2012) and also Trainor & Steidel (2012).

2.2 Galaxy Redshifts

Redshifts for KBSS galaxies are measured from features in their rest-frame far-UV and optical spectra. The strongest features in the rest-frame UV spectra of these galaxies are the H I Ly α emission line (when present) and a series of metallic interstellar absorption lines. All of these strong features have been empirically determined to lie at significant velocity offsets with respect to the systemic velocity of the galaxy (Shapley et al. 2003; Adelberger et al. 2003; Steidel et al. 2010; Rakic et al. 2012) which is generally interpreted as evidence for strong mass outflows from such systems. The rest-frame optical spectra of KBSS galaxies consist primarily of nebular emission lines which arise in H II regions within these galaxies and therefore trace the systemic velocity of the system to much higher fidelity. For this reason, we prefer redshifts measured from nebular emission lines, when they are available.

Many galaxies in the KBSS have been observed with the near-IR Keck instruments NIRSPEC and MOSFIRE which have spectral resolutions $R \approx 1200$ and ≈ 3600 , respectively. Such observations allowed measurement of galaxy redshifts using their nebular emission lines H α , H β , and [O III] $\lambda\lambda 4959, 5007$ for 381 galaxies in our KBSS subsample. Since the nebular emission lines are good tracers of the systemic galaxy velocity, for those galaxies with nebular redshifts we take $z_{\text{gal}} = z_{\text{neb}}$. The measurement uncertainties for the two instruments, which were estimated by comparing multiple observations of the same galaxy either on

two separate occasions or in two different bands, are determined to be $\approx \pm 60 \text{ km s}^{-1}$ and $\approx \pm 18 \text{ km s}^{-1}$, respectively. We emphasise that most of the galaxies in the three smallest impact parameter bins have nebular redshifts (see Table 1).

The remaining 473 galaxies in our KBSS subsample lack rest-frame optical spectra and therefore have redshifts measured from rest-frame UV lines observed with Keck/LRIS ($R \approx 800\text{--}1300$). To account for the offset of rest-frame UV features from the systemic galaxy velocity, we apply a correction to those galaxy redshifts estimated from interstellar absorption lines, z_{ISM} , and Ly α emission lines, $z_{\text{Ly}\alpha}$.

Rakic et al. (2011) used the fact that the mean foreground galaxy Ly α absorption profiles seen in QSO spectra should be symmetric around the true galaxy redshift to determine the corrections needed to infer the systemic galaxy redshifts. Another approach, which is the one that we use in this work, was first applied by Adelberger et al. (2005a) and Steidel et al. (2010). They used a sample of galaxies having redshifts measured from both rest-frame UV and nebular emission lines to estimate the typical offset between the two measurement techniques.

To calculate the velocity offset values, we use all galaxies with $2 < z_{\text{neb}} < 3$ that have both rest-frame UV and optical spectra, where the errors on the mean have been determined from bootstrap resampling the galaxies 1000 times with replacement, and taking the 1σ confidence intervals. The resulting offset values are implemented as follows:

- For galaxies with only Ly α emission lines detected (50 galaxies),

$$z_{\text{gal,Ly}\alpha} = z_{\text{Ly}\alpha} - 220_{-29}^{+30} \text{ km s}^{-1}. \quad (2)$$

- For galaxies with only interstellar absorption lines (244 galaxies),

$$z_{\text{gal,ISM}} = z_{\text{ISM}} + 110_{-16}^{+19} \text{ km s}^{-1}. \quad (3)$$

- For galaxies with both Ly α emission and interstellar absorption (179 galaxies), first the following corrections are made to the measured redshifts:

$$\begin{aligned} z_{\text{gal,Ly}\alpha} &= z_{\text{Ly}\alpha} - 370_{-16}^{+17} \text{ km s}^{-1}, \\ z_{\text{gal,ISM}} &= z_{\text{ISM}} + 200_{-16}^{+18} \text{ km s}^{-1}. \end{aligned} \quad (4)$$

The arithmetic mean of the corrected redshifts,

$$z_{\text{gal}} = \frac{z_{\text{gal,Ly}\alpha} + z_{\text{gal,ISM}}}{2}, \quad (5)$$

is then used as the final corrected value, unless it does not satisfy

$$z_{\text{ISM}} < z_{\text{gal}} < z_{\text{Ly}\alpha}, \quad (6)$$

in which case we use the arithmetic mean of the uncorrected values,

$$z_{\text{gal}} = \frac{z_{\text{Ly}\alpha} + z_{\text{ISM}}}{2}. \quad (7)$$

Based on the sample of 238 galaxies with both nebular and UV redshift estimates, we find that the rest-frame UV redshifts exhibit a $1\text{-}\sigma$ scatter of $\pm 150 \text{ km s}^{-1}$. This value corresponds to the error for individual systemic redshift estimates, rather than the error on the mean velocity offset.

Table 2. Rest wavelengths of both strong and weak components and their separation (if applicable), as well as the pixel optical depth recovery implementation, for the different metal ions studied in this work.

| Metal ion | $\lambda_{\text{rest}}(\text{\AA})$ | | Δv (km s^{-1}) | Subtr. higher-order H α | Doublet min. | Self-contam. |
|-----------|-------------------------------------|----------|--------------------------------------|--------------------------------|--------------|--------------|
| | strong | weak | | | | |
| OVI | 1031.927 | 1037.616 | 1650 | ✓ | ✓ | |
| NV | 1238.821 | 1242.804 | 962 | | ✓ | |
| CIV | 1548.195 | 1550.770 | 498 | | | ✓ |
| CIII | 977.020 | ... | ... | ✓ | | |
| SiIV | 1393.755 | 1402.770 | 1930 | | ✓ | |

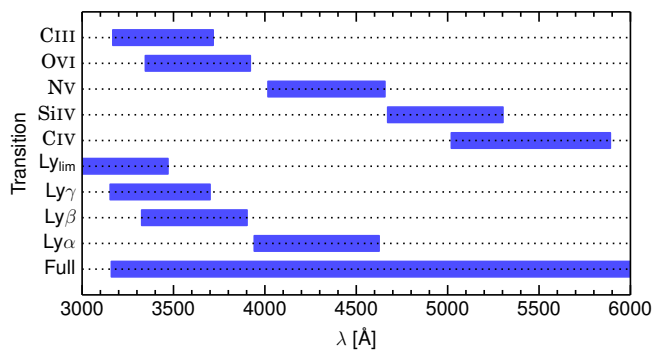


Figure 2. Wavelength ranges of various transitions in one of our QSOs (Q1549+1933, $z_{\text{qso}} = 2.8443$), when their redshifts are restricted to that of the H α Ly α forest ($z = 2.24$ – 2.81) plus the additional ion-dependent constraints outlined in § 3. The bottom row (marked “Full”) shows the wavelength range covered by the observed spectrum.

3 OPTICAL DEPTH RECOVERY

To study the absorption of metals in the vicinity of galaxies, we have used the pixel optical depth method (Cowie & Songaila 1998; Songaila 1998; Ellison et al. 2000; Schaye et al. 2000; Aguirre et al. 2002; Schaye et al. 2003) rather than the complementary technique of fitting Voigt profiles to absorption lines. The pixel optical depth approach is advantageous in the sense that it allows one to quickly and objectively measure absorption strengths in a statistical sense, even for weak signals in highly contaminated regions. On the other hand, with the standard pixel optical depth method, information about line widths is lost, and the interpretation of optical depths is not always as straightforward as that of column densities. In this section, we give a brief description of our specific implementation which is taken largely from Aguirre et al. (2002) with some minor improvements; more details can be found in Appendix A.

3.1 Redshift ranges

For each metal transition, the so-called fiducial redshift range that we use for the recovery is first set by that of the Ly α forest, which was described in § 2 and is given by

Equation 1. As for H α , for all ions considered we set the upper limit to be $z_{\text{qso}} - 3000 \text{ km s}^{-1}$ to avoid proximity effects. Additional redshift range modifications are made based on the transition in question, the reasons for which can be seen more clearly by examining Figure 2.

Firstly, the OVI region overlaps mainly with the Ly β forest, but extends marginally into the Ly α forest since its rest wavelength is slightly higher than that of Ly β . In an effort to make the contamination across the recovery area uniform, we limit OVI to overlap only with the Ly β forest, and take $z_{\text{max}} = (1 + z_{\text{qso}})\lambda_{\text{H}\alpha, \text{Ly}\beta} / \lambda_{\text{OVI}, 2} - 1$ where $\lambda_{Z, k}$ is the rest wavelength of multiplet component k of the ion Z .

The NV doublet ($\lambda_{\text{rest}} = [1238.8, 1242.8] \text{\AA}$) has rest-wavelengths which are slightly above that of H α Ly α ($\lambda_{\text{rest}} = 1215.8 \text{\AA}$), and therefore the recovery region of this species lies mainly in the Ly α forest. Although no correction is done for contamination by Ly α , to keep the level of contamination in the recovery region uniform, we impose the constraint that the recovered optical depth region must not extend to redshifts outside of the Ly α forest, namely $z_{\text{max}} = (1 + z_{\text{qso}})\lambda_{\text{Ly}\alpha} / \lambda_{\text{NV}} - 1$.

The recovery regions of CIV ($\lambda_{\text{rest}} = [1548.2, 1550.8] \text{\AA}$) and SiIV ($\lambda_{\text{rest}} = [1393.8, 1402.8] \text{\AA}$) both lie mainly redwards of the Ly α forest. In the case of SiIV, we avoid any contamination from Ly α by excluding wavelengths bluewards of the quasar’s Ly α emission, corresponding to a minimum redshift of $z_{\text{min}} = (1 + z_{\text{qso}})\lambda_{\text{Ly}\alpha} / \lambda_{\text{SiIV}} - 1$. For CIV, the limits given in Equation 1 are used; however, it is possible to expand the range to lower redshifts until the quasar’s Ly α emission limit is reached ($z_{\text{min}} = [1 + z_{\text{qso}}]\lambda_{\text{Ly}\alpha} / \lambda_{\text{CIV}} - 1$), which can significantly increase the number of galaxies in the sample. We experiment with this modification in Appendix B4.

3.2 Corrections for contamination

Below we briefly outline the optical depth recovery method used (see Appendix A for the full description). A summary of the metal ion rest wavelengths, the doublet separation in km s^{-1} (if applicable), and pixel optical depth implementations (to be explained below) is given in Table 2. Here we also note that the separation between the strong OVI transition ($\lambda_{\text{rest}} = 1031.927 \text{\AA}$) and H α Ly β ($\lambda_{\text{rest}} = 1025.7223 \text{\AA}$) is 1810 km s^{-1} . It is important to keep the above transi-

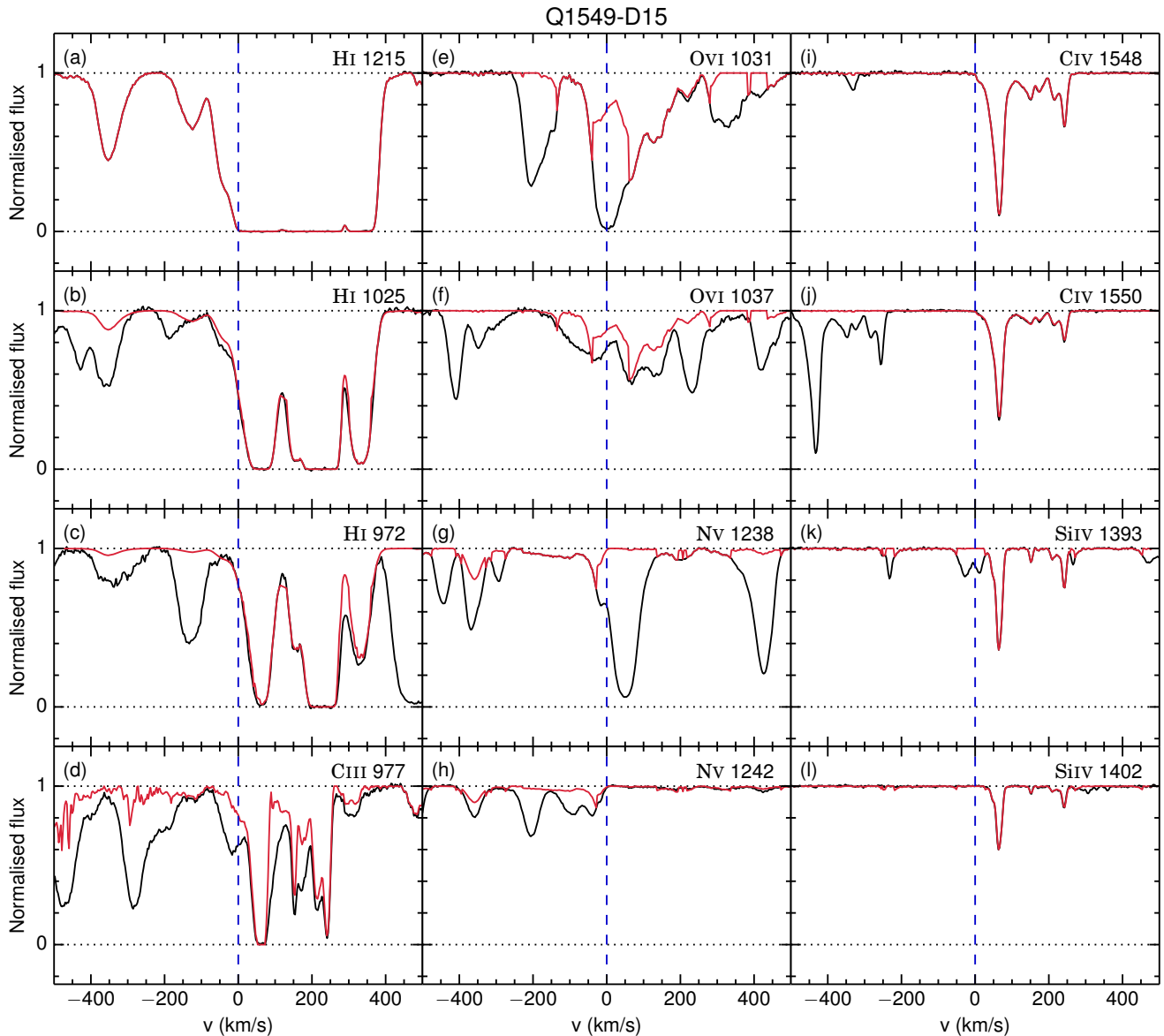


Figure 3. Normalised flux (black lines) and recovered optical depths converted to normalised flux (red lines) for regions $\pm 500 \text{ km s}^{-1}$ around the ions studied in this work at the redshift of the galaxy Q1549-D15, which has an impact parameter of 58 pkpc. $v = 0 \text{ km s}^{-1}$ corresponds to the galaxy redshift, and is marked by the vertical dashed blue line. We stress here that, particularly for those metal ions bluewards of $\text{Ly}\alpha$ (OVI, NV, and CIII), the derived optical depths are *apparent* rather than true optical depths, since we have no way of fully correcting for all possible contamination. Panels (a), (b) and (c) show $\text{Ly}\alpha$, $\text{Ly}\beta$ and $\text{Ly}\gamma$, respectively, and demonstrate how higher-order HI components often have unsaturated pixels which can be used to correct pixels which are saturated in $\text{Ly}\alpha$ (such as in the region shown here from 0–400 km s^{-1}). Panel (d) makes clear that much of the absorption in the CIII region can be attributed to higher order HI absorption, and is at least partially corrected for in the HI subtraction procedure. We note that the noise from the subtracted HI is responsible for the fine structure seen at negative velocities for CIII. Both NV (panels (g) and (h)) and SiIV (panels (k) and (l)) have their optical depths corrected for contamination by taking the minimum optical depth between the two double components. This procedure allowed us to identify and correct for the contaminating absorption systems located at ~ 50 and $\sim 450 \text{ km s}^{-1}$ for NV (panel (g)), and at ~ -250 and $\sim 0 \text{ km s}^{-1}$ for SiIV (panel (k)). The recovery procedure for the OVI doublet, shown in panels (e) and (f), uses both HI subtraction as well as taking the minimum optical depth value between the two doublet components. Finally, the $\sim -350 \text{ km s}^{-1}$ absorption line in panel (i) was identified and removed by the CIV self-contamination correction.

tion separations in mind when examining the optical depths, since contamination can be expected on these characteristic scales. To visualise the corrections for contamination, in Figure 3 we have plotted $\pm 500 \text{ km s}^{-1}$ regions of the spectrum around the galaxy Q1549-D15, for each of the ions studied. The black lines denote the original flux, while the red lines are calculated from the recovered optical depths derived using the following procedure.

Implementing the above redshift ranges, we define the optical depth for each ion Z and multiplet component k as $\tau_{Z,k}(z) = -\ln(F)$, where $F(\lambda)$ is the normalised flux at $\lambda = \lambda_k(1+z)$. Beginning with H I Ly α , the main source of error is the saturation of the absorption; to account for this, for every saturated pixel we search for unsaturated higher-order lines at the same redshift and take the minimum of the optical depths (corrected for differences in oscillator strengths and rest-frame wavelengths, and accounting for noise). An example of a saturated region with corresponding unsaturated higher-order lines can be seen in panels (a)–(c) of Figure 3. We also use the higher-order transitions to search for and flag Ly α pixels contaminated by metal line absorption, something which was not implemented in Aguirre et al. (2002).

The recovered H I optical depths are then used to clean the C III and O VI regions by subtracting the optical depths of five higher order H I lines starting from Ly β . In both Aguirre et al. (2002) and this work, the H I subtraction is performed on all unsaturated metal ion pixels. However, the subtraction cannot be done reliably for saturated metal ion pixels since their optical depths are not well defined. In Aguirre et al. (2002), such pixels remain unchanged by the subtraction procedure, which could result in recovered optical depths being biased high. To combat this, we have made another addition to the recovery method, where for saturated metal line pixels we sum the optical depths from the higher-order H I components. If this value is consistent with saturation, we flag the pixel as contaminated and discard it. Panel (d) of Figure 3 shows the effect of H I subtraction on the C III region, where any absorption that is seen in the black spectrum but not in the red is due to known higher-order H I lines.

Furthermore, since O VI is a doublet, we perform the H I subtraction on both doublet components and further correct for contamination by taking the minimum of the optical depths between the two components at each redshift, taking into account relative oscillator strengths and rest wavelengths. This doublet minimum correction is also made for N V and Si IV, which are mainly contaminated by H I Ly α and C IV, respectively. We note that for metals that have a doublet component, we always scale the weaker transition optical depths to the strongest transition (in this work, all doublets considered have an optical depth ratio of 2). Unlike in Aguirre et al. (2002), we allow pixels from the weaker transition to be used in the doublet minimum correction even if they have been flagged as having flux > 1 (or a negative optical depth). Panels (g)–(h) (N V) and (k)–(l) (Si IV) of Figure 3 demonstrate how this technique can remove contaminating absorption lines.

Finally, C IV shows relatively strong absorption with a

recovery region that lies redwards of the Ly α forest; this means that the main source of contamination comes from its own doublet. To correct for this, we iteratively subtract the expected optical depth of the contaminating doublet from each pixel. The result of doing so is shown in panels (i)–(j) of Figure 3.

How important is it to correct for contamination? In Appendix B we examine the recovery of each metal ion in turn to see how the above procedure affects our final result. In general, we find that performing the correction increases the dynamic range of recovered optical depths and decreases the scatter when they are binned as a function of galactocentric distance. However, we note that even without any corrections, the main conclusions of this work still hold.

It is important to note that the corrections for contamination are not perfect. For example, because we can only reliably recover H I Ly α in the range of the Ly α forest, we cannot correct contamination of O VI and C III (which lie in the Ly β forest) by Ly α . Hence, the optical depths quoted should not be taken at face value. This is particularly relevant for C III, N V and O VI, which all suffer from substantial residual contamination from H I. However, because the contamination is due to gas at very different redshifts, it does not vary systematically with the distance to galaxies will therefore not give rise to spurious trends of absorption strength with separation from galaxies. It can only compromise our ability to detect such a trend.

4 RESULTS

We can now use the recovered optical depths from § 3 and combine them with the redshifts and impact parameters of the galaxies from § 2 to investigate how H I and metal ions are distributed around galaxies. In § 4.1, we bin the pixel optical depths by galaxy impact parameter and along the LOS to create 2-dimensional (2-D) optical depth maps, while in § 4.2 we make the cuts through these maps to look for redshift space distortions in order to compare the optical depth distributions for different ions. We bin the pixels by their 3-D distance to the galaxy in § 4.3, where distances are estimated assuming pure Hubble flow, and in § 4.5 we show how the distribution of optical depths for each ion varies as a function of impact parameter. Covering fractions are examined in § 4.4, and lastly we explore the effect of galaxy redshift errors on our results in § 4.7. Unless specified otherwise, all errors are calculated by bootstrap resampling (with replacement) the galaxy sample 1000 times within each impact parameter bin, and taking the 1σ confidence intervals.

4.1 2-D Optical depth maps

For each ion we have constructed a galaxy-centred map of the median optical depth as a function of the transverse and LOS separation from the galaxies. The maps extend 2 pMpc in the transverse direction and 5.64 pMpc along the LOS (i.e. $\pm 1350 \text{ km s}^{-1}$), where velocity differences were converted into proper distances given each galaxy’s redshift

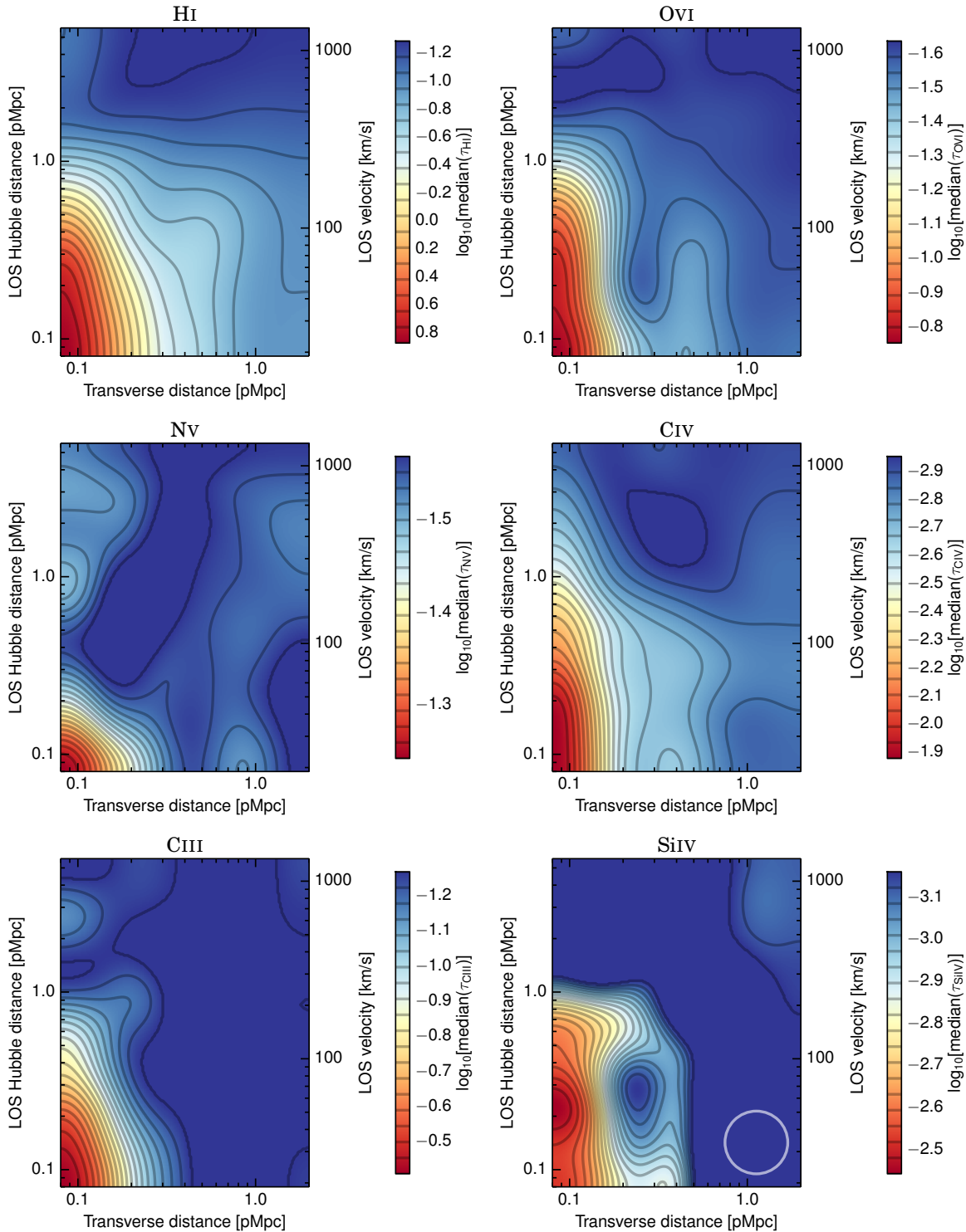


Figure 4. 2-D optical depth maps constructed by binning the galaxy impact parameters and LOS distance (assuming pure Hubble flow) logarithmically, taking the absolute LOS distance, and calculating the median optical depth in each bin. The bins are 0.15 dex wide except for the innermost bin, which runs from 0 to 130 pkpc. The maps have been smoothed using a Gaussian that has σ equal to the bin size, and the FWHM of the smoothing kernel is indicated by open white circle in the bottom right corner of the SiIV map. For each ion, the range of optical depths is set to run from the median of all pixels in the considered redshift range to the maximum value in the smoothed image. Note that the minimum optical depth shown typically reflects the median level of noise and contamination rather than the detection of true metal absorption. The ions considered and their rest frame wavelengths are, from left to right: HI (1215.7 Å), OVI (1031.9 Å), NV (1238.8 Å), CIV (1548.2 Å), CIII (977.0 Å), and SiIV (1393.8 Å). In every case, there is a region of very strongly enhanced absorption at impact parameters of $\lesssim 2$ pkpc, which is smeared along the LOS direction. This elongation likely originates primarily from gas peculiar velocities, as discussed in § 4.7.

Table 3. The median $\log_{10} \tau_{\text{HI}}$ and 1σ errors as a function of impact parameter (rows) and distance along the LOS (columns), used to construct Figure 4. The values for the innermost transverse and LOS distance bins are plotted in Figure 5. Tables for OVI, NV, CIV, CIII, and SiIV are available online at http://www.strw.leidenuniv.nl/~turnerm/kbss_metals_table.pdf.

| HI | | | | | | | | | |
|------------|-------------------------|-------------------------|-------------------------|-------------------------|-------------------------|-------------------------|-------------------------|-------------------------|-------------------------|
| D (pMpc) | 0.04–0.13 | 0.13–0.18 | 0.18–0.25 | 0.25–0.36 | 0.36–0.50 | 0.50–0.71 | 0.71–1.00 | 1.00–1.42 | 1.42–2.00 |
| 0.00–0.13 | $1.06^{+0.94}_{-0.29}$ | $0.13^{+0.25}_{-0.37}$ | $0.08^{+0.39}_{-1.37}$ | $-0.83^{+0.29}_{-0.14}$ | $-0.28^{+0.15}_{-0.17}$ | $-0.78^{+0.18}_{-0.17}$ | $-0.98^{+0.09}_{-0.09}$ | $-0.97^{+0.08}_{-0.08}$ | $-0.92^{+0.09}_{-0.08}$ |
| 0.13–0.18 | $0.95^{+0.32}_{-0.31}$ | $-0.12^{+0.18}_{-0.24}$ | $0.11^{+0.24}_{-0.99}$ | $-0.94^{+0.27}_{-0.21}$ | $-0.40^{+0.17}_{-0.17}$ | $-0.81^{+0.15}_{-0.11}$ | $-0.95^{+0.12}_{-0.11}$ | $-0.98^{+0.08}_{-0.09}$ | $-0.92^{+0.10}_{-0.09}$ |
| 0.18–0.25 | $0.99^{+0.17}_{-0.21}$ | $-0.40^{+0.63}_{-0.11}$ | $-0.01^{+0.23}_{-0.65}$ | $-0.90^{+0.42}_{-0.27}$ | $-0.49^{+0.15}_{-0.14}$ | $-0.72^{+0.13}_{-0.15}$ | $-1.00^{+0.12}_{-0.07}$ | $-0.93^{+0.08}_{-0.07}$ | $-0.97^{+0.09}_{-0.08}$ |
| 0.25–0.36 | $0.96^{+0.20}_{-0.70}$ | $-0.31^{+0.28}_{-0.51}$ | $-0.55^{+0.25}_{-0.16}$ | $-0.71^{+0.21}_{-0.28}$ | $-0.50^{+0.12}_{-0.16}$ | $-0.55^{+0.09}_{-0.13}$ | $-0.96^{+0.08}_{-0.07}$ | $-0.95^{+0.09}_{-0.07}$ | $-0.96^{+0.06}_{-0.07}$ |
| 0.36–0.50 | $0.43^{+0.43}_{-0.72}$ | $-0.68^{+0.76}_{-0.25}$ | $-0.65^{+0.17}_{-0.10}$ | $-0.91^{+0.24}_{-0.20}$ | $-0.52^{+0.16}_{-0.18}$ | $-0.63^{+0.11}_{-0.09}$ | $-0.86^{+0.11}_{-0.09}$ | $-0.98^{+0.06}_{-0.06}$ | $-0.96^{+0.07}_{-0.06}$ |
| 0.50–0.71 | $0.05^{+0.37}_{-0.47}$ | $-0.53^{+0.79}_{-0.41}$ | $-0.88^{+0.32}_{-0.22}$ | $-0.87^{+0.24}_{-0.28}$ | $-0.75^{+0.24}_{-0.19}$ | $-0.70^{+0.07}_{-0.10}$ | $-0.85^{+0.11}_{-0.08}$ | $-0.93^{+0.06}_{-0.06}$ | $-0.99^{+0.06}_{-0.07}$ |
| 0.71–1.00 | $-0.51^{+0.09}_{-0.12}$ | $-0.57^{+0.32}_{-0.23}$ | $-0.68^{+0.27}_{-0.29}$ | $-0.98^{+0.17}_{-0.18}$ | $-0.79^{+0.12}_{-0.13}$ | $-0.96^{+0.10}_{-0.08}$ | $-0.92^{+0.06}_{-0.08}$ | $-1.00^{+0.05}_{-0.06}$ | $-1.02^{+0.05}_{-0.05}$ |
| 1.00–1.42 | $-0.81^{+0.18}_{-0.22}$ | $-0.89^{+0.13}_{-0.11}$ | $-0.94^{+0.47}_{-0.19}$ | $-1.09^{+0.14}_{-0.12}$ | $-1.04^{+0.10}_{-0.11}$ | $-1.13^{+0.09}_{-0.09}$ | $-1.06^{+0.07}_{-0.06}$ | $-1.09^{+0.05}_{-0.05}$ | $-1.10^{+0.05}_{-0.05}$ |
| 1.42–2.00 | $-1.36^{+0.19}_{-0.14}$ | $-1.45^{+0.23}_{-0.18}$ | $-1.04^{+0.33}_{-0.27}$ | $-1.14^{+0.09}_{-0.11}$ | $-1.26^{+0.07}_{-0.07}$ | $-1.17^{+0.08}_{-0.08}$ | $-1.09^{+0.07}_{-0.06}$ | $-1.16^{+0.04}_{-0.04}$ | $-1.16^{+0.04}_{-0.04}$ |
| 2.00–2.83 | $-0.98^{+0.27}_{-0.22}$ | $-1.43^{+0.11}_{-0.15}$ | $-1.32^{+0.09}_{-0.10}$ | $-1.39^{+0.13}_{-0.13}$ | $-1.36^{+0.07}_{-0.08}$ | $-1.16^{+0.06}_{-0.06}$ | $-1.29^{+0.04}_{-0.04}$ | $-1.17^{+0.03}_{-0.04}$ | $-1.25^{+0.03}_{-0.04}$ |
| 2.83–3.99 | $-1.01^{+0.11}_{-0.14}$ | $-1.34^{+0.10}_{-0.09}$ | $-1.43^{+0.21}_{-0.14}$ | $-1.24^{+0.09}_{-0.09}$ | $-1.27^{+0.06}_{-0.07}$ | $-1.28^{+0.05}_{-0.05}$ | $-1.33^{+0.05}_{-0.05}$ | $-1.22^{+0.03}_{-0.03}$ | $-1.28^{+0.03}_{-0.03}$ |
| 3.99–5.64 | $-1.02^{+0.12}_{-0.14}$ | $-1.20^{+0.11}_{-0.12}$ | $-1.38^{+0.17}_{-0.12}$ | $-1.21^{+0.10}_{-0.10}$ | $-1.34^{+0.06}_{-0.06}$ | $-1.38^{+0.05}_{-0.06}$ | $-1.27^{+0.04}_{-0.04}$ | $-1.29^{+0.03}_{-0.02}$ | $-1.28^{+0.03}_{-0.03}$ |

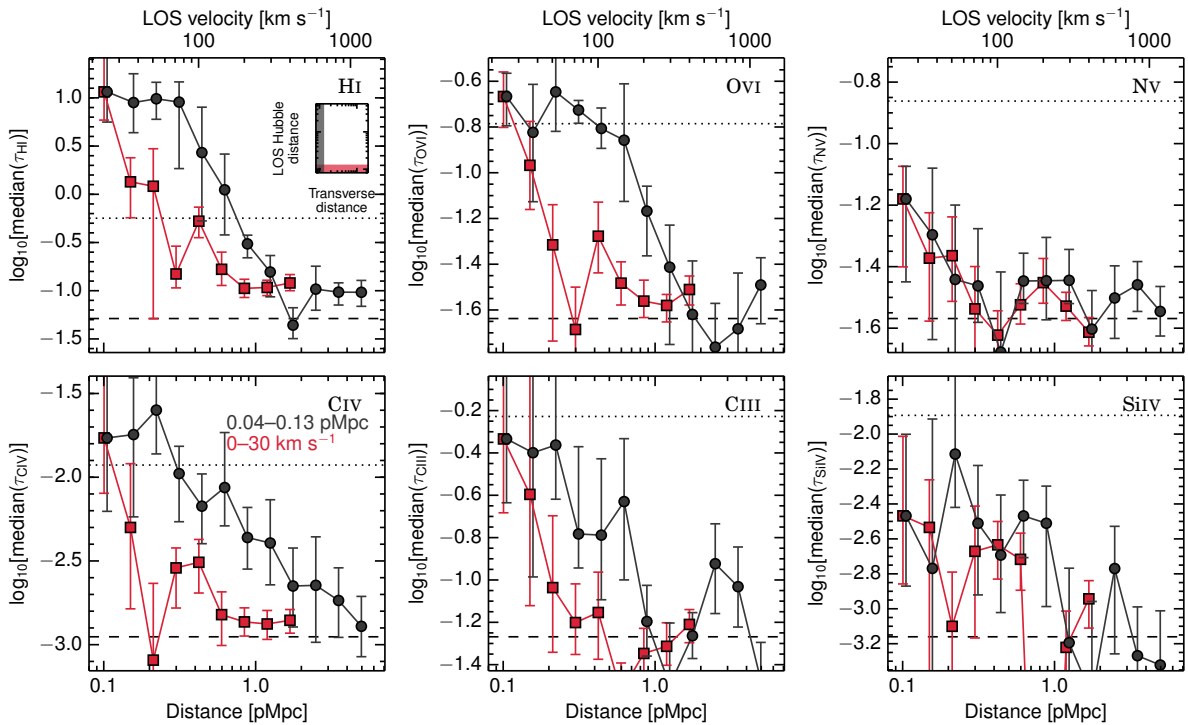


Figure 5. Cuts through the median optical depth maps shown in Figure 4 along the innermost LOS and transverse distance bins, where each panel represents a different ion. Contrary to Figure 4, the data have not been smoothed. The black circles run along the LOS and are taken from a 0.04–0.13 pMpc cut in impact parameter, while the red squares run along the transverse direction using a $\pm 30.0 \text{ km s}^{-1}$ LOS cut size, which corresponds to 0.13 pMpc at $z = 2.34$ in the case of pure Hubble flow. The insets show the scaled down areas plotted in Figure 4, where the coloured strips denote the cut sizes. The horizontal dashed lines represent the median optical depths of all pixels in the redshift range considered for each ion, while the horizontal dotted line shows the 1σ scatter. In every case except for NV, the median optical depth values along the LOS are greater than those in the transverse direction for bins 2–7 (i.e. out to $\sim 1 \text{ pMpc}$ or 240 km s^{-1}).

Table 4. The log of the median optical depth, and the median continuum S/N of all pixels (with normalized flux > 0.7) in the redshift range considered for the particular ion and recovery method.

| Ion | $\log_{10}\tau_{Z,\text{rnd}}$ | S/N _{med} |
|------|--------------------------------|--------------------|
| HI | -1.29 | 70.1 |
| OVI | -1.64 | 45.7 |
| NV | -1.57 | 72.4 |
| CIV | -2.95 | 83.6 |
| CIII | -1.27 | 37.8 |
| SiIV | -3.16 | 84.4 |

and assuming pure Hubble flow. The pixels contributing to the maps were binned logarithmically in the LOS and transverse directions, where the first bin runs from 0.04–0.13 pMpc and subsequent bins are 0.15 dex wide. We note that each bin contains pixels coming from several different galaxy sightlines, where the number of contributing galaxies depends on the impact parameter (see Table 1). The median pixel optical depth in each bin was then taken to construct Figure 4, where the images were smoothed by a Gaussian with a σ equal to the bin size. The right y -axis indicates the LOS velocity difference assuming the median redshift of the galaxies in our sample, $z = 2.34$. The (unsmoothed) optical depth values in each bin, plus their 1σ errors, are given in Table 3.

We note that the optical depth scales on the maps presented in Figure 4 run from the median optical depth of all pixels in the redshift range considered for the particular ion and recovery method (which we denote as $\tau_{Z,\text{rnd}}$ for each ion Z), up to the maximum value of all smoothed pixels in the image, in order to maximise the dynamic range. It is therefore advised that care be taken in the interpretation of these maps, as the true dynamic range of any one species may not be properly captured since the minimum of the range (set by $\tau_{Z,\text{rnd}}$) is set by the contamination and/or shot noise. We list $\tau_{Z,\text{rnd}}$ (as well as the median S/N for all considered pixels) for each ion in Table 4.

One should also keep in mind that although these maps are constructed by situating the galaxies at the origin, at large distances the median absorption is likely affected by gas near neighbouring galaxies, most of which will be undetected. These maps should be interpreted as the average properties of gas around galaxies, which include the effects of clustering. We elaborate further on this point in § 4.4.

Before further discussing Figure 4, we first summarise the results from a similar analysis of HI from Rakic et al. (2012), using an earlier sample from the KBSS (see also Rudie et al. 2012). We note that the 2-D HI median optical depth map presented in Figure 6 of Rakic et al. (2012) is analogous to the top left panel of Figure 4 in this work (but created with a slightly different galaxy sample). As described in Rakic et al. (2012), the first point to note from these figures is the strongly enhanced absorption extending $\sim 10^2$ pkpc in the transverse direction and ~ 1 pMpc (~ 240 km s $^{-1}$) along the LOS. They concluded that this redshift space distortion, often called the “finger of God”

effect, could have two origins. Firstly, the redshift estimates of the galaxies have associated errors that smear the signal along the LOS. Specifically, the errors are roughly $\Delta v \approx 150$ km s $^{-1}$ for LRIS, $\Delta v \approx 60$ km s $^{-1}$ for NIRSPEC, and $\Delta v \approx 18$ km s $^{-1}$ for MOSFIRE redshifts. Additionally, peculiar velocities of the gas arising from infall, outflows or virial motions may be responsible for this effect, particularly because the extent of the elongation is greater than that which one may expect purely from redshift errors.

The second main result from the 2-D HI median optical depth map studied in Rakic et al. (2012) (again, see their Figure 6 or the top left panel of our Figure 4) was the presence of an anisotropy on large scales. They noticed that while HI absorption was enhanced out to the maximum considered impact parameter of 2 pMpc, along the LOS it already dropped off at ≈ 1.5 pMpc (≈ 300 km s $^{-1}$). Such a feature could be attributed to the Kaiser (1987) effect, originally defined as Doppler shifts in galaxy redshifts caused by the large-scale coherent motions of the galaxies towards cluster centres, which manifest as LOS distortions. Although in this work we are not specifically looking at clusters, any large-scale coherent motions should produce a similar effect. In the case of Rakic et al. (2012), since one would expect redshift space distortions caused by measurement errors to elongate the signal, the observed compression is likely due to peculiar velocities of infalling gas. Indeed, Rakic et al. (2013) used simulations to show that the observed anisotropy is consistent with being due to the Kaiser effect. However, we note that a similar study at $z \sim 3$ by Tummuangpak et al. (2013) examining the Ly α -galaxy correlation function found the observed infall to be smaller than would be predicted by simulations.

We emphasise here that the typical galaxy redshift error of our sample has changed substantially since Rakic et al. (2012). Most galaxies in the innermost bins now have redshifts measured using nebular lines, while the converse was true for Rakic et al. (2012, see their Figure 1). However, as we show in Appendix D, the extent of the elongation of the optical depth signal along the LOS direction has not changed significantly between the two samples, even though the redshift errors are now considerably smaller. This suggests that the main origin of the small-scale anisotropy is gas peculiar velocities (see § 4.7 for further discussion). Note also that the large-scale anisotropy detected by Rakic et al. (2012) is also present here, as can be seen most clearly from the top left panel of Figure 5 (compare the last red point with the black point at the same distance).

While the goal of Rakic et al. (2012) was to study HI, in this work we are extending the analysis to metal ions. In Figure 4 we compare the 2-D HI optical depth distribution to those of the metals. In all cases we see a strong central enhancement of absorption, which is elongated along the LOS. For a more quantitative picture, we have made “cuts” through the maps, and plotted the (unsmoothed) optical depth values from the nearest LOS bin (red squares) and the innermost transverse distance bin (black circles) for each ion in Figure 5 (see also Table 3). Note that the first bin is identical for the transverse and LOS directions. For every ion except for NV (and one data point in SiIV), the optical

depths of the data points in the LOS direction are greater than those in the transverse direction (i.e., the black points are above the red points) for bins 2–7, or out to ~ 1 pMpc.

The discrepancy between NV and the other ions is likely due to the fact that NV is both relatively weak and has HI contamination that is difficult to correct for, and not necessarily due to intrinsically different redshift-space structure. This is supported by the fact that the dynamic range of optical depths probed for NV is much smaller than those for the other ions.

In Figure 5 we show the median optical depth of a random region (horizontal dashed line) as well as the 1σ scatter (horizontal dotted line). From this, it is clear that the scatter is quite large relative to many of the detected optical depth enhancements. The full distribution of pixel optical depths is discussed in more detail in § 4.5.

We estimate the confidence levels associated with these measurements by bootstrap resampling the galaxies in each impact parameter bin. In each bootstrap realisation we randomise the galaxy redshifts and compute the median optical depth as a function of transverse or LOS distance for both the original and randomised galaxy redshifts. Then, in each transverse or LOS distance bin, we calculate the fraction of bootstrap realisations for which the median optical depth computed using galaxies with randomised redshifts is higher than the median optical depth computed using the original galaxy redshifts. From this, we determine that for NV, only in the innermost bin is the optical depth enhancement detected with a confidence level $\geq 68\%$ (1σ).

In Figure 6 (Table 5) we now make larger cuts through the maps from Figure 4, and divide the results for each ion by $\tau_{Z,\text{rnd}}$ in order to compare the ions with each other in the same figure. Since the innermost impact parameter bin contains only 13 galaxies, and because we see an enhanced optical depth signal out to larger distances, for the cut along the LOS direction we combine the two innermost impact parameter bins to create a single bin out to 0.18 pMpc. In the transverse direction, we combine the six smallest bins, which leads to a cut size of ± 170 km s $^{-1}$ (or 0.71 pMpc). A similar bin size was previously motivated by Rakic et al. (2011)¹ because it is the scale over which τ_{HI} is smooth in the LOS direction, and because they found errors between points along LOS direction (but not in the transverse direction) to be correlated on smaller scales (i.e. for separations $\lesssim 100$ km s $^{-1}$; see Appendix B of Rakic et al. 2012). We note that the conclusions from this section are not affected by the precise size of the cut.

From the right panels of Figure 6 we can see that in general, along the LOS, the optical depth enhancement is very small or undetectable beyond ~ 240 km s $^{-1}$ (~ 1 pMpc) for both HI and the metals. In the transverse direction only HI and CIV remain significantly enhanced above the noise level for all impact parameters. Calculating confidence intervals as before, we find a $\geq 84\%$ confidence level for HI in every

bin, and a $\geq 68\%$ (i.e., 1σ) confidence level for CIV at every point except for the sixth bin (0.50–0.71 pMpc) which has a confidence level of 55%.

It is important to mention that the non-detection of this large-scale enhancement for the other the metal ions may be due to sensitivity limits rather than a true paucity of these species at larger impact parameters. Due either to contamination (for ions with rest wavelengths shortward of Ly α) or shot noise and continuum fitting errors (for SiIV), we are likely unable to probe optical depths down to the true median level for these ions.

4.2 Rescaled profiles

Next we consider the distribution of the metals presented in our optical depth maps and compare them to HI and to each other, in an effort to explore whether the measured absorption signals trace the same gaseous structure. Of course, the metal optical depths are set not only by the metal abundance, but are also determined by the varying degree of ionisation and hence by the density and temperature of the gas in which they reside.

With this point in mind, we explore whether the optical depth profiles of the different ions arise from the same intrinsic functional form, i.e. whether their spatial (in the transverse direction) or kinematic (in the LOS direction) profiles have the same shape. However, as Figures 4, 5, and 6 suggest, the comparison is not straightforward, as some metals have a very small dynamic range where the median optical depth (set by the detection limit) lies close to the maximum binned optical depth value. We therefore propose a method to normalise the curves to alleviate this problem.

If all ions follow the same intrinsic profile, but appear to vary because the transitions through which they are observed have different strengths and because they suffer from different levels of contamination and noise, then for each ion Z , the median optical depth profile can be written as

$$f_Z(x) = a_Z f(x) + \text{med}_Z \quad (8)$$

where $f_Z(x)$ is the observed, apparent optical depth of species Z , $f(x)$ is the intrinsic profile (which varies from $\max(f)$ at $x = 0$ to 0 as $x \rightarrow \infty$), a_Z is a scale factor that sets the relative strengths of different transitions, and med_Z is the median optical depth to which the curve asymptotes (i.e. the detection limit set by noise and contamination). For CIV and SiIV, this value is set mostly by shot noise and continuum fitting errors, while for the other transitions it is mainly unrelated absorption (i.e. contamination).

Although the values of a_Z and med_Z will certainly depend on the ion in question, it is possible that the intrinsic profile $f(x)$ does not vary between different ions. To examine this, we can try and normalise the curves such that, if indeed $f(x)$ does not depend on the ion Z , then the normalised curves should also be equivalent for different ions. This can be achieved using the following transformation:

$$g_Z(x) = \frac{f_Z(x) - \text{med}_Z}{\max_Z - \text{med}_Z} + 1 \quad (9)$$

where $\max_Z = f_Z(x_{\text{max}})$ and x_{max} is the value of x at which

¹ Due to a slightly different cosmology and median galaxy redshift used in Rakic et al. (2012), the velocity interval corresponding to 0.71 pMpc was closer to ± 165 km s $^{-1}$.

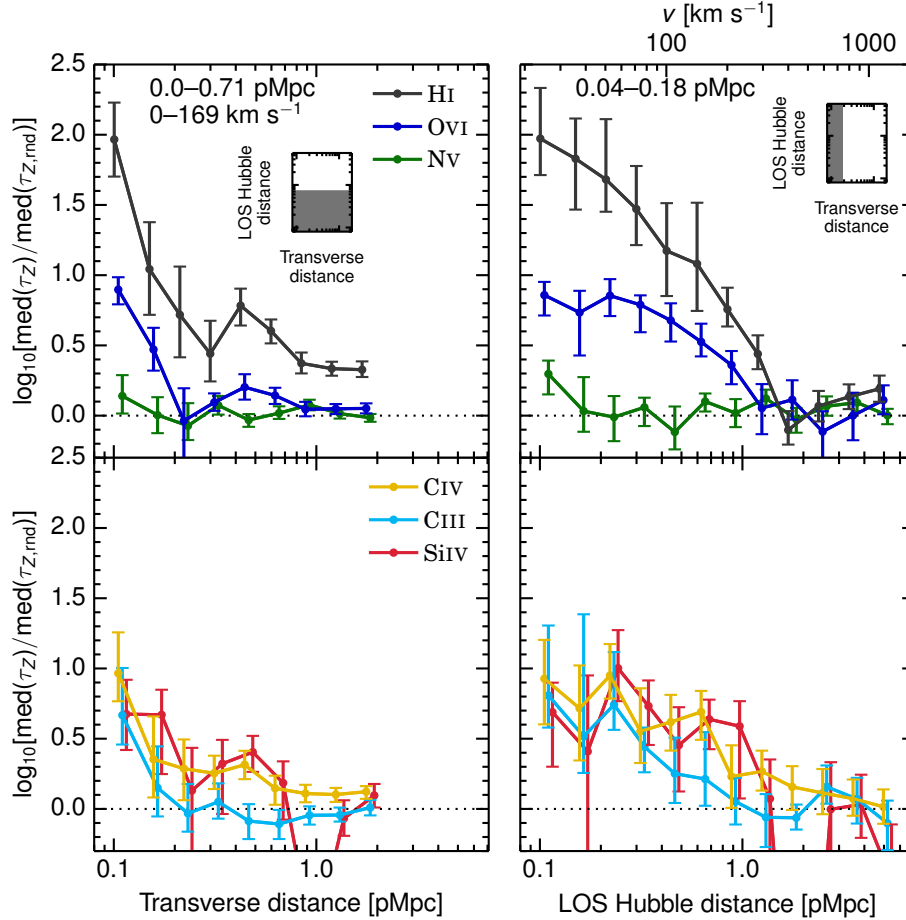


Figure 6. Cuts through the (unsmoothed) median optical depth maps from Figure 4 along the transverse (left) and LOS (right) directions. All optical depths were divided by their corresponding $\tau_{Z,\text{rnd}}$ so that the medians of all ions are aligned, and denoted by the horizontal dotted black line. For clarity, the different ions have been divided between the top and bottom panels, and the points have been offset from each other horizontally by 0.02 dex. The shaded strip in the inset shows the region included in each cut. Except for NV, the optical depths of all ions are enhanced out to at least 180 pkpc in the transverse direction and ~ 1 pMpc ($\sim 240 \text{ km s}^{-1}$) along the LOS. Like HI, the optical depth of CIV is significantly enhanced along the entire extent of the transverse direction (bottom left panel).

the maximum value of $f_Z(x)$ occurs. For the optical depth profiles, x_{max} is usually the innermost transverse or LOS distance bin. Combining Equations 8 and 9, we obtain the expression $g_Z(x) = f(x)/f(x_{\text{max}}) + 1$, which is independent of Z and varies between 1 and 2. In summary, if the observed spatial and/or kinematic optical depth profiles of different ions are all the same apart from a multiplicative factor reflecting the strength of the transition and an additional constant reflecting the levels of contamination and noise, then by using the transformation in Equation 9, the resulting curves should all overlap each other.

We implemented the above by taking med_k to be $\tau_{Z,\text{rnd}}$, and max_k to be the optical depth of the innermost point of the curve in question (the values differ along the LOS and transverse directions, due to the different cut sizes taken). The resulting curves are shown in Figure 7. Note that the normalisation method will amplify any small point-to-point

variations inversely with dynamic range. Since NV has a relatively small dynamic range, variations which appear small in the top left panel (particularly the first few points along the transverse direction) of Figure 6 manifest themselves as large deviations compared to the other curves, and for this reason we have chosen to omit NV from Figure 7.

The curves resulting from cuts along the transverse direction (left panels of Figure 7) appear quite similar for all species observed. In every case (including HI), the optical depth drops sharply after the first impact parameter bin, and quickly asymptotes to the median. The plateau in the absorption at impact parameters 180 pkpc–2 pMpc that was clearly detected for HI and CIV in Figures 4 and 6 may therefore also be present for the other species, but cannot be detected due to the smaller dynamic range in their recovered optical depths. Along the LOS (right panels of Figure 7), the situation is less uniform. While CIII tends to

Table 5. The median $\log_{10}\tau_Z$ and 1σ errors determined by taking cuts through Figure 4. Unlike in Figure 5, bins have now been combined in order to reduce the amount of noise and facilitate comparisons between different ions, and the results are plotted in Figure 6. Specifically, the values along the transverse direction (top portion of the table) are measured from a 170 km s^{-1} (0.71 pMpc , or combining the first six bins) cut along the LOS, while the values along the LOS (bottom portion of the table) are calculated from a 0.18 pMpc (combining the first two bins) transverse direction cut. For comparison, the bottom row of the table lists the median optical depths measured over the full redshift range of each ion ($\tau_{Z,\text{rnd}}$). We note that $\log_{10}\tau_{\text{SiIV}} = -6.00$ is a flag value which indicate that the median optical depth in that bin is negative.

| D_{trans} (pMpc) | HI | OVI | NV | CIV | CIII | SiIV | |
|---|-------------------------|-------------------------|-------------------------|-------------------------|-------------------------|-------------------------|-------------------------|
| 0.04–0.13 | $0.68^{+0.26}_{-0.26}$ | $-0.74^{+0.09}_{-0.10}$ | $-1.43^{+0.15}_{-0.12}$ | $-1.99^{+0.29}_{-0.20}$ | $-0.60^{+0.34}_{-0.21}$ | $-2.49^{+0.24}_{-0.26}$ | |
| 0.13–0.18 | $-0.25^{+0.33}_{-0.33}$ | $-1.17^{+0.15}_{-0.15}$ | $-1.56^{+0.13}_{-0.13}$ | $-2.60^{+0.31}_{-0.21}$ | $-1.12^{+0.30}_{-0.20}$ | $-2.49^{+0.18}_{-0.42}$ | |
| 0.18–0.25 | $-0.57^{+0.34}_{-0.30}$ | $-1.67^{+0.33}_{-0.34}$ | $-1.64^{+0.16}_{-0.10}$ | $-2.67^{+0.21}_{-0.22}$ | $-1.30^{+0.21}_{-0.13}$ | $-3.03^{+0.30}_{-0.51}$ | |
| 0.25–0.36 | $-0.85^{+0.23}_{-0.20}$ | $-1.54^{+0.06}_{-0.06}$ | $-1.50^{+0.07}_{-0.07}$ | $-2.70^{+0.13}_{-0.11}$ | $-1.22^{+0.13}_{-0.12}$ | $-2.84^{+0.17}_{-0.36}$ | |
| 0.36–0.50 | $-0.51^{+0.12}_{-0.14}$ | $-1.44^{+0.09}_{-0.09}$ | $-1.60^{+0.04}_{-0.05}$ | $-2.64^{+0.10}_{-0.10}$ | $-1.35^{+0.12}_{-0.13}$ | $-2.76^{+0.10}_{-0.14}$ | |
| 0.50–0.71 | $-0.69^{+0.08}_{-0.09}$ | $-1.49^{+0.05}_{-0.06}$ | $-1.55^{+0.05}_{-0.04}$ | $-2.81^{+0.09}_{-0.12}$ | $-1.38^{+0.10}_{-0.11}$ | $-2.98^{+0.15}_{-0.26}$ | |
| 0.71–1.00 | $-0.92^{+0.08}_{-0.07}$ | $-1.59^{+0.05}_{-0.05}$ | $-1.49^{+0.04}_{-0.04}$ | $-2.84^{+0.06}_{-0.06}$ | $-1.31^{+0.06}_{-0.07}$ | $-4.13^{+0.55}_{-1.87}$ | |
| 1.00–1.42 | $-0.95^{+0.05}_{-0.05}$ | $-1.59^{+0.03}_{-0.04}$ | $-1.55^{+0.03}_{-0.04}$ | $-2.85^{+0.05}_{-0.05}$ | $-1.31^{+0.05}_{-0.05}$ | $-3.23^{+0.13}_{-0.12}$ | |
| 1.42–2.00 | $-0.96^{+0.06}_{-0.05}$ | $-1.59^{+0.04}_{-0.04}$ | $-1.58^{+0.03}_{-0.03}$ | $-2.83^{+0.04}_{-0.05}$ | $-1.26^{+0.05}_{-0.06}$ | $-3.06^{+0.08}_{-0.09}$ | |
| v_{LOS} (km s^{-1}) | D_{LOS} (pMpc) | HI | OVI | NV | CIV | CIII | SiIV |
| 0–30 | 0.00–0.13 | $0.68^{+0.36}_{-0.26}$ | $-0.78^{+0.09}_{-0.15}$ | $-1.27^{+0.10}_{-0.15}$ | $-2.03^{+0.28}_{-0.33}$ | $-0.46^{+0.50}_{-0.23}$ | $-2.47^{+0.21}_{-0.39}$ |
| 30–42 | 0.13–0.18 | $0.54^{+0.29}_{-0.36}$ | $-0.90^{+0.15}_{-0.31}$ | $-1.54^{+0.24}_{-0.15}$ | $-2.24^{+0.31}_{-0.37}$ | $-0.75^{+0.87}_{-0.26}$ | $-2.75^{+0.54}_{-3.25}$ |
| 42–60 | 0.18–0.25 | $0.39^{+0.43}_{-0.23}$ | $-0.78^{+0.12}_{-0.15}$ | $-1.58^{+0.15}_{-0.17}$ | $-2.00^{+0.22}_{-0.16}$ | $-0.53^{+0.37}_{-0.18}$ | $-2.16^{+0.27}_{-0.23}$ |
| 60–84 | 0.25–0.36 | $0.18^{+0.31}_{-0.26}$ | $-0.85^{+0.07}_{-0.20}$ | $-1.51^{+0.07}_{-0.13}$ | $-2.40^{+0.31}_{-0.23}$ | $-0.83^{+0.14}_{-0.18}$ | $-2.43^{+0.18}_{-0.28}$ |
| 84–119 | 0.36–0.50 | $-0.12^{+0.34}_{-0.32}$ | $-0.96^{+0.12}_{-0.15}$ | $-1.69^{+0.12}_{-0.12}$ | $-2.33^{+0.19}_{-0.20}$ | $-1.02^{+0.26}_{-0.21}$ | $-2.71^{+0.27}_{-0.33}$ |
| 119–169 | 0.50–0.71 | $-0.21^{+0.43}_{-0.34}$ | $-1.11^{+0.13}_{-0.10}$ | $-1.47^{+0.06}_{-0.07}$ | $-2.26^{+0.15}_{-0.20}$ | $-1.06^{+0.15}_{-0.19}$ | $-2.52^{+0.14}_{-0.21}$ |
| 169–238 | 0.71–1.00 | $-0.53^{+0.15}_{-0.12}$ | $-1.28^{+0.10}_{-0.14}$ | $-1.55^{+0.10}_{-0.10}$ | $-2.72^{+0.22}_{-0.22}$ | $-1.22^{+0.17}_{-0.16}$ | $-2.57^{+0.18}_{-0.51}$ |
| 238–336 | 1.00–1.42 | $-0.85^{+0.13}_{-0.11}$ | $-1.58^{+0.17}_{-0.19}$ | $-1.45^{+0.06}_{-0.06}$ | $-2.69^{+0.15}_{-0.14}$ | $-1.33^{+0.17}_{-0.21}$ | $-3.09^{+0.28}_{-0.72}$ |
| 336–475 | 1.42–2.00 | $-1.39^{+0.13}_{-0.10}$ | $-1.52^{+0.14}_{-0.14}$ | $-1.59^{+0.08}_{-0.10}$ | $-2.80^{+0.15}_{-0.16}$ | $-1.33^{+0.09}_{-0.08}$ | $-6.00^{+2.41}_{-0.00}$ |
| 475–671 | 2.00–2.83 | $-1.22^{+0.11}_{-0.11}$ | $-1.75^{+0.14}_{-0.21}$ | $-1.50^{+0.07}_{-0.07}$ | $-2.84^{+0.15}_{-0.15}$ | $-1.11^{+0.15}_{-0.12}$ | $-3.16^{+0.34}_{-1.35}$ |
| 671–948 | 2.83–3.99 | $-1.15^{+0.09}_{-0.09}$ | $-1.64^{+0.16}_{-0.18}$ | $-1.48^{+0.07}_{-0.06}$ | $-2.88^{+0.14}_{-0.12}$ | $-1.20^{+0.15}_{-0.17}$ | $-3.13^{+0.21}_{-0.24}$ |
| 948–1339 | 3.99–5.64 | $-1.10^{+0.09}_{-0.09}$ | $-1.53^{+0.11}_{-0.10}$ | $-1.57^{+0.05}_{-0.06}$ | $-2.94^{+0.12}_{-0.12}$ | $-1.37^{+0.16}_{-0.19}$ | $-3.67^{+0.40}_{-2.33}$ |
| $\log_{10}(\tau_{Z,\text{rnd}})$ | | -1.29 | -1.64 | -1.57 | -2.95 | -1.27 | -3.16 |

trace the HI profile, OVI, CIV and SiIV appear to be *more enhanced* than HI out to $\sim 1 \text{ pMpc}$ or 240 km s^{-1} . This result suggests that we might be seeing two different gas phases, i.e. a relatively compact one traced mainly by HI and CIII, and a phase that is more extended in real and/or velocity space and that is traced by OVI, CIV and SiIV.

We again point out that any fluctuations in the normalised optical depth values for the metal ions are magnified in these figures, due to the lower dynamic range of optical depths. Although this makes it difficult to draw secure conclusions about any observed differences in the distributions of the metals with respect to each other and to HI, we can at least say that the strong HI enhancement seen along the LOS direction is also present for the metal ions OVI, CIV, CIII and SiIV.

4.3 3-D Hubble distance

If we assume that the velocity differences between galaxies and the nearby absorption regions in the quasar are due only to Hubble flow, then we can calculate the 3-D Hubble distance as $\sqrt{b^2 + (H(z)\Delta v)^2}$, where b is the galaxy impact parameter, $H(z)$ is the Hubble parameter, and Δv is the

LOS separation between the absorber and the galaxy. We have computed the 3-D Hubble distance for every galaxy-pixel pair, divided them into 0.15 dex distance bins as in Figure 4, and taken the median optical depth in every bin. The result is plotted in Figure 8, and the data are given in Table 6. We stress that this metric is a poor approximation for distances $\lesssim 1 \text{ pMpc}$ since Figure 5 revealed strong anisotropies along the LOS on this scale, and we have shaded the poor-approximation region grey in Figure 8.

Although using the Hubble distance results in the loss of some important information, by using this projection we are able to achieve higher S/N ratios because each 3-D bin contains many more pixels than those constructed from cuts through the median optical depth maps. Specifically, we are able to see a significant enhancement of optical depth above the median for HI out to $\sim 2.8 \text{ pMpc}$ (99.5% confidence) and for CIV out to $\sim 4.0 \text{ pMpc}$ (90% confidence)². The latter result suggests that the enhancement of CIV above

² We note that in the eighth 3-D Hubble distance bin, which runs from 1.0–1.4 pMpc, we only detect the CIV enhancement with a confidence level of 80%.

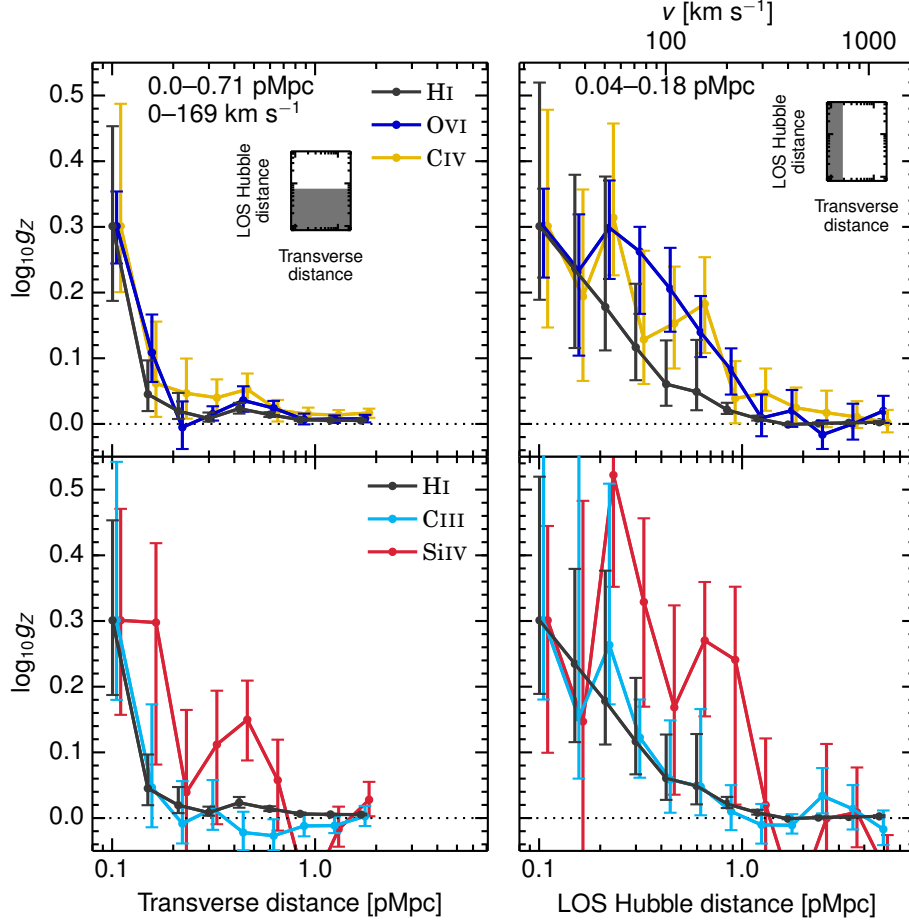


Figure 7. The same as Figure 6, but after re-scaling the optical depths using Equation 9 to account for differences in transition strengths and detection limits. Note that HI is shown in both the top and bottom panels, while NV has been removed. In general, the shapes of the rescaled metal optical depth profiles appear similar to that of HI, although OVI, CIV and SiIV are somewhat enhanced relative to HI along the LOS direction.

Table 6. The median $\log_{10}\tau_Z$ and 1σ errors as a function of 3-D Hubble distance (left column). Columns 2–7 display values for the different ions Z studied in this work, and the data are plotted in Figure 8. For comparison, the bottom row of the table lists the median optical depths measured over the full redshift range of each ion ($\tau_{Z,\text{rnd}}$).

| v_{Hubble} (km s^{-1}) | D_{Hubble} (pMpc) | HI | OVI | Nv | CIV | CIII | Siiv |
|--|----------------------------|-------------------------|-------------------------|-------------------------|-------------------------|-------------------------|-------------------------|
| 0–30 | 0.00–0.13 | $1.16^{+1.39}_{+0.38}$ | $-0.66^{+0.07}_{-0.14}$ | $-1.19^{+0.11}_{-0.08}$ | $-1.81^{+0.63}_{-0.47}$ | $-0.46^{+4.46}_{-0.24}$ | $-2.75^{+0.29}_{-3.25}$ |
| 30–42 | 0.13–0.18 | $0.67^{+0.24}_{-0.28}$ | $-0.88^{+0.15}_{-0.19}$ | $-1.22^{+0.07}_{-0.07}$ | $-1.89^{+0.26}_{-0.34}$ | $-0.03^{+0.34}_{-0.51}$ | $-2.18^{+0.30}_{-0.56}$ |
| 42–60 | 0.18–0.25 | $0.30^{+0.14}_{-0.23}$ | $-1.01^{+0.11}_{-0.12}$ | $-1.48^{+0.09}_{-0.12}$ | $-2.36^{+0.21}_{-0.24}$ | $-0.84^{+0.21}_{-0.17}$ | $-2.68^{+0.29}_{-0.40}$ |
| 60–84 | 0.25–0.36 | $-0.31^{+0.24}_{-0.18}$ | $-1.39^{+0.11}_{-0.11}$ | $-1.55^{+0.08}_{-0.06}$ | $-2.52^{+0.09}_{-0.10}$ | $-1.13^{+0.08}_{-0.10}$ | $-2.59^{+0.12}_{-0.21}$ |
| 84–119 | 0.36–0.50 | $-0.42^{+0.08}_{-0.10}$ | $-1.33^{+0.08}_{-0.09}$ | $-1.55^{+0.06}_{-0.05}$ | $-2.56^{+0.10}_{-0.11}$ | $-1.19^{+0.10}_{-0.09}$ | $-2.80^{+0.13}_{-0.13}$ |
| 119–169 | 0.50–0.71 | $-0.71^{+0.08}_{-0.19}$ | $-1.48^{+0.05}_{-0.04}$ | $-1.57^{+0.03}_{-0.04}$ | $-2.70^{+0.05}_{-0.05}$ | $-1.37^{+0.09}_{-0.07}$ | $-2.82^{+0.08}_{-0.11}$ |
| 169–238 | 0.71–1.00 | $-0.80^{+0.05}_{-0.06}$ | $-1.53^{+0.04}_{-0.04}$ | $-1.55^{+0.03}_{-0.03}$ | $-2.83^{+0.05}_{-0.05}$ | $-1.33^{+0.05}_{-0.05}$ | $-3.22^{+0.05}_{-0.17}$ |
| 238–336 | 1.00–1.42 | $-0.95^{+0.03}_{-0.03}$ | $-1.59^{+0.02}_{-0.03}$ | $-1.55^{+0.02}_{-0.02}$ | $-2.88^{+0.03}_{-0.03}$ | $-1.31^{+0.03}_{-0.03}$ | $-3.36^{+0.09}_{-0.17}$ |
| 336–475 | 1.42–2.00 | $-1.08^{+0.03}_{-0.02}$ | $-1.59^{+0.02}_{-0.02}$ | $-1.56^{+0.01}_{-0.01}$ | $-2.86^{+0.02}_{-0.02}$ | $-1.31^{+0.03}_{-0.03}$ | $-3.11^{+0.04}_{-0.07}$ |
| 475–671 | 2.00–2.83 | $-1.19^{+0.02}_{-0.02}$ | $-1.63^{+0.02}_{-0.02}$ | $-1.54^{+0.01}_{-0.01}$ | $-2.89^{+0.02}_{-0.02}$ | $-1.24^{+0.02}_{-0.03}$ | $-3.10^{+0.04}_{-0.05}$ |
| 671–948 | 2.83–3.99 | $-1.26^{+0.02}_{-0.02}$ | $-1.65^{+0.02}_{-0.02}$ | $-1.52^{+0.01}_{-0.01}$ | $-2.90^{+0.02}_{-0.02}$ | $-1.28^{+0.02}_{-0.02}$ | $-3.07^{+0.04}_{-0.04}$ |
| 948–1339 | 3.99–5.64 | $-1.29^{+0.02}_{-0.02}$ | $-1.64^{+0.02}_{-0.02}$ | $-1.59^{+0.01}_{-0.01}$ | $-2.92^{+0.02}_{-0.02}$ | $-1.27^{+0.02}_{-0.02}$ | $-3.13^{+0.04}_{-0.04}$ |
| $\log_{10}(\tau_{Z,\text{rnd}})$ | | -1.29 | -1.64 | -1.57 | -2.95 | -1.27 | -3.16 |

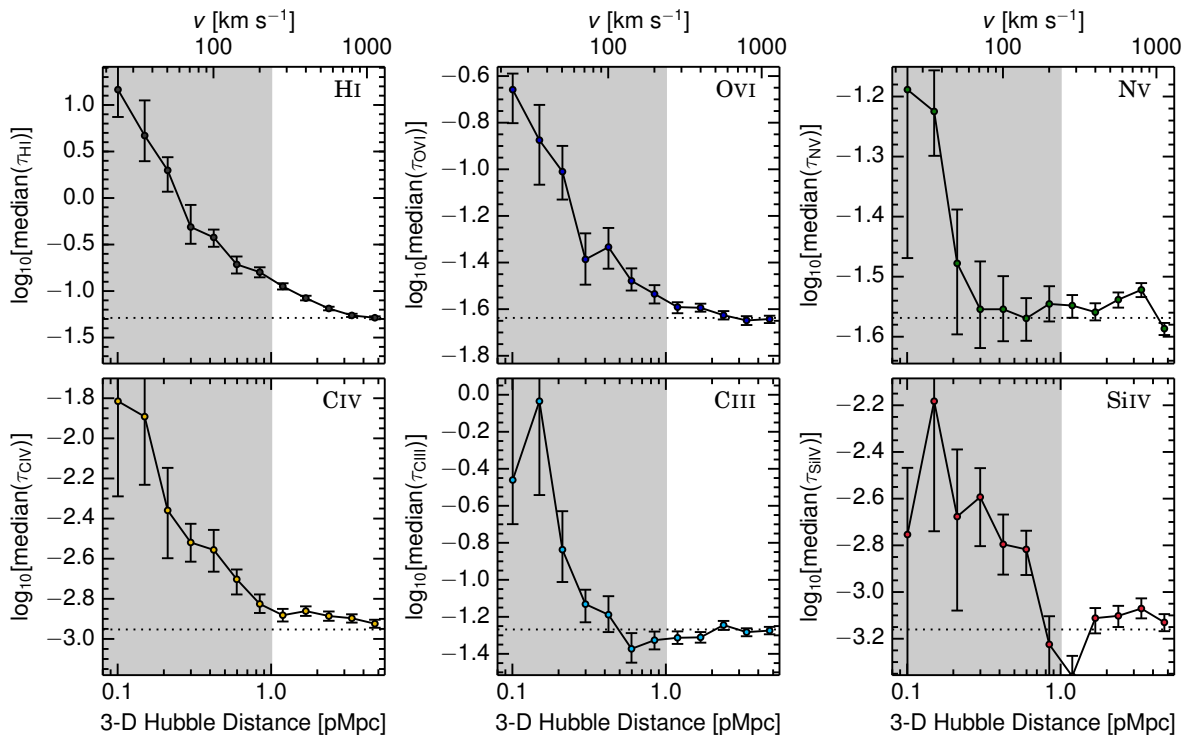


Figure 8. The median optical depth as a function of 3-D Hubble distance for all galaxies in our sample, assuming that velocity differences between the galaxies and associated absorption regions are purely due to Hubble flow. This assumption is certainly incorrect for $\lesssim 1$ pMpc, and we have therefore greyed out the regions that we believe are effected by redshift-space distortions. The horizontal dotted black lines indicate the median optical depth for all pixels of the ion shown. One advantage of examining 3-D Hubble distance is that it allows us to decrease the noise by combining large numbers of pixels, particularly at large distances. As a result, the enhancement in the median optical depth of CIV can now be detected out to ~ 4 pMpc.

the median seen throughout the 2-D map in Figure 4 is a real effect. We note that for NV, the enhancement seen at ~ 900 km s $^{-1}$ is likely due to residual contamination from its own doublet.

4.4 Covering fraction

The results from § 4.1 tell us about the median optical depths as a function of distance from galaxies. However, we are also interested in the rate of occurrence of relatively high optical depth (and hence more rare) systems. To quantify this, we use the covering fraction, which we define as the fraction of galaxies in a particular impact parameter bin for which the median pixel optical depth within ± 170 km s $^{-1}$ of the galaxy exceeds some threshold value $\tau_{Z,\text{thresh}}$. We have checked that the results remain unchanged using a larger velocity interval of ± 300 km s $^{-1}$.

To see which values of $\tau_{Z,\text{thresh}}$ may be informative, for each ion Z we calculate the median optical depth for 1000 random ± 170 km s $^{-1}$ regions selected from the full recovered redshift range, which are taken to represent typical IGM values. We then select the $\tau_{Z,\text{thresh}}$ values for which the covering fractions of the 1000 random regions are 0.25, 0.05, and 0.01 (the exact values of $\tau_{Z,\text{thresh}}$ for each ion are displayed in Figure 9). In Appendix C we instead use an

EW threshold and find that our conclusions still hold. The covering fractions for HI and each metal, as a function of impact parameter and for different values of $\tau_{Z,\text{thresh}}$ are shown in Figure 9 and Table 7, with the associated random region covering fraction denoted by the horizontal dashed lines.

First we examine values of $\tau_{Z,\text{thresh}}$ for which the IGM covering fraction is 0.25 and 0.05 (red circles and blue diamonds respectively). In every case except for NV, we observe elevated covering fractions within the two smallest impact parameter bins. For larger impact parameters, the HI covering fraction is higher than the IGM value out to 2 pMpc, which is in agreement with § 5 of Rudie et al. (2012). Additionally, OVI and in particular CIV both have covering fractions significantly above that of the IGM along the full range of impact parameters. This is consistent with the finding that we are able to detect levels of CIV optical depth enhancement above the median IGM value at all impact parameters probed (Figures 4 and 6). Again, the fact that for impact parameters $\gtrsim 180$ pkpc we only see significantly enhanced covering fractions for HI, OVI, and CIV does not necessarily mean that the other metal ions are not present, but could rather be due to contamination and noise preventing us from probing low enough optical depths, and could also be due to changes in the ionisation level of the gas.

Table 7. Covering fraction and 1σ errors as a function of transverse distance (top row), which is defined as the fraction of galaxies in each impact parameter bin that have a median optical depth within $\pm 170 \text{ km s}^{-1}$ above some threshold value. The threshold values are set by the optical depth at which the covering fraction of 1000 random $\pm 170 \text{ km s}^{-1}$ regions, f_{IGM} , are equal to 0.25, 0.05, and 0.01 (second column), and the results are plotted in Figure 9.

| D_{trans} (pMpc) | | 0.04–0.13 | 0.13–0.18 | 0.18–0.25 | 0.25–0.36 | 0.36–0.50 | 0.50–0.71 | 0.71–1.00 | 1.00–1.42 | 1.42–2.00 |
|---------------------------|------------------|------------------------|------------------------|------------------------|------------------------|------------------------|------------------------|------------------------|------------------------|------------------------|
| Ion | f_{IGM} | | | | | | | | | |
| HI | 0.25 | $1.00^{+0.00}_{-0.00}$ | $0.80^{+0.10}_{-0.10}$ | $0.64^{+0.18}_{-0.18}$ | $0.54^{+0.08}_{-0.12}$ | $0.61^{+0.07}_{-0.07}$ | $0.57^{+0.05}_{-0.05}$ | $0.43^{+0.05}_{-0.04}$ | $0.45^{+0.03}_{-0.03}$ | $0.45^{+0.03}_{-0.03}$ |
| | 0.05 | $0.83^{+0.08}_{-0.08}$ | $0.50^{+0.10}_{-0.10}$ | $0.27^{+0.09}_{-0.09}$ | $0.19^{+0.08}_{-0.08}$ | $0.25^{+0.05}_{-0.05}$ | $0.19^{+0.04}_{-0.04}$ | $0.14^{+0.03}_{-0.03}$ | $0.13^{+0.02}_{-0.02}$ | $0.14^{+0.02}_{-0.02}$ |
| | 0.01 | $0.42^{+0.17}_{-0.17}$ | $0.20^{+0.10}_{-0.10}$ | $0.09^{+0.09}_{-0.09}$ | $0.04^{+0.04}_{-0.04}$ | $0.14^{+0.05}_{-0.05}$ | $0.07^{+0.03}_{-0.03}$ | $0.02^{+0.02}_{-0.02}$ | $0.04^{+0.01}_{-0.01}$ | $0.04^{+0.01}_{-0.01}$ |
| OVI | 0.25 | $0.83^{+0.08}_{-0.08}$ | $0.64^{+0.18}_{-0.18}$ | $0.36^{+0.18}_{-0.18}$ | $0.27^{+0.08}_{-0.08}$ | $0.35^{+0.05}_{-0.05}$ | $0.36^{+0.06}_{-0.06}$ | $0.31^{+0.05}_{-0.04}$ | $0.32^{+0.03}_{-0.03}$ | $0.31^{+0.03}_{-0.03}$ |
| | 0.05 | $0.58^{+0.17}_{-0.17}$ | $0.27^{+0.18}_{-0.18}$ | $0.09^{+0.09}_{-0.09}$ | $0.04^{+0.04}_{-0.04}$ | $0.16^{+0.05}_{-0.05}$ | $0.04^{+0.01}_{-0.03}$ | $0.09^{+0.02}_{-0.02}$ | $0.08^{+0.02}_{-0.02}$ | $0.07^{+0.02}_{-0.02}$ |
| | 0.01 | $0.08^{+0.08}_{-0.08}$ | $0.09^{+0.09}_{-0.09}$ | $0.00^{+0.00}_{-0.00}$ | $0.00^{+0.00}_{-0.00}$ | $0.04^{+0.02}_{-0.02}$ | $0.01^{+0.01}_{-0.01}$ | $0.03^{+0.02}_{-0.02}$ | $0.03^{+0.01}_{-0.01}$ | $0.02^{+0.01}_{-0.01}$ |
| NV | 0.25 | $0.42^{+0.17}_{-0.17}$ | $0.27^{+0.11}_{-0.09}$ | $0.20^{+0.10}_{-0.10}$ | $0.32^{+0.07}_{-0.11}$ | $0.25^{+0.05}_{-0.05}$ | $0.26^{+0.06}_{-0.06}$ | $0.34^{+0.04}_{-0.04}$ | $0.33^{+0.03}_{-0.03}$ | $0.27^{+0.03}_{-0.03}$ |
| | 0.05 | $0.00^{+0.00}_{-0.00}$ | $0.09^{+0.09}_{-0.09}$ | $0.10^{+0.10}_{-0.10}$ | $0.04^{+0.04}_{-0.04}$ | $0.04^{+0.02}_{-0.02}$ | $0.06^{+0.03}_{-0.03}$ | $0.08^{+0.02}_{-0.02}$ | $0.06^{+0.01}_{-0.01}$ | $0.05^{+0.01}_{-0.01}$ |
| | 0.01 | $0.00^{+0.00}_{-0.00}$ | $0.00^{+0.00}_{-0.00}$ | $0.00^{+0.00}_{-0.00}$ | $0.00^{+0.00}_{-0.00}$ | $0.00^{+0.00}_{-0.00}$ | $0.00^{+0.00}_{-0.00}$ | $0.00^{+0.00}_{-0.00}$ | $0.00^{+0.00}_{-0.00}$ | $0.00^{+0.00}_{-0.00}$ |
| CIV | 0.25 | $0.77^{+0.08}_{-0.09}$ | $0.45^{+0.18}_{-0.09}$ | $0.55^{+0.18}_{-0.18}$ | $0.46^{+0.07}_{-0.11}$ | $0.46^{+0.07}_{-0.07}$ | $0.37^{+0.05}_{-0.05}$ | $0.24^{+0.04}_{-0.04}$ | $0.34^{+0.04}_{-0.03}$ | $0.35^{+0.03}_{-0.03}$ |
| | 0.05 | $0.62^{+0.15}_{-0.15}$ | $0.18^{+0.09}_{-0.09}$ | $0.18^{+0.09}_{-0.09}$ | $0.14^{+0.07}_{-0.07}$ | $0.24^{+0.05}_{-0.05}$ | $0.09^{+0.03}_{-0.03}$ | $0.11^{+0.03}_{-0.03}$ | $0.09^{+0.02}_{-0.02}$ | $0.12^{+0.02}_{-0.02}$ |
| | 0.01 | $0.15^{+0.08}_{-0.08}$ | $0.09^{+0.09}_{-0.09}$ | $0.00^{+0.00}_{-0.00}$ | $0.00^{+0.00}_{-0.00}$ | $0.03^{+0.03}_{-0.02}$ | $0.01^{+0.01}_{-0.01}$ | $0.01^{+0.01}_{-0.01}$ | $0.01^{+0.01}_{-0.01}$ | $0.01^{+0.01}_{-0.01}$ |
| CIII | 0.25 | $0.60^{+0.20}_{-0.20}$ | $0.43^{+0.14}_{-0.14}$ | $0.29^{+0.14}_{-0.14}$ | $0.29^{+0.10}_{-0.10}$ | $0.27^{+0.07}_{-0.07}$ | $0.24^{+0.06}_{-0.06}$ | $0.25^{+0.04}_{-0.04}$ | $0.20^{+0.03}_{-0.03}$ | $0.31^{+0.03}_{-0.03}$ |
| | 0.05 | $0.30^{+0.10}_{-0.10}$ | $0.14^{+0.14}_{-0.14}$ | $0.00^{+0.00}_{-0.00}$ | $0.05^{+0.05}_{-0.05}$ | $0.05^{+0.02}_{-0.02}$ | $0.08^{+0.04}_{-0.04}$ | $0.02^{+0.01}_{-0.01}$ | $0.03^{+0.01}_{-0.01}$ | $0.05^{+0.01}_{-0.01}$ |
| | 0.01 | $0.00^{+0.00}_{-0.00}$ | $0.00^{+0.00}_{-0.00}$ | $0.00^{+0.00}_{-0.00}$ | $0.00^{+0.00}_{-0.00}$ | $0.00^{+0.00}_{-0.00}$ | $0.00^{+0.00}_{-0.00}$ | $0.00^{+0.00}_{-0.00}$ | $0.00^{+0.00}_{-0.00}$ | $0.00^{+0.00}_{-0.00}$ |
| SIV | 0.25 | $0.50^{+0.17}_{-0.17}$ | $0.56^{+0.22}_{-0.11}$ | $0.38^{+0.12}_{-0.12}$ | $0.35^{+0.12}_{-0.12}$ | $0.37^{+0.06}_{-0.06}$ | $0.30^{+0.05}_{-0.07}$ | $0.20^{+0.04}_{-0.04}$ | $0.25^{+0.03}_{-0.03}$ | $0.26^{+0.03}_{-0.03}$ |
| | 0.05 | $0.25^{+0.17}_{-0.08}$ | $0.11^{+0.11}_{-0.11}$ | $0.00^{+0.00}_{-0.00}$ | $0.12^{+0.06}_{-0.06}$ | $0.10^{+0.04}_{-0.04}$ | $0.07^{+0.03}_{-0.03}$ | $0.04^{+0.02}_{-0.02}$ | $0.06^{+0.02}_{-0.02}$ | $0.06^{+0.02}_{-0.02}$ |
| | 0.01 | $0.17^{+0.08}_{-0.08}$ | $0.11^{+0.11}_{-0.11}$ | $0.00^{+0.00}_{-0.00}$ | $0.06^{+0.06}_{-0.06}$ | $0.06^{+0.04}_{-0.04}$ | $0.03^{+0.02}_{-0.02}$ | $0.00^{+0.00}_{-0.00}$ | $0.01^{+0.01}_{-0.01}$ | $0.01^{+0.01}_{-0.01}$ |

Finally, turning our attention to the values of $\tau_{\text{Z,thresh}}$ for which the IGM covering fraction is 0.01 (yellow squares), only HI, CIV, and SIV show significant enhancement at small impact parameters. This suggests that for the ions bluewards of Ly α , the highest optical depth values are largely the result of contamination. Furthermore, HI and CIV no longer have enhanced covering fractions at large impact parameters, which suggests that the rare, high optical depth systems are preferentially located very near galaxies.

Here we address the two major transverse direction enhancement extents seen in HI and the metal ions: a strong enhancement (out to $\approx 180 \text{ pkpc}$) and a weak enhancement (out to $\approx 2 \text{ pMpc}$). We have observed the strong enhancement for all ions studied out to $\approx 180 \text{ pkpc}$, in both the transverse cuts (left panels of Figure 6) and the covering fraction (Figure 9). To put this distance into context, we take the comoving number density of identically selected galaxies in this survey from Reddy et al. (2008), which is $\Phi = 3.7 \times 10^{-3} \text{ cMpc}^{-3}$ (for $\mathcal{R} \leq 25.5$). From this, we can infer that the regions within 180 pkpc around galaxies comprise only $\sim 0.4\%$ of the total volume of the universe. In spite of being present in a very small volume, the high optical depths and covering fractions within this distance indicate that these regions contain substantial amounts of HI and metals ions.

The second, weaker enhancement out to $\approx 2 \text{ pMpc}$ can be seen for HI and CIV (and marginally for OVI) in the

transverse-direction cuts (left panels of Figure 6), 3-D Hubble distance (Figure 8), and covering fraction (Figure 9).

Although the enhanced absorption observed on these scales is statistically significant, we note that 2 pMpc corresponds to $\sim 20\times$ the virial radii of the galaxies in our sample, far beyond the physical sphere of influence of the galaxies centred at the origins of these figures. Performing the same calculation as above, to determine the fraction of the volume of the Universe within 2 pMpc of these galaxies results in a value that exceeds unity – i.e., if these galaxies were uniformly distributed, all of space would lie within 2 pMpc of a galaxies that meets these selection criteria. However, it is well established that galaxies are clustered (e.g., Adelberger et al. 2005b), so we would expect many of the “spheres” from our simple calculation to be overlapping.

Indeed, Rudie et al. (2012) noted that the galaxy-galaxy autocorrelation scale-length for this same sample of galaxies has been measured to be $\approx 2.8 \text{ pMpc}$ (Trainor & Steidel 2012), which certainly suggests that the 2-halo term plays a role in the enhancement at large scales. Another possibility is that we are seeing metals in the IGM; in reality we are likely observing a combination of both CGM metals from other clustered galaxies, as well as some truly intergalactic metals.

Studies by Adelberger et al. (2003) at $z \sim 3$ and Adelberger et al. (2005a) at $z \sim 2.5$, using decrements in transmitted flux, found evidence for elevated (with respect to random IGM positions) HI absorption out to impact param-

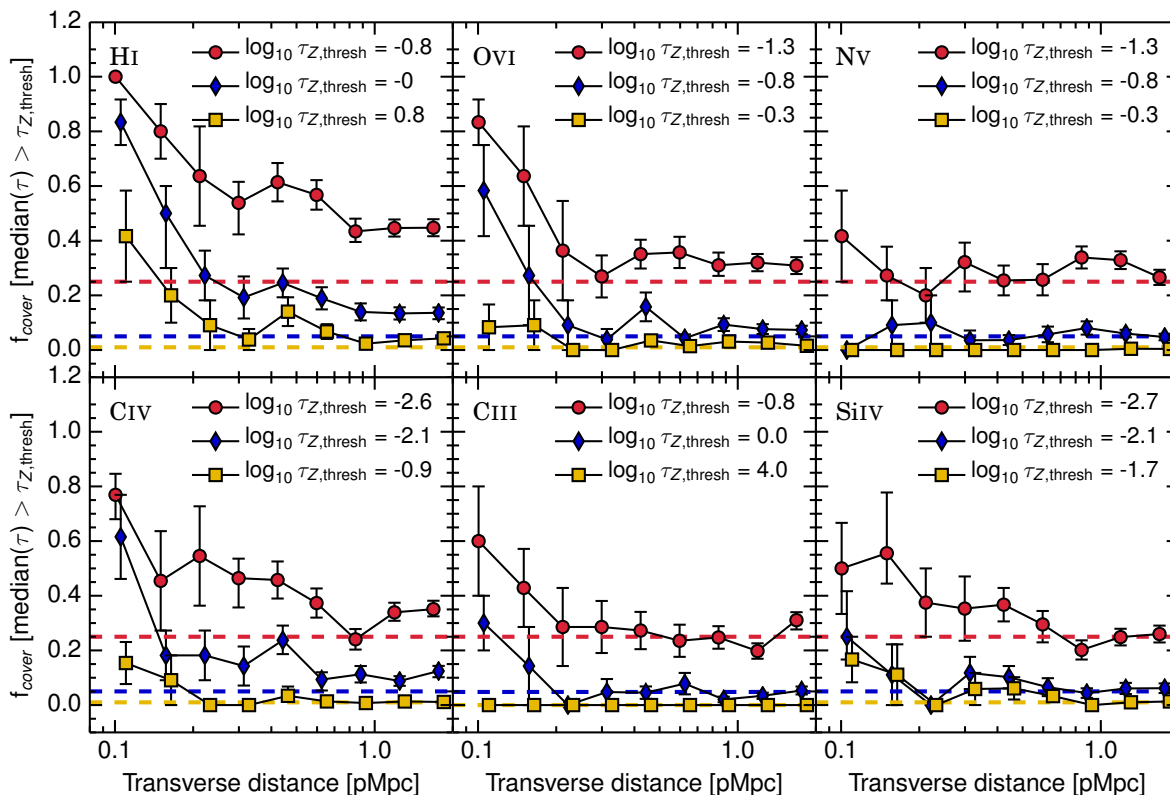


Figure 9. Covering fraction for each ion, defined as the fraction of galaxies within some impact parameter bin that have a median optical depth within $\pm 170 \text{ km s}^{-1}$ above some threshold value. These values are chosen to be the optical depths for which the covering fraction computed for 1000 random regions in the IGM is equal to 0.25 (red circles), 0.05 (blue diamonds), and 0.01 (yellow squares). The IGM covering fraction values are indicated by the horizontal dashed lines of corresponding colour. Points determined using different $\tau_{Z,\text{thresh}}$ values have been offset horizontally by 0.02 dex for clarity. We note that points where the covering fraction is 0 or 1 have no errorbar because bootstrapping galaxies from the same sample cannot change the covering fraction within that particular impact parameter bin.

eters of $\sim 2 \text{ pMpc}$. The authors also measured a strong correlation between the positions of CIV absorbers and galaxies, with the strength of the correlation increasing with absorber strength. Furthermore, at $z \sim 0.5$ Zhu et al. (2014) found MgII absorber and galaxy positions to be correlated out to $\sim 20 \text{ pMpc}$. The above results are certainly consistent with the fact that we are finding enhanced covering fractions for HI and CIV out to impact parameters of 2 pMpc.

4.5 Optical depth distributions

Up until this point we have only considered median optical depths. To acquire a sense of how individual pixel optical depth values are distributed, we have plotted their probability density functions (PDFs) for $\pm 170 \text{ km s}^{-1}$ regions around galaxies in Figure 10, where each panel shows a different ion. The galaxies are divided into the usual impact parameter bins (coloured lines), except for the final six bins which have been combined into three (with sizes of 0.30 dex for clarity). The values marked “sat.” are for pixels which we found to be saturated, and, in the case of HI, whose optical depths could not be recovered from higher order Lyman

series lines. We set the optical depth values of such pixels to 10^4 . We have also determined the PDFs for 1000 random regions in the IGM, which are shown by the black lines. Finally, for pixels which have negative optical depths, we have taken the log of their absolute values and plotted their PDFs using dashed lines.

First we consider the source of the positive optical depths, by comparing their distributions (solid lines) to those of negative optical depths (dashed lines), which we expect to reflect the level of shot-noise in the spectrum. Aside from the bins with impact parameters $< 0.18 \text{ pMpc}$, for CIV and SiIV the distributions of positive and negative optical depths are similar to each other, suggesting that most of the positive optical depths arise from shot noise around the level of the continuum. This is not surprising for ions with rest-frame wavelengths redwards of the QSO Ly α emission, i.e. regions that do not suffer from HI contamination. On the other hand, for the remaining ions, the negative optical depths contribute minimally to the full distribution, which means that the positive optical depths should primarily reflect real absorption (including contamination).

Figure 10 demonstrates that the scatter in optical

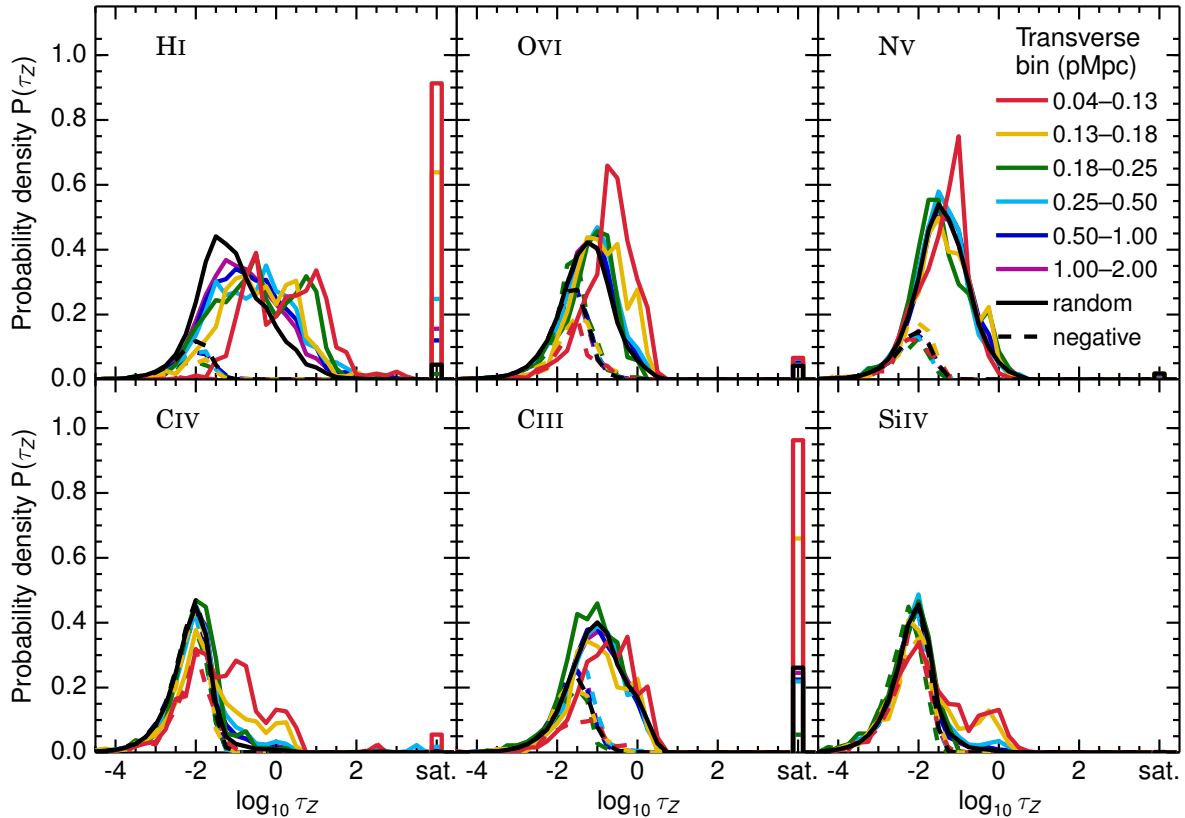


Figure 10. Pixel optical depth PDFs within $\pm 170 \text{ km s}^{-1}$ of galaxies divided by impact parameter bin (coloured lines), where each panel displays a different ion. We have used the usual binning scheme, but combined the last six bins to create three in order to reduce the number of lines plotted. The black line shows the PDF for 1000 random $\pm 170 \text{ km s}^{-1}$ regions within the full redshift range corresponding to each ion. The portion marked “sat” represents pixels that were found to be saturated, and for which the optical depth could not be recovered. The dashed lines show the PDFs for pixels which had negative optical depths, where we have taken the log of their absolute values. Except for NV, the PDFs for the two smallest impact parameter bins (and more for HI) tend to higher optical depth values compared to the PDF of random regions.

depths is quite large. Even for regions at small galactocentric distances, many optical depths reach values typical of random IGM regions (which may of course be close to undetected galaxies). However, except perhaps for NV, the optical depth PDFs of the 2 or 3 smallest impact parameter bins for each ion appear substantially different from the random region PDF, and in particular tend towards higher optical depth values.³

4.6 Equivalent widths

In studies where individual absorption lines are examined, EW is often used to parametrise their strength independently of the line shapes, and can also be computed using spectral stacking. Another advantage of employing EW as a metric is that it can be applied to spectra with low S/N

or resolution. In particular, to measure absorption at very small impact parameters (i.e., less than our smallest value of 35 pkpc), the usage of QSO-galaxy pairs is currently not viable, and instead galaxy-galaxy pairs (with much lower resolution spectra) must be used. By stacking such spectra to create mean flux profiles, Steidel et al. (2010) measured EW as a function of galaxy impact parameter (see their Figure 21 and their Table 4). We have plotted their results for the ions which are also in our sample (HI, CIV, and SiIV) in Figure 11. In addition to measuring EWs for small impact parameters by using galaxy-galaxy pairs, they also used galaxy-quasar pairs to calculate HI EWs for impact parameters of 128–280 pkpc, which we denote by the large black open circles. We note that the galaxy-quasar sample from Steidel et al. (2010) is comprised of the same QSOs and mostly the same galaxies as the sample used in this work.

We calculate typical EWs as a function of galaxy impact parameter by shifting the absorption spectrum (i.e. the associated region of the intervening QSO) of every galaxy to the rest-frame wavelength of the ion in question and com-

³ Unfortunately, because of spatial correlations between the optical depth pixels, the use of the Kolmogorov-Smirnov test to compare the PDFs is not appropriate for this data.

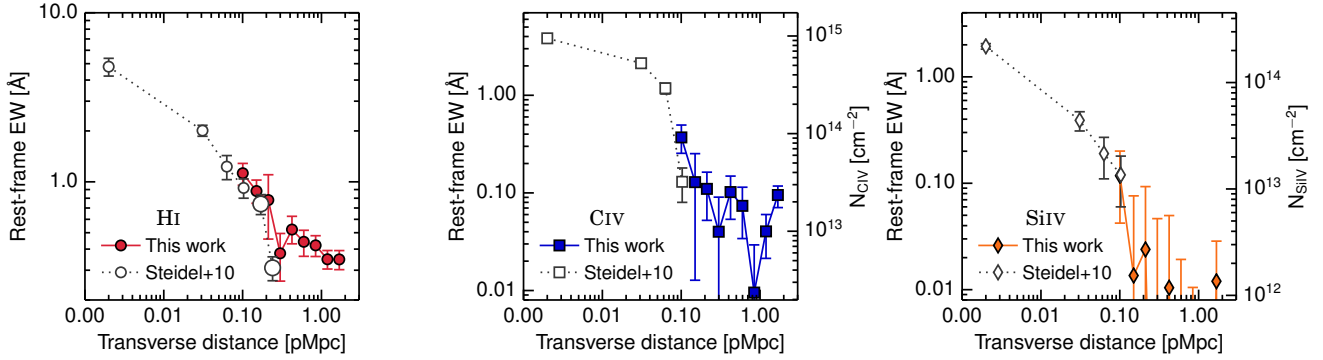


Figure 11. Rest-frame EW calculated using the mean spectrum within each galaxy impact parameter bin (filled points), where each panel shows a different ion. Here, the average spectrum was divided by the mean flux of all spectral pixels and the flux decrement was integrated over ± 500 km s $^{-1}$. Also plotted are EWs calculated using galaxy pairs from low-resolution spectra (open points) as well as H I EWs from galaxy-QSO pairs (left panel, large open circles at 128–280 pkpc) taken from Steidel et al. (2010). Note that for clarity, each panel has a different range along the y -axis. EWs were also calculated for an average spectrum created from 1000 random ± 500 km s $^{-1}$ regions, and the result was negative for all three ions. For reference, on the right-hand y -axis of the two rightmost panels we show the corresponding column density calculated from Equation 10, which assumes that the absorbers are on the linear portion of the curve-of-growth. At the point of overlap, $\sim 10^2$ pkpc, our points agree with Steidel et al. (2010), and although we do not see the sharp drop off at larger impact parameters predicted by their models, we do find consensus in the measured H I EWs at large impact parameters.

Table 8. Median EWs and 1σ errors (in \AA) calculated by integrating the normalised flux decrement over a ± 500 km s $^{-1}$ region as a function of transverse distance for H I, C IV and Si IV. These values are plotted in Figure 11. We also show two different column density estimates, $\log_{10} N^{\text{EW}}$ and $\log_{10} N_{\text{rec}}^{\text{EW}}$, where N is in cm $^{-2}$. N^{EW} was computed by applying Equation 10 to the EWs from the row above. $N_{\text{rec}}^{\text{EW}}$ was measured by performing the EW integration on the recovered optical depths converted back to flux, rather than on the observed flux as was done for N^{EW} , and then applying Equation 10. Empty values correspond to negative column densities (due to negative EWs), and u.l. denotes 1σ upper limits.

| D_{trans} (pMpc) | | 0.04–0.13 | 0.13–0.18 | 0.18–0.25 | 0.25–0.36 | 0.36–0.50 | 0.50–0.71 | 0.71–1.00 | 1.00–1.42 | 1.42–2.00 |
|---------------------------|--|---------------------------|---------------------------|---------------------------|---------------------------|---------------------------|-------------------------|---------------------------|-------------------------|---------------------------|
| Ion | | | | | | | | | | |
| H I | EW | $1.12^{+0.16}_{-0.17}$ | $0.88^{+0.14}_{-0.14}$ | $0.78^{+0.32}_{-0.32}$ | $0.38^{+0.12}_{-0.12}$ | $0.52^{+0.10}_{-0.09}$ | $0.44^{+0.08}_{-0.08}$ | $0.42^{+0.06}_{-0.06}$ | $0.35^{+0.04}_{-0.04}$ | $0.35^{+0.04}_{-0.05}$ |
| C IV | EW | $0.37^{+0.13}_{-0.12}$ | $0.13^{+0.12}_{-0.12}$ | $0.11^{+0.05}_{-0.06}$ | $0.04^{+0.05}_{-0.05}$ | $0.10^{+0.05}_{-0.05}$ | $0.07^{+0.04}_{-0.04}$ | $0.01^{+0.02}_{-0.02}$ | $0.04^{+0.02}_{-0.02}$ | $0.10^{+0.02}_{-0.02}$ |
| | $\log_{10} N^{\text{EW}}$ | $13.62^{+0.12}_{-0.18}$ | $13.16^{+0.28}_{-1.38}$ | $13.09^{+0.18}_{-0.29}$ | $12.66^{+0.36}_{-\infty}$ | $13.06^{+0.17}_{-0.27}$ | $12.92^{+0.19}_{-0.35}$ | $12.03^{+0.49}_{-\infty}$ | $12.66^{+0.17}_{-0.29}$ | $13.03^{+0.10}_{-0.12}$ |
| | $\log_{10} N_{\text{rec}}^{\text{EW}}$ | $13.55^{+0.11}_{-0.17}$ | $12.66^{+0.46}_{-\infty}$ | $12.66^{+0.30}_{-0.97}$ | $12.80^{+0.29}_{-1.37}$ | $12.70^{+0.25}_{-0.61}$ | 12.28 (u.l.) | ... | ... | $12.40^{+0.23}_{-0.42}$ |
| Si IV | EW | $0.12^{+0.08}_{-0.08}$ | $0.01^{+0.06}_{-0.07}$ | $0.02^{+0.07}_{-0.06}$ | $-0.01^{+0.05}_{-0.05}$ | $0.01^{+0.04}_{-0.04}$ | $-0.01^{+0.03}_{-0.03}$ | $-0.01^{+0.02}_{-0.02}$ | $-0.02^{+0.01}_{-0.01}$ | $0.01^{+0.02}_{-0.02}$ |
| | $\log_{10} N^{\text{EW}}$ | $13.12^{+0.22}_{-0.33}$ | $12.19^{+0.77}_{-\infty}$ | $12.43^{+0.57}_{-\infty}$ | 12.71 (u.l.) | $12.07^{+0.67}_{-\infty}$ | 12.28 (u.l.) | 12.09 (u.l.) | ... | $12.13^{+0.38}_{-\infty}$ |
| | $\log_{10} N_{\text{rec}}^{\text{EW}}$ | $12.83^{+0.33}_{-\infty}$ | 12.62 (u.l.) | ... | ... | ... | ... | ... | ... | ... |

putting the mean spectrum within the transverse distance bin. To simulate the effect of a suppressed continuum, as appropriate for the low-resolution spectra used in Steidel et al. (2010), we follow Rakic et al. (2012) and calculate the mean flux level of all pixels in all spectra within the wavelength region probed for a particular ion. We then divide the mean flux profile by this value before integrating the flux decrement over ± 500 km s $^{-1}$ to compute the EW. The results are given in Table 8 and Figure 11. We have verified that the conclusions presented here hold if we use 150, 300 and 600 km s $^{-1}$ intervals instead.

For overlapping impact parameter bins, we see good agreement between the two samples for H I and Si IV. Additionally, C IV shows good agreement when we compare the outer transverse distance bin of Steidel et al. (2010) with our

second-smallest bin. The models from Steidel et al. (2010) predict that when one extrapolates EWs to larger impact parameters, there is sharp drop in EW around impact parameters of $\sim 10^2$ pkpc for the metal ions and around ~ 200 pkpc for H I. We do not see such an effect in our data, where the EW values drop off relatively slowly with increasing transverse distance. However, the models were only intended to explain the behaviour of the EWs down to 0.1 \AA , and were insensitive to any plateau at smaller EW values. On the other hand, we find good agreement between both sets of measured H I EW values at large impact parameters, in spite of the differences in the galaxy sample, bin size, and EW measurement technique.

To ease comparison with other studies, we convert EW to column density as in Savage & Sembach (1991), assuming

the linear curve-of-growth regime (i.e. $\tau < 1$):

$$\begin{aligned} N &= 4\pi\epsilon_0 \frac{m_e c^2}{\pi e^2} \frac{EW}{f_{Z,k} \lambda_{Z,k}^2} \\ &= 1.13 \times 10^{20} \frac{1}{f_{Z,k}} \left(\frac{1\text{\AA}}{\lambda_{Z,k}} \right)^2 \left(\frac{EW}{1\text{\AA}} \right) \text{cm}^{-2} \end{aligned} \quad (10)$$

where ϵ_0 is the permittivity of free space, m_e is the electron mass, e is the electric charge, c is the speed of light, and $\lambda_{Z,k}$ and $f_{Z,k}$ are the rest-frame wavelength and oscillator strength of the k th transition of ion Z . Figure 10 demonstrates that the linear regime is not a valid assumption for HI since a substantial number of pixels have $\tau > 1$, however, we can still apply Equation 10 to CIV and SiIV.⁴ We show this conversion as a secondary vertical axis in Figure 11. In addition, in Table 8 we give the column densities computed from Equation 10 applied to the given EWs (N^{EW}). Furthermore, instead of calculating EW directly from the observed spectrum, we convert the recovered optical depths back to flux values, and integrate over those to determine column densities, which are also presented in Table 8 ($N_{\text{rec}}^{\text{EW}}$).

4.7 Galaxy redshift measurements

As discussed earlier, the various nebular and rest-frame UV-based galaxy redshifts suffer from different levels of uncertainty. In general, there is significantly more uncertainty associated with those redshifts determined from interstellar absorption or Ly α emission lines than with nebular redshifts measured by NIRSPEC or MOSFIRE. Since the elongation of the absorption enhancement along the LOS could be caused at least in part by redshift errors (e.g., Rakic et al. 2013), reducing them helps disentangle this effect from that of peculiar velocities. Currently, our galaxy sample has 381 galaxies with redshifts measured from nebular emission lines, and 340 of those are derived from MOSFIRE observations, which we estimate have errors of $\Delta v \approx 18 \text{ km s}^{-1}$ (compared to 41 galaxies with NIRSPEC measured redshifts that have an estimated error of $\Delta v \approx 60 \text{ km s}^{-1}$). The measurement errors from these instruments are much smaller than the $\sim 240 \text{ km s}^{-1}$ extent of elongation seen along the LOS.

Therefore, we experiment with using different subsamples of KBSS galaxies. In Figure 12, we again show the (unsmoothed) median optical depths from cuts taken along the maps in Figure 4, using the innermost bins and plotting points along the transverse direction (left columns) and LOS direction (right columns). The blue circles show the cuts constructed using the full galaxy sample and are identical to the points in Figure 6. We also consider the results when only galaxies whose redshifts were measured from nebular emission lines using NIRSPEC or MOSFIRE

⁴ Examining the curve-of-growth and assuming a Doppler parameter $b_D = 10 \text{ km s}^{-1}$, we find that the linear regime is valid for $N_{\text{CIV}} \lesssim 8 \times 10^{13} \text{ cm}^{-2}$ and $N_{\text{SiIV}} \lesssim 3 \times 10^{13} \text{ cm}^{-2}$. Furthermore, from visual inspection we conclude that the spectral regions around the 30 smallest impact parameter galaxies show no evidence for saturation in CIV and SiIV.

are used (381 galaxies or 45% of the full sample for HI, orange squares).

In general, we do not see any significant differences between the cuts taken from the fiducial sample and the one using only nebular redshifts. For the points along the transverse direction, one might expect that more accurate redshift measurements would result in an increase in the observed absorption. Although a small effect can be seen, that is, in most cases along the transverse direction the orange squares are at slightly higher optical depths than the blue circles, the result is not significant for any fixed transverse distance (although the increase in optical depths could be significant if integrated over the full impact parameter range).

We note that discrepancies between the two samples may be due to the different galaxies used to construct each optical depth profile. To test this, in Appendix D we take the 238 galaxies that have had *both* their nebular and rest-frame UV redshifts measured, and show the results determined using only one type of redshift measurement at a time in Figure D1. The slight enhancement along the transverse direction is no longer apparent in this comparison, so it may be a consequence of the different galaxies used in the nebular-only sample. However, it is important to note that in Figure D1 the number of galaxies in the sample is relatively small and hence that subtle differences may be hidden in the noise. Furthermore, in Figure D2 we directly plot our results against those from Rakic et al. (2012), where only 10% of the galaxy sample had redshifts measured from nebular emission lines. We find that the HI optical depths along the LOS agree between the two sample for the innermost bin, although the redshift error effects become apparent in larger impact parameter bins.

The most striking result from Figure 12 is that we do not observe significant differences between the LOS-direction optical depth profiles of the two galaxy samples. The lack of change in the extent of the optical depth enhancement when galaxy redshift errors are reduced from ~ 150 to $\sim 10 \text{ km s}^{-1}$ implies that the small-scale anisotropy detected for HI by Rakic et al. (2012) and Rudie et al. (2012), and for HI and metals in this work, originates from gas peculiar velocities rather than from redshift errors.

Finally, as in Rudie et al. (2012), we would like to extract the peculiar velocity field by subtracting the redshift errors ($\approx 18 \text{ km s}^{-1}$) and transverse extent of the absorption (180 pkpc or $\approx 42 \text{ km s}^{-1}$) in quadrature from the observed velocity enhancement; doing so results in $\sim \pm 240 \text{ km s}^{-1}$, and is in good agreement with the peculiar velocities measured in Rudie et al. (2012) of $\sim \pm 260 \text{ km s}^{-1}$. The magnitudes of the peculiar velocities we observe are consistent with what would be expected from infall, outflows, and virial velocities, so although it is currently difficult to disentangle the exact nature of their origin, it is likely that we are detecting motions of the gas around LBGs.

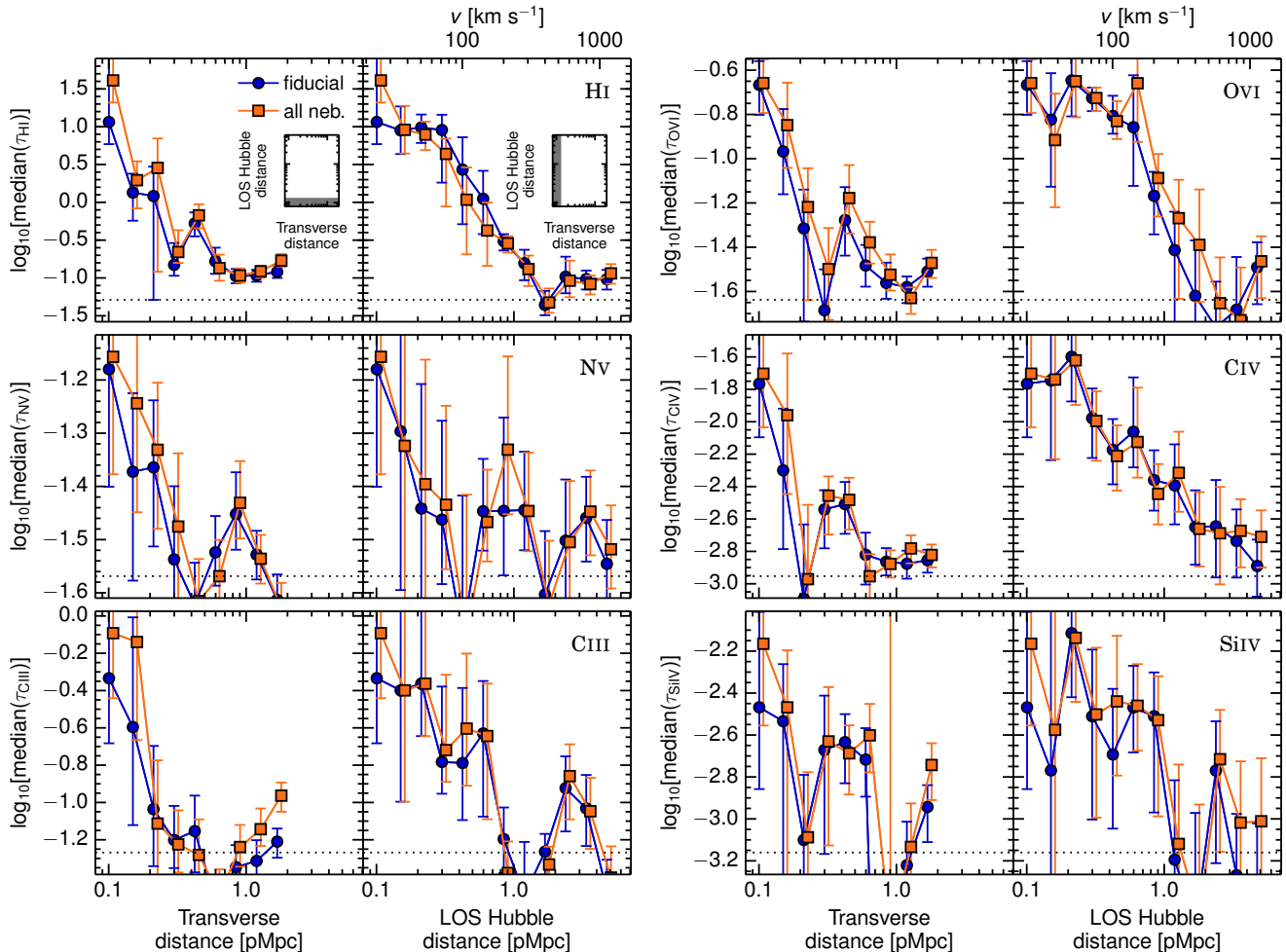


Figure 12. The median log optical depth $\tau_{Z,\text{rand}}$ where each set of two horizontal panels shows a different ion. The left and right panels in each set of two show points along the transverse and LOS directions, respectively. The cut sizes, shown in the insets, are the same as in Figure 6, i.e., 0–30 km s^{-1} and 0.04–0.18 pMpc for the points along the transverse and LOS directions, respectively. The results from the fiducial sample used throughout this work, which consists of galaxy redshifts measured using a mix of rest-frame UV lines and nebular emission lines, are shown by the blue circles (835 galaxies), while the orange squares indicate the medians from all galaxies that have their redshift measured using nebular emission lines (354 galaxies). Points have been offset horizontally by 0.03 dex for clarity. The elongation of the optical depth enhancement along the LOS does not decrease when the sample only contains galaxies with nebular redshifts, which indicates that redshift measurement errors do not contribute significantly to this effect.

5 SUMMARY AND CONCLUSIONS

We have studied metals in the CGM around 854 $z \approx 2\text{--}2.8$ galaxies taken from the KBSS. The sample contains 381 galaxies that have been observed with NIRSPEC and/or MOSFIRE, allowing us to measure their redshifts using nebular emission lines with estimated errors of only $\Delta v \approx 60 \text{ km s}^{-1}$ and $\Delta v \approx 18 \text{ km s}^{-1}$ for the two instruments, respectively. The galaxies studied lie in the fields of 15 hyper-luminous QSOs for which high-quality Keck spectra are available, with galaxy impact parameters ranging from 35 pkpc to 2 pMpc. Using the QSO spectra, the optical depth at each pixel in the Ly α forest redshift range was recovered for H I as well as for five metal ions (O VI, NV, CIV, C III, and Si IV). This was done using a slightly modified ver-

sion of the pixel optical depth technique of Aguirre et al. (2002), which corrects the optical depths for saturation and various forms of contamination.

The main results are summarised below:

(i) We have presented 2-D maps of the median absorption around galaxies in H I (first shown for a smaller sample by Rakic et al. 2012), as well as the first maps of O VI, NV, CIV, C III, and Si IV. These maps were created by taking the medians of the binned pixel optical depths as a function of the LOS and transverse distances from the galaxies in our sample (Figure 4, § 4.1).

(ii) For every ion studied except perhaps for NV, we measure an enhancement of the absorption at small galactocentric radii, out to ~ 180 pkpc in the transverse direction and

$\sim \pm 240 \text{ km s}^{-1}$ along the LOS ($\sim 1 \text{ pMpc}$ assuming pure Hubble flow). Inside this region the median optical depth is typically enhanced above that of random regions by about one order of magnitude for the metals and by two order of magnitude for HI (Figures 4 and 5, § 4.1).

(iii) In the transverse direction, HI and CIV show a slight enhancement out to the maximum impact parameter covered by the survey (2 pMpc). The non-detection of an enhancement in the other ions at such large impact parameters does not necessarily imply that these ions are not present; rather, it may reflect differences in detection limits (Figure 6, § 4.1).

(iv) The visual impression from the maps is that the enhancement of the HI is more extended in the transverse direction than that of the metals. However, normalising the optical depth profiles such that they all have the same maximum and asymptote, the metal ions do not show a significantly different profile shape (i.e. drop-off of optical depth values) with increasing transverse distance compared to HI. In the LOS direction, CIII traces the normalised HI profile, while OVI, CIV and SiIV show evidence for more extended absorption (Figure 7, § 4.2).

(v) Comparing cuts through the median optical depth maps in the transverse direction to those in the LOS direction, for all ions except NV the optical depths are higher in the LOS than in the transverse direction out to distances of $\sim 1 \text{ pMpc}$ (i.e. 240 km s^{-1}) (Figure 5, § 4.1).

(vi) We examined the median optical depth as a function of 3-D Hubble distance, which allows us to reduce the noise by combining pixels from both the LOS and transverse directions. Focusing on larger distance scales which should be minimally affected by redshift-space distortions (i.e. $\gtrsim 1 \text{ pMpc}$), we find the CIV optical depth to be slightly enhanced out to $\sim 4 \text{ pMpc}$. (Figure 8, § 4.3).

(vii) The pixel optical depth PDFs at all impact parameters and for random regions all show similar amounts of scatter. However, at small impact parameters, particularly in the two innermost bins (i.e. $< 180 \text{ pkpc}$), the distributions of optical depths are typically skewed to higher values (Figure 10, § 4.5).

(viii) Comparison to the EWs from Steidel et al. (2010), which were calculated using galaxy pairs and probe smaller impact parameters than in this work, yields agreement for the overlapping impact parameter bins (Figure 11, § 4.6).

(ix) The value of the covering fraction, defined as the fraction of galaxies for which the median optical depth within $\pm 170 \text{ km s}^{-1}$ exceeds specific values, was found to be greater than the covering fraction at a random location for galaxy impact parameters below $\sim 180 \text{ pkpc}$, for all ions (Figure 9, § 4.4).

(x) For HI, CIV, and in some cases OVI, the covering fraction is elevated with respect to the IGM for all impact parameters probed, which is consistent with the optical depth enhancement seen along the transverse distance cuts. However, for high optical depth threshold values, corresponding to the top 1% of random regions, the enhancement is only seen at impact parameters $< 0.13 \text{ pMpc}$, which suggests that high optical depth systems are preferentially found at very small galactocentric distances (Figure 9, § 4.4).

(xi) Limiting the sample to galaxies with nebular redshifts does not impart any significant change to the observed median optical depths as a function of transverse and LOS distance from the galaxies, even when the same sample of galaxies is used to compare the measurement techniques. This implies that the elongation of the optical depth enhancement along the LOS direction is due to gas peculiar velocities rather than redshift errors (Figure 12, § 4.7).

Thanks to our unique sample, and particularly due to its unprecedented combination of size and data quality, we were able to study the 2-D metal distribution around galaxies in a way that has not been possible until now. We have presented the first 2-D maps of metal absorption around galaxies and we have quantified the enhancement in the absorption signal near $z \approx 2.4$ star-forming galaxies for 5 different metal ions, as well as for neutral hydrogen. Observations with MOSFIRE have allowed us to significantly reduce the errors on galaxy redshift measurements, to the point where we now have compelling evidence that the redshift-space distortions seen in the 2-D HI and metal ion optical depth distributions (i.e. the Finger-of-God effect seen in the LOS direction) is caused by peculiar motions of the gas.

As MOSFIRE observations proceed and the KBSS galaxy sample continues to grow, improvements in the data will allow us to split the sample according to various galaxy properties (e.g., mass, SFR, etc.) and to study how these characteristics affect the CGM. Additionally, we plan to examine the ratios between different metal ions and between metal ions and HI, and also to compare the results from this work to simulations.

ACKNOWLEDGEMENTS

We are very grateful to Milan Bogosavljevic, Alice Shapley, Dawn Erb, Naveen Reddy, Max Pettini, Ryan Trainor, and David Law for their invaluable contributions to the Keck Baryonic Structure Survey, without which the results presented here would not have been possible. We also thank Ryan Cooke for his help with the continuum fitting of QSO spectra, and the anonymous referee whose valuable comments greatly improved this work. We gratefully acknowledge support from Marie Curie Training Network CosmoComp (PITN-GA-2009-238356) and from the European Research Council under the European Union's Seventh Framework Programme (FP7/2007-2013) / ERC Grant agreement 278594-GasAroundGalaxies. CCS, GCR, ALS acknowledge support from grants AST-0908805 and AST-13131472 from the US National Science Foundation. We thank the W. M. Keck Observatory staff for their assistance with the observations. We also thank the Hawaiian people, as without their hospitality the observations presented here would not have been possible.

REFERENCES

- Adelberger K. L., Shapley A. E., Steidel C. C., Pettini M., Erb D. K., Reddy N. A., 2005a, *ApJ*, 629, 636

- Adelberger K. L., Steidel C. C., Pettini M., Shapley A. E., Reddy N. A., Erb D. K., 2005b, *ApJ*, 619, 697
- Adelberger K. L., Steidel C. C., Shapley A. E., Hunt M. P., Erb D. K., Reddy N. A., Pettini M., 2004, *ApJ*, 607, 226
- Adelberger K. L., Steidel C. C., Shapley A. E., Pettini M., 2003, *ApJ*, 584, 45
- Aguirre A., Hernquist L., Schaye J., Weinberg D. H., Katz N., Gardner J., 2001, *ApJ*, 560, 599
- Aguirre A., Schaye J., Theuns T., 2002, *ApJ*, 576, 1
- Ajiki M., Taniguchi Y., Murayama T., Nagao T., Veilleux S., Shioya Y., Fujita S. S., Kakazu Y., Komiyama Y., Okamura S., Sanders D. B., Oyabu S., Kawara K., Ohyama Y., Iye M., Kashikawa N., Yoshida M., Sasaki T., Kosugi G., Aoki K., Takata T., Saito Y., Kawabata K. S., Sekiguchi K., Okita K., Shimizu Y., Inata M., Ebizuka N., Ozawa T., Yadoumaru Y., Taguchi H., Ando H., Nishimura T., Hayashi M., Ogasawara R., Ichikawa S.-i., 2002, *ApJ*, 576, L25
- Bahcall J. N., Spitzer Jr. L., 1969, *ApJ*, 156, L63
- Bergeron J., Boissé P., 1991, *A&A*, 243, 344
- Booth C. M., Schaye J., Delgado J. D., Dalla Vecchia C., 2012, *MNRAS*, 420, 1053
- Chen H.-W., Lanzetta K. M., Webb J. K., 2001, *ApJ*, 556, 158
- Chen H.-W., Mulchaey J. S., 2009, *ApJ*, 701, 1219
- Conroy C., Shapley A. E., Tinker J. L., Santos M. R., Lemson G., 2008, *ApJ*, 679, 1192
- Cowie L. L., Songaila A., 1998, *Nature*, 394, 44
- Ellison S. L., Songaila A., Schaye J., Pettini M., 2000, *AJ*, 120, 1175
- Erb D. K., Shapley A. E., Pettini M., Steidel C. C., Reddy N. A., Adelberger K. L., 2006a, *ApJ*, 644, 813
- Erb D. K., Steidel C. C., Shapley A. E., Pettini M., Reddy N. A., Adelberger K. L., 2006b, *ApJ*, 647, 128
- , 2006c, *ApJ*, 646, 107
- Ford A. B., Oppenheimer B. D., Davé R., Katz N., Kollmeier J. A., Weinberg D. H., 2013, *MNRAS*, 432, 89
- Franx M., Illingworth G. D., Kelson D. D., van Dokkum P. G., Tran K.-V., 1997, *ApJ*, 486, L75
- Haas M. R., Schaye J., Booth C. M., Dalla Vecchia C., Springel V., Theuns T., Wiersma R. P. C., 2013a, *MNRAS*, 435, 2931
- , 2013b, *MNRAS*, 435, 2955
- Heckman T. M., Armus L., Miley G. K., 1990, *ApJS*, 74, 833
- Heckman T. M., Lehnert M. D., Strickland D. K., Armus L., 2000, *ApJS*, 129, 493
- Jones T., Stark D. P., Ellis R. S., 2012, *ApJ*, 751, 51
- Kaiser N., 1987, *MNRAS*, 227, 1
- Martin C. L., 2005, *ApJ*, 621, 227
- McLean I. S., Steidel C. C., Epps H. W., Konidaris N., Matthews K. Y., Adkins S., Aliado T., Brims G., Canfield J. M., Cromer J. L., Fucik J., Kulas K., Mace G., Magnone K., Rodriguez H., Rudie G., Trainor R., Wang E., Weber B., Weiss J., 2012, in *Society of Photo-Optical Instrumentation Engineers (SPIE) Conference Series*, Vol. 8446, *Society of Photo-Optical Instrumentation Engineers (SPIE) Conference Series*
- Nielsen N. M., Churchill C. W., Kacprzak G. G., Murphy M. T., 2013, *ApJ*, 776, 114
- Oppenheimer B. D., Davé R., 2008, *MNRAS*, 387, 577
- Oppenheimer B. D., Davé R., Kereš D., Fardal M., Katz N., Kollmeier J. A., Weinberg D. H., 2010, *MNRAS*, 406, 2325
- Pettini M., Steidel C. C., Adelberger K. L., Dickinson M., Gialalisco M., 2000, *ApJ*, 528, 96
- Planck Collaboration, Ade P. A. R., Aghanim N., Armitage-Caplan C., Arnaud M., Ashdown M., Atrio-Barandela F., Aumont J., Baccigalupi C., Banday A. J., et al., 2013, *ArXiv e-prints*
- Prochaska J. X., Weiner B., Chen H.-W., Mulchaey J., Cooksey K., 2011, *ApJ*, 740, 91
- Quider A. M., Pettini M., Shapley A. E., Steidel C. C., 2009, *MNRAS*, 398, 1263
- Rakic O., Schaye J., Steidel C. C., Booth C. M., Dalla Vecchia C., Rudie G. C., 2013, *MNRAS*, 433, 3103
- Rakic O., Schaye J., Steidel C. C., Rudie G. C., 2011, *MNRAS*, 414, 3265
- , 2012, *ApJ*, 751, 94
- Reddy N. A., Steidel C. C., Pettini M., Adelberger K. L., Shapley A. E., Erb D. K., Dickinson M., 2008, *ApJS*, 175, 48
- Rudie G. C., Steidel C. C., Trainor R. F., Rakic O., Bogosavljević M., Pettini M., Reddy N., Shapley A. E., Erb D. K., Law D. R., 2012, *ApJ*, 750, 67
- Rupke D. S., Veilleux S., Sanders D. B., 2005, *ApJS*, 160, 115
- Savage B. D., Sembach K. R., 1991, *ApJ*, 379, 245
- Schaye J., Aguirre A., Kim T.-S., Theuns T., Rauch M., Sargent W. L. W., 2003, *ApJ*, 596, 768
- Schaye J., Rauch M., Sargent W. L. W., Kim T.-S., 2000, *ApJ*, 541, L1
- Shapley A. E., Steidel C. C., Pettini M., Adelberger K. L., 2003, *ApJ*, 588, 65
- Shen S., Madau P., Guedes J., Mayer L., Prochaska J. X., Wadsley J., 2013, *ApJ*, 765, 89
- Simcoe R. A., 2011, *ApJ*, 738, 159
- Songaila A., 1998, *AJ*, 115, 2184
- Steidel C. C., Adelberger K. L., Gialalisco M., Dickinson M., Pettini M., 1999, *ApJ*, 519, 1
- Steidel C. C., Adelberger K. L., Shapley A. E., Pettini M., Dickinson M., Gialalisco M., 2003, *ApJ*, 592, 728
- Steidel C. C., Erb D. K., Shapley A. E., Pettini M., Reddy N., Bogosavljević M., Rudie G. C., Rakic O., 2010, *ApJ*, 717, 289
- Steidel C. C., Gialalisco M., Pettini M., Dickinson M., Adelberger K. L., 1996, *ApJ*, 462, L17
- Steidel C. C., Rudie G. C., Strom A. L., Pettini M., Reddy N. A., Shapley A. E., Trainor R. F., Erb D. K., Turner M. L., Konidaris N. P., Kulas K. R., Mace G., Matthews K., McLean I. S., 2014, *ArXiv e-prints*
- Steidel C. C., Shapley A. E., Pettini M., Adelberger K. L., Erb D. K., Reddy N. A., Hunt M. P., 2004, *ApJ*, 604, 534
- Stocke J. T., Penton S. V., Danforth C. W., Shull J. M., Tumlinson J., McLin K. M., 2006, *ApJ*, 641, 217
- Trainor R. F., Steidel C. C., 2012, *ApJ*, 752, 39
- Tremonti C. A., Moustakas J., Diamond-Stanic A. M.,

2007, ApJ, 663, L77

Tumlinson J., Thom C., Werk J. K., Prochaska J. X., Tripp T. M., Weinberg D. H., Peebles M. S., O’Meara J. M., Oppenheimer B. D., Meiring J. D., Katz N. S., Davé R., Ford A. B., Sembach K. R., 2011, *Science*, 334, 948

Tummuangpak P., Shanks T., Bielby R., Crighton N. H. M., Francke H., Infante L., Theuns T., 2013, ArXiv e-prints

Weiner B. J., Coil A. L., Prochaska J. X., Newman J. A., Cooper M. C., Bundy K., Conselice C. J., Dutton A. A., Faber S. M., Koo D. C., Lotz J. M., Rieke G. H., Rubin K. H. R., 2009, ApJ, 692, 187

Wiersma R. P. C., Schaye J., Dalla Vecchia C., Booth C. M., Theuns T., Aguirre A., 2010, MNRAS, 409, 132

Wiersma R. P. C., Schaye J., Theuns T., 2011, MNRAS, 415, 353

Zhu G., Ménard B., Bizyaev D., Brewington H., Ebelke G., Ho S., Kinemuchi K., Malanushenko V., Malanushenko E., Marchante M., More S., Oravetz D., Pan K., Petitjean P., Simmons A., 2014, MNRAS

Zibetti S., Ménard B., Nestor D., Turnshek D., 2005, ApJ, 631, L105

APPENDIX A: THE PIXEL OPTICAL DEPTH METHOD

In this appendix, we describe our implementation of the pixel optical depth technique. Our version is based on Aguirre et al. (2002), which was itself based on Cowie & Songaila (1998); Ellison et al. (2000); Schaye et al. (2000), and we will point out where our method differs from that of Aguirre et al. (2002).

Using the redshift ranges given in § 3, we calculate the optical depth for each species Z and each multiplet component k (if applicable) as:

$$\tau_{Z,k}(z) \equiv -\ln[F_{Z,k}(z)] \quad (\text{A1})$$

where $F_{Z,k}(z)$ is the normalised flux at redshift z , obtained from

$$F_{Z,k}(z) \equiv F(\lambda = \lambda_{Z,k}[1+z]) \quad (\text{A2})$$

where $\lambda_{Z,k}$ is the transition’s rest wavelength. For all optical depths other than $\tau_{\text{HI},\text{Ly}\alpha}(z)$, linear interpolation of the flux is used so that all discrete z values are the same as for $\tau_{\text{HI},\text{Ly}\alpha}(z)$. Before beginning the correction, we search for saturated pixels, defined as those pixels satisfying $F(\lambda) \leq N_\sigma \sigma(\lambda)$, where $\sigma(\lambda)$ is the normalised noise array, and we set $N_\sigma = 3$. Since the optical depths of the saturated pixels are not reliable, but will be high compared to the unsaturated pixels, we set their values to $\tau_{Z,k}(z) = 10^6$. Using such an extreme optical depth to flag the saturated pixels will not skew our results provided median statistics are used throughout the analysis.

First we perform the recovery for HI, since we will need the recovered optical depths to correct metals which are contaminated by higher order Lyman lines. For HI, the main source of error comes from the saturation of the Ly α lines. Therefore, for all Ly α pixels previously flagged as saturated,

we look to all available higher order Lyman lines (in practice we have used $N = 16$ higher order components). We only use higher order pixels which satisfy $N_\sigma \sigma(\lambda) \leq F(\lambda) \leq 1 - N_\sigma \sigma(\lambda)$ at $\lambda = \lambda_{\text{HI},\text{Ly}n}[1+z]$, to ensure that they are not poorly detected. Scaling the higher order optical depths to the Ly α component strength, we set the recovered Ly α optical depth, $\tau_{\text{HI},\text{Ly}\alpha}^{\text{rec}}(z)$ to be the minimum of all well-detected higher order pixels:

$$\tau_{\text{HI},\text{Ly}\alpha}^{\text{rec}}(z) \equiv \min \left[\frac{\tau_{\text{HI},\text{Ly}n}(z) g_{\text{HI},\text{Ly}\alpha}}{g_{\text{HI},\text{Ly}n}} \right]. \quad (\text{A3})$$

Here, $g_{\text{HI},\text{Ly}n} \equiv f_{\text{HI},\text{Ly}n} \lambda_{\text{HI},\text{Ly}n}$ where $f_{\text{HI},\text{Ly}n}$ is the oscillator strength.

In addition to the above correction for saturated pixels which is identical to the one used in Ellison et al. (2000) and Aguirre et al. (2002), we implement a procedure to search for and flag contaminated Ly α pixels. We consider a Ly α pixel to be contaminated if

$$F_{\text{HI},\text{Ly}\alpha}(z) - N_\sigma \sigma(\lambda = \lambda_{\text{HI},\text{Ly}\alpha}[1+z]) > \max [F_{\text{HI},\text{Ly}\alpha}(z), N_\sigma \sigma(\lambda_{\text{HI},\text{Ly}\alpha}[1+z])]^{g_{\text{HI},\text{Ly}n}/g_{\text{HI},\text{Ly}\alpha}}. \quad (\text{A4})$$

Specifically, for unsaturated Ly α pixels, we scale the Ly α flux to obtain the flux expected at higher-order transition n ; if the observed flux at transition n is significantly greater than would be expected from the Ly α flux, the Ly α pixel is likely contaminated. In order to apply this algorithm to saturated Ly α pixels (for which the flux estimate is likely to be unreliable), we instead use the Ly α noise array to set the Ly α flux. All Ly α pixels found to be contaminated in this way are flagged and discarded for the remainder of the analysis.

The recovered HI Ly α optical depths are then used to correct unsaturated pixels of metals contaminated by Lyman series lines. For the recovery of OVI and CIII, which are located in the Ly β forest, the procedure involves the subtraction of the Lyman lines starting with Ly β (i.e., $n = 2$):

$$\tau_{Z,k}(z) := \tau_{Z,k}(z) - \sum_{n=2}^N \frac{g_{\text{HI},\text{Ly}n}}{g_{\text{HI},\text{Ly}\alpha}} \tau_{\text{HI},\text{Ly}\alpha}^{\text{rec}} \left(\frac{\lambda \lambda_{\text{HI},\text{Ly}\alpha}}{\lambda_{\text{HI},\text{Ly}n}} \right) \quad (\text{A5})$$

where $\lambda = \lambda_{Z,k}[1+z]$ and we take $N = 5$ (the effects of varying N are explored in Appendix B2). For OVI, the HI optical depth subtraction procedure is performed for both multiplet components k .

Something else that we have implemented in the HI subtraction procedure which was not done in Aguirre et al. (2002), is the treatment of saturated metal pixels. More specifically, since the true optical depth of saturated pixels cannot be measured accurately in the presence of noise, we cannot make a reliable HI subtraction. Hence, we do not apply Equation A5 to pixels for which $F(\lambda) \leq N_\sigma \sigma(\lambda)$. Rather, if the sum of contaminating HI optical depths is sufficient to saturate the absorption, i.e. if

$$\exp \left[- \sum_{n=2}^N \frac{g_{\text{HI},\text{Ly}n}}{g_{\text{HI},\text{Ly}\alpha}} \tau_{\text{HI},\text{Ly}\alpha}^{\text{rec}} \left(\frac{\lambda \lambda_{\text{HI},\text{Ly}\alpha}}{\lambda_{\text{HI},\text{Ly}n}} \right) \right] < N_\sigma \sigma(\lambda), \quad (\text{A6})$$

then the pixel cannot be used to estimate the metal optical depth. For CIII, this pixel is discarded immediately. Since OVI is a doublet and we are able to compare the two

components in the next contamination correction step, it is not as crucial to discard all contaminated pixels right away. Instead, we perform this flagging procedure on each of the doublet components and only discard those redshifts for which both components are contaminated.

As mentioned above, the next step is to correct the optical depths of metals which have two multiplet components k (OVI, NV, and SiIV) by taking the minimum of the optical depths, where the optical depth of the weaker component is scaled to match that of the stronger one. Specifically, we take:

$$\tau_{Z,1}^{\text{rec}}(z) = \min \left[\tau_{Z,1}(z), \frac{g_{Z,1}}{g_{Z,2}} \tau_{Z,2}(z) \right]. \quad (\text{A7})$$

However, it may not be a good idea to use the minimum optical depth at every pixel. This is because, particularly in the case where both pixels are not contaminated, doing so will result in an optical depth value that is biased low. To combat this, Aguirre et al. (2002) would only take the optical depth of the weaker component if it were positive, i.e. $\tau_{Z,2}(z) > 0$. Here we use a different approach, where we take the noise level into account, and only use the optical depth of the weaker component if:

$$\left[\exp[-\tau_{Z,2}(z)] - N_{\sigma} \sigma(\lambda = \lambda_{Z,2}[1+z]) \right]^{\frac{g_{Z,1}}{g_{Z,2}}} > \exp[-\tau_{Z,1}(z)] + N_{\sigma} \sigma(\lambda = \lambda_{Z,1}[1+z]). \quad (\text{A8})$$

The left hand side of this condition contains the optical depth of the weaker component expressed in terms of flux, with the noise term subtracted, and then scaled to match the strength of the stronger component optical depth, which is on the right-hand side. This condition states that the scaled optical depth of the weaker component must be *significantly* lower than that of the stronger one in order that it be used for the recovered optical depth value.

Finally, the rest wavelength of CIV puts the recovery region redwards of the Ly α forest, and the majority of the contamination therefore consists of self-contamination from its own doublet. We correct for this self-contamination as follows Aguirre et al. (2002). First, every pixel is checked for contamination from other ions, which is done by testing to see if its optical depth is higher than what would be expected from self-contamination alone. Specifically, we define $\tau_{\text{CIV},1}(\lambda)$ as $\tau_{\text{CIV},1}(z)$ where $z = \lambda/\lambda_{\text{CIV},1} - 1$. If the optical depth at wavelength λ comes from the weaker component, we want to know the optical depth at the location of the strong component $\lambda_s = [\lambda_{\text{CIV},1}/\lambda_{\text{CIV},2}]\lambda$. We also want to consider the case where the optical depth at λ comes from the strong component, and therefore need the optical depth at the wavelength of the weak component, $\lambda_w = \lambda_{\text{CIV},2}[1+z]$. We then scale these optical depths to test if the optical depth at λ is higher than expected from self-contamination, which gives the condition:

$$\exp[-\tau_{\text{CIV},1}(\lambda)] + N_{\sigma} \bar{\sigma}(\lambda) < \exp \left[-\frac{g_{\text{CIV},2}}{g_{\text{CIV},1}} \tau_{\text{CIV},1}(\lambda_s) - \frac{g_{\text{CIV},1}}{g_{\text{CIV},2}} \tau_{\text{CIV},1}(\lambda_w) \right] \quad (\text{A9})$$

where $\bar{\sigma}^2(\lambda) = \sigma^2(\lambda) + \sigma^2(\lambda_s) + \sigma^2(\lambda_w)$; pixels meeting this condition are probably contaminated with absorption from

other ions, and are therefore not used for the correction or any subsequent analysis. Then, an iterative doublet subtraction algorithm is used to remove self-contamination, where the scaled optical depth of the strong component at λ_s is subtracted from the optical depth at λ . Before doing this, for those pixels with $\tau_{\text{CIV},1}(z) < 0$, we set $\tau_{\text{CIV},1}(z) = 10^{-4}$ so that negative optical depth values won't affect the subtraction procedure. After first setting $\tau_{\text{CIV},1}^{\text{rec}}(\lambda) = \tau_{\text{CIV},1}(\lambda)$, the following is repeated until convergence occurs (about 5 iterations):

$$\tau_{\text{CIV},1}^{\text{rec}}(\lambda) := \tau_{\text{CIV},1}(\lambda) - \frac{g_{\text{CIV},2}}{g_{\text{CIV},1}} \tau_{\text{CIV},1}^{\text{rec}}(\lambda_s). \quad (\text{A10})$$

Here we note the implementation of an automated continuum fitting procedure which we apply to the spectral regions with wavelengths greater than that of their quasar's Ly α emission. The purpose of this is to homogenise the continuum fitting errors, and it is performed as follows. This region of each spectrum is divided into bins of size $\Delta\lambda$ in the rest-frame, each with central wavelength λ_i and median flux \bar{f}_i . We then interpolate a B-spline through \bar{f}_k and discard any pixels with flux values that are $N_{\sigma}^{cf} \times \sigma$ below the interpolated flux values. \bar{f}_k is recalculated without the discarded pixels, and the procedure is repeated until convergence is reached. In our implementation, we use $N_{\sigma}^{cf} = 2$ and $\Delta\lambda = 20 \text{ \AA}$ as in Schaye et al. (2003).

Finally, we discuss our masking procedure. As mentioned in § 2, six of the QSOs have DLAs located in their Ly α forest regions. For the recovery of HI and NV, we use the spectra that have had the damping wings of these DLAs fitted out and the saturated region masked. However, for the recovery of OVI and CIII, we want to subtract as much HI contamination as possible. Therefore, we also perform an HI recovery without the Ly α forest region DLAs fitted out and masked, and use these values for the subtraction of contamination from the OVI and CIII regions. We found that the results for OVI and CIII obtained from using the unmasked DLA HI recovery are similar to those obtained from masking out the higher order components of the DLA by hand. Lastly, for all recoveries we have masked out two more DLAs which are bluewards of their QSO's Ly α forest region, i.e. saturated Lyman continuum absorption associated with strong HI absorbers, and we have also masked out all Lyman break regions, which occurs for three of our QSOs.

APPENDIX B: VARIATION IN PIXEL OPTICAL DEPTH RECOVERY

In this section we explore the sensitivity of our results to variations in the method used to recover the pixel optical depths. For this purpose we will compare the enhancement in the median optical depth relative to a random location as a function of 3-D Hubble distance. Note that corrections may change the median $\tau_{Z,\text{rnd}}$ even if they do not change the median $\tau_Z/\tau_{Z,\text{rnd}}$ plotted in this section. As we will demonstrate, our results are not particularly sensitive to any of the corrections that we apply in the recovery of pixel optical depths.

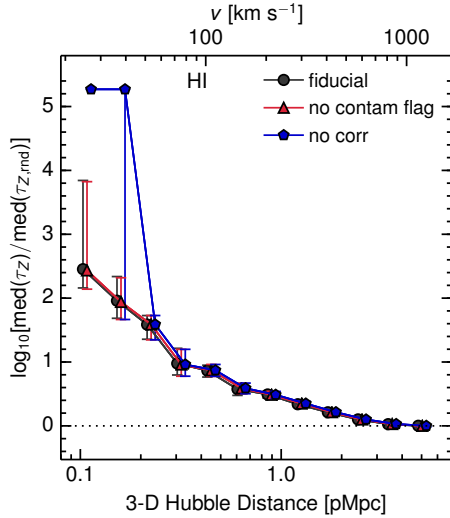


Figure B1. Similar to Figure 8, but only for HI, dividing by $\tau_{Z,\text{rand}}$, and modifying the optical depth recovery method. The modifications are: not flagging pixels determined to be contaminated from their higher-order HI flux (“no contam flag”), and doing no correction at all (i.e. not using higher-order HI lines to correct saturated HI Ly α pixels, “no corr”). The points are offset horizontally by 0.02 dex for clarity.

B1 HI

We begin by examining one of the changes made to the HI Ly α recovery algorithm with respect to that used in Aguirre et al. (2002), which is the use of higher-order HI flux to flag contaminated HI Ly α pixels. We show the resulting median optical depth divided by $\tau_{Z,\text{rand}}$ as a function of Hubble distance in Figure B1 for the fiducial HI recovery as well as one performed without flagging contaminated pixels, and we can see that this change in the algorithm has almost no impact on the results. We have also plotted the median optical depths obtained when no HI correction is done (i.e. saturated HI Ly α pixels are not corrected using higher-order HI components). This correction is most important for small galactocentric distances, where the median optical depths actually reach the optical depth value used to flag saturated pixels. However, the absence of this correction would not affect our overall conclusions.

B2 OVI

For OVI, we first vary the number of higher order HI Lyman lines that are subtracted from the OVI region. The fiducial number that we use is five, and we have also tried subtracting ten, two, and zero higher order HI lines, the outcomes of which are shown in Figure B2. In the recoveries where at least two higher-order HI lines are subtracted, the curves are almost identical. The main difference (which cannot be seen from this figure) is that the median optical depth in random locations ($\tau_{Z,\text{rand}}$) increases as fewer HI lines are subtracted.

Next we investigate the effects of the pixel optical depth recovery modifications with respect to Aguirre et al. (2002).

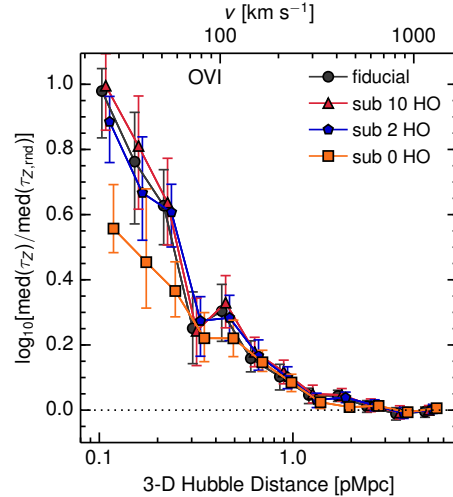


Figure B2. Similar to Figure B1, but for OVI, and modifying the optical depth recovery method with respect to the fiducial one (which invokes the subtraction of five higher order HI lines). The modifications are: subtracting 10, 2, and 0 higher-order (HO) HI lines, where the doublet minimum is taken in every case.

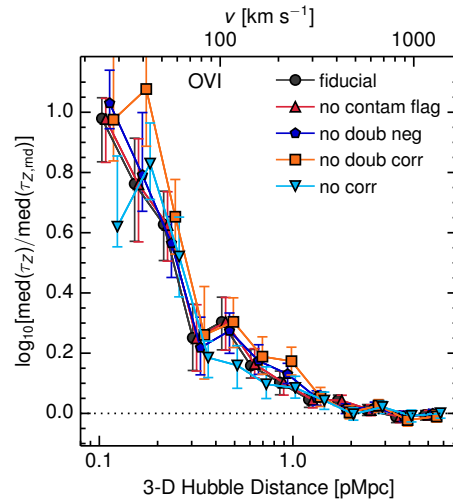


Figure B3. Similar to Figure B1, but for the following modifications with respect to the fiducial optical depth recovery: pixels determined to be saturated with contaminating HI are not flagged (“no contam flag”); the weaker doublet component is not considered if it has a negative optical depth (“no doub neg”); no doublet minimum taken (“no doub corr”); and no correction at all (i.e., neither HI subtraction nor doublet minimum, “no corr”).

Specifically, in Figure B3, we show the median optical depth that results from not discarding pixels for which the contaminating HI absorption is thought to be saturated based on the sum of corresponding higher-order HI optical depths; and also using the doublet minimum condition from Aguirre et al. (2002): that is, instead of using Equation A8, the doublet minimum is taken for every pixel, except for pixels where the weaker component has a negative optical depth.

Neither of these changes has any impact on the resulting median optical depth. In Figure B3, we also look at the median optical depth from recoveries where we did not perform the doublet correction (that is, we still subtract five higher order HI lines, but then do not take the minimum of the OVI doublet at each redshift); finally where we did not perform any correction at all. Although not taking the doublet minimum does not have a significant affect on the outcome, not performing any correction at all does reduce the dynamic range with respect to the fiducial case.

Another technique which can be applied to the OVI recovery is to make redshift cuts such that those wavelength ranges contaminated by more higher order HI lines are removed from the analysis. For example, one can choose to limit the recovery to the region in the spectrum where only three HI lines ($\text{Ly}\alpha$, $\text{Ly}\beta$, $\text{Ly}\gamma$, and no further higher order lines) are present. In the top row Figure B4 we show the result of limiting the spectral region to that contaminated by all, seven, and five higher order HI lines, respectively. For the five higher order HI line limit, there are so few galaxies in the innermost impact parameter bins (right panel of Figure B4 that the error bars are likely not reliable. In general, we find these cuts slightly increase the dynamic range of the optical depths, but for up to 3 higher order lines, i.e. our most restrictive cut, the dynamic range in τ_{OVI} is significantly smaller. Given the low number of galaxies at the smallest impact parameters where the optical depth is enhanced with respect to the median (and the even lower numbers resulting from reducing the sample size), such differences are probably due to small number statistics.

Additionally, one could optimise the OVI recovery by making cuts in the S/N of the HIRES spectra, since it is at the lowest wavelengths of Keck (those of the OVI region) where the S/N declines quite rapidly. We try excluding individual regions with S/N less than 10 and 20 (using a higher S/N cut results in < 10 galaxies in the smallest impact parameter bin), and show the results in the top row of Figure B5. Indeed, such cuts do appear to enhance the median central absorption relative to that in a random location. However, as was the case for the higher order HI line cuts, this could certainly be due to the varying and small number of galaxies in the smallest impact parameter bins (see the histograms in the bottom row of Figure B5).

B3 Nv

The optical depth correction for Nv consists only of examining both doublet components at each redshift and taking the minimum of the two optical depths. In Figure B6, we compare the 3-D-Hubble distance curves determined both with and without this correction, as well the curve resulting from using the doublet minimum condition from Aguirre et al. (2002) (where instead of using Equation A8, the doublet minimum is taken for all pixels except those where the weaker component has a negative optical depth). Neither of these changes have a significant impact on the resulting median optical depth. Not using the doublet correction yields a larger dynamic range; however, the errors become much larger. Hence, the significance with which the enhancement

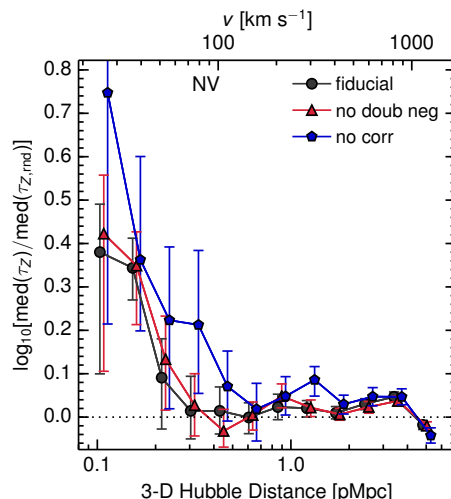


Figure B6. Similar to Figure B1, but for Nv and comparing the use of the fiducial optical depth recovery method (taking the doublet minimum) to recoveries where the weaker doublet component is not considered if it has a negative optical depth (“no doub neg”), and where no correction is done at all (“no corr”).

is detected is typically smaller without the correction. We also note that since the points here are correlated, the fact that the first five green points are above the black ones may not be a significant effect. Indeed, the differences between the two recovery methods is no longer seen when we use cuts along the transverse direction of the 2-D optical depth maps (where the points are independent) instead of the 3-D Hubble distances.

B4 CIV

As described in § 3, we normally perform an automated continuum fit to any regions in the spectrum redwards of the $\text{Ly}\alpha$ emission. However, we find that this only slightly boosts the dynamic range in the recovered median optical depths, as can be seen in Figure B7.

We have also examined the effect of not applying the self-contamination correction, but rather taking the doublet minimum, as well as not doing any correction at all. In both instances, the dynamic range probed is actually larger than in the self-contamination correction case. However, this increase in dynamic range is probably due to self-contamination. The CIV doublet separation is $\sim 500 \text{ km s}^{-1}$. As this is smaller than the scale over which the absorption is enhanced, self-contamination will boost the enhancement in the apparent CIV absorption near galaxies.

Finally, our fiducial CIV recovery only uses pixels within the redshift range of the $\text{Ly}\alpha$ forest of the quasar, i.e. down to the redshift for which $\text{Ly}\alpha$ absorption coincides with the $\text{Ly}\beta$ emission line. However, the region where CIV can be recovered accurately (i.e., redwards of the QSO $\text{Ly}\alpha$ emission) extends to lower redshifts than this range, and so we experiment with performing the recovery down to

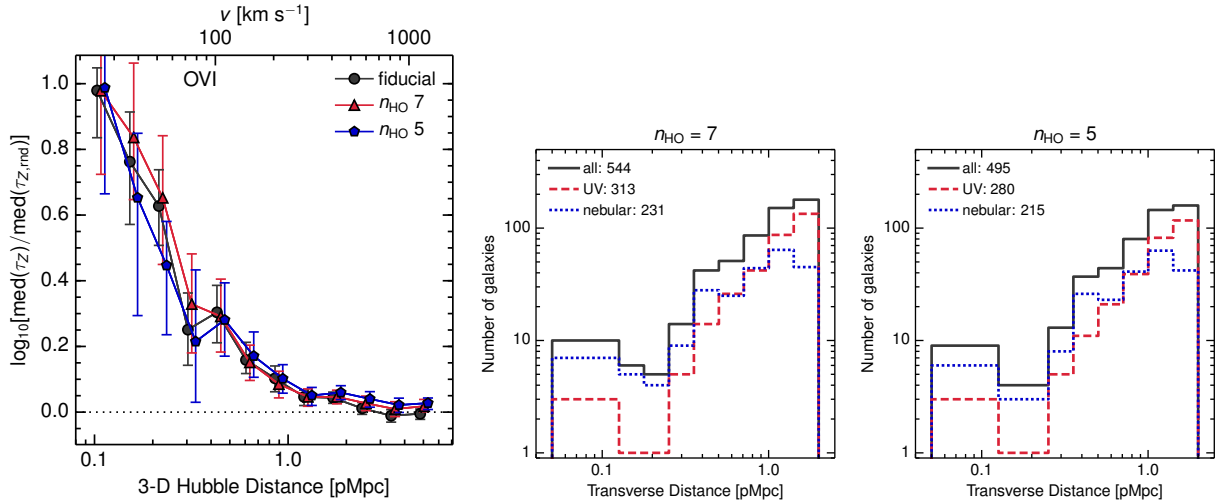


Figure B4. *Left:* Similar to Figure B1, but limiting the spectral region to that contaminated by: any number (fiducial), seven and five higher order H α lines. *Centre and right:* Histograms of the number of galaxies per impact parameter bin for each of the spectral region cuts shown above. For reference, the fiducial number of galaxies in each bin is 854 galaxies in total, with 473 and 381 having their redshifts measured from rest-frame UV features and nebular emission lines, respectively.

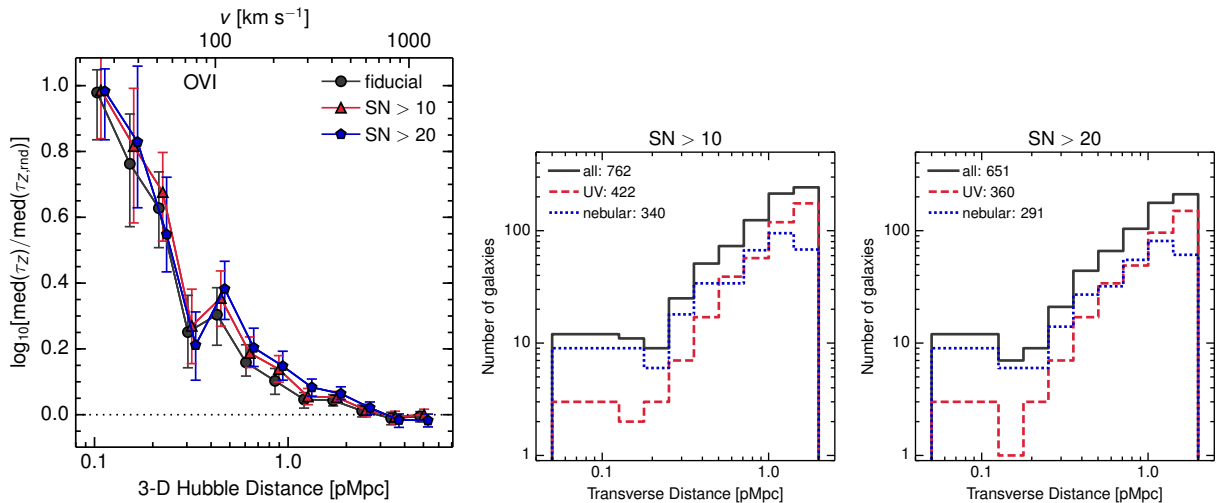


Figure B5. *Right:* Similar to Figure B1, but limiting the used spectral region to that having S/N greater than 0 (fiducial), 10 and 20. *Centre and right:* Histograms of the number of galaxies per impact parameter bin for each of the spectral region S/N cuts shown above. For reference, the fiducial number of galaxies in each bin is 854 galaxies in total, with 473 and 381 having their redshifts measured from rest-frame UV features and nebular emission lines, respectively.

the redshift for which C IV absorption coincides with the quasar’s Ly α emission line.

The result is shown as the red points Figure B7. Extending the recovered redshift range increases the number of galaxies that fall within the spectral coverage range (see the galaxy histograms in the right two panels of Figure B7). However, the signal is slightly reduced, although the difference is not significant. The galaxy sample now contains, and the median redshift is now 2.27 instead of 2.34 for the fiducial sample. This could skew the sample to lower masses, since at lower redshift these galaxies are more easily ob-

served. Alternatively, the small decrease in the enhancement may reflect small number statistics since it is not significant.

B5 C III

Since the correction for C III involves the subtraction of higher-order contaminating H α lines, we repeat the procedure done for OVI where we test the effect of removing different numbers of higher order H α lines (the fiducial number being 5). In Figure B8 we show the result of removing 10, 5, 2, and no higher order lines (no correction). We also show

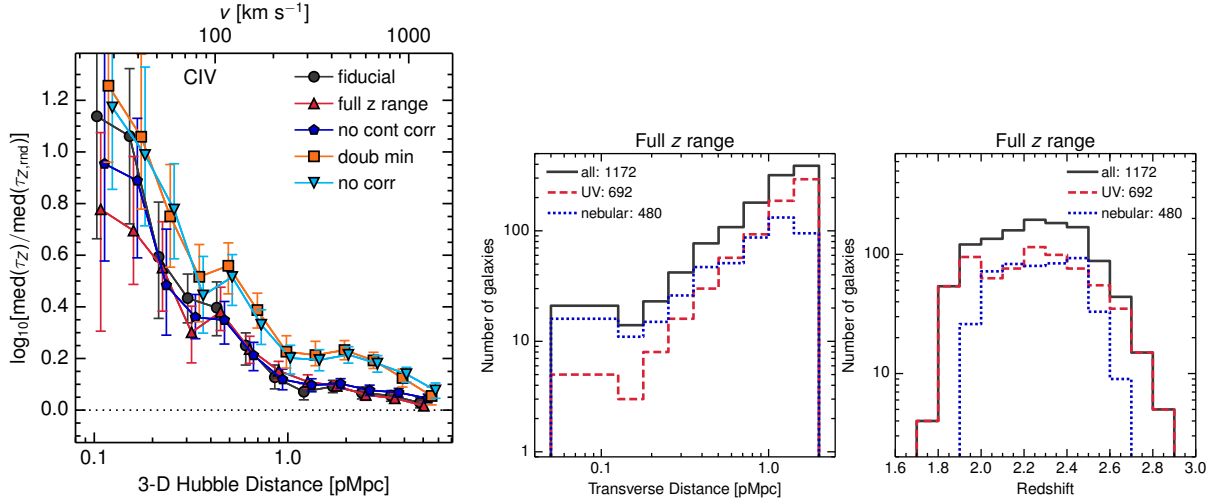


Figure B7. *Left:* Similar to Figure B1, but plotting different CIV recoveries. These are: self-contamination correction (“*fiducial*”); using the full redshift range (“*full z range*”); without the automatic continuum correction (“*no cont corr*”); taking the doublet minimum instead of the self-contamination correction (“*doub min*”); and without any correction (“*no corr*”). *Centre and right:* The histograms show the number of galaxies per impact parameter (centre) and redshift bin (right) obtained when the full CIV redshift range is used. For reference, the fiducial number of galaxies in each bin is 854 galaxies in total, with 473 and 381 having their redshifts measured from rest-frame UV features and nebular emission lines, respectively.

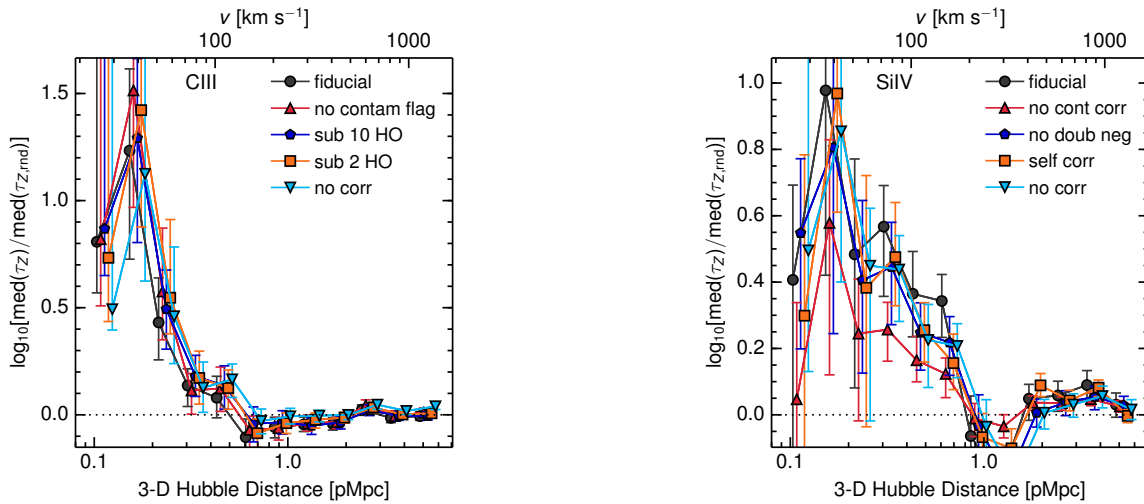


Figure B8. Similar to Figure B1, but for CIII and modifying the optical depth recovery method with respect to the fiducial one (which invokes the subtraction of five higher order H I lines). The modifications are: not flagging pixels determined to be contaminated from their higher-order H I flux (“*no contam flag*”); and subtracting 10 (“*sub 10 HO*”), 2 (“*sub 2 HO*”), and 0 (“*no corr*”) higher-order H I lines.

Figure B9. Similar to Figure B1, but only for SiIV and for different optical depth recovery methods. These are: taking the doublet minimum (“*fiducial*”); without the automatic continuum correction (“*no cont corr*”); the weaker doublet component is not considered if it has a negative optical depth (“*no doub neg*”); performing a self-contamination correction instead of taking the doublet minimum (“*self corr*”); and without any correction (“*no corr*”).

the effect of not flagging pixels determined to be saturated due to H I contamination. We find almost no change except for the case of no correction, where the optical depth dynamic range is slightly reduced.

B6 SiIV

In Figure B9, we find that for SiIV (unlike for CIV) the automated correction to the continuum fit substantially increases the dynamic range probed. Since SiIV is a relatively

weak transition and its optical depths are very close to the noise level, it is likely quite sensitive to the continuum fit.

Using the doublet minimum condition from Aguirre et al. (2002) (where instead of using Equation A8, the doublet minimum is taken for all pixels except those where the weaker component has a negative optical depth), employing the self-contamination correction instead of the doublet minimum, or doing no correction at all does not significantly alter the dynamic range of the recovered optical depths, although we note that using the self-contamination correction results in larger errors. This may be due to the fact that SiIV is a relatively weak line (compared to CIV) and the greatest source of contamination likely comes from CIV rather than from its own doublet.

APPENDIX C: COVERING FRACTION FOR EW THRESHOLDS

Here we investigate the outcome of using an alternate threshold for the covering fraction, where we use the EW (rather than the median optical depth) within $\pm 170 \text{ km s}^{-1}$ of every galaxy, to facilitate comparison with low-quality data. The EW within $\pm 170 \text{ km s}^{-1}$ is also computed for 1000 random regions within the spectra. We define the covering fraction as the fraction of galaxies within an impact parameter bin with an EW above $EW_{Z,\text{thresh}}$, where we take $EW_{Z,\text{thresh}}$ values as those where the covering fractions for random regions are 0.25, 0.05 and 0.01. The results are shown in Figure C1 and Table C1.

In general, the results are similar to those obtained using our first covering fraction definition: for HI, the covering fraction is above that for random regions out to the largest impact parameter in our sample (2 pMpc), while for metals the covering fraction is only elevated for the smallest transverse distance bins. One difference to note is that for the EW thresholds, a signal is seen for the covering fraction of NV (which was not the case using median optical depth thresholds).

APPENDIX D: GALAXY REDSHIFT MEASUREMENTS

Figure 12 investigated if there are any differences in the absorption profiles using the full galaxy sample (which contains galaxy redshifts measured from a mix of rest-frame UV features and nebular emission lines) to a sample of galaxies with redshifts measured only using nebular emission lines. However, the comparison was complicated by the fact that these two samples contain different galaxies (and also that the latter group has less than half as many galaxies as the former).

To remove galaxy sample effects, we now use only the 238 galaxies that have redshifts measured using both techniques, and directly compare the results in Figure D1. The slight enhancement at large LOS distances in the optical depth of the nebular only sample that was visible in Figure 12 for OVI and CIV is less apparent here. Overall there

is only one significant difference between the two samples, for the smallest impact parameter / LOS bin, the nebular-only optical depths are consistently lower than those measured from rest-frame UV features. This may suggest that the peak in the absorption is systematically offset from the galaxy's systemic redshift.

Furthermore, our galaxy sample has changed significantly from that of Rakic et al. (2012). Particularly in the innermost impact parameter bins, many more galaxies now have redshifts measured using MOSFIRE. This presents a problem: since the redshift errors in Rakic et al. (2012) were so large, then would we not expect to see a difference in the LOS extent of HI optical depths between the two samples? Specifically, the results from Rakic et al. (2012) should essentially show the effect of being smoothed on 150 km s^{-1} scales with respect to the current data.

To explore this, we show our median HI optical depth results (yellow circles) alongside those from Rakic et al. (2012, grey points) in Figure D2. Specifically, we plot the unsmoothed data taken from cuts along the LOS through the HI map in our Figure 4 and Figure 5 of Rakic et al. (2012). We also show how the current data look when smoothed with a $\sigma = 150 \text{ km s}^{-1}$ Gaussian as the magenta line. Naively, we would expect the points from Rakic et al. (2012) to be consistent with this curve, and indeed, except for the smallest transverse cut (upper left panel), they are in relatively good agreement.

As for the innermost transverse distance bin, it is still curious that HI optical depths from this work and Rakic et al. (2012) are in near perfect agreement. A possible explanation comes from the fact that galaxies with low impact parameters were preferentially targeted with NIRSPEC – already in Rakic et al. (2012), 25% of galaxies with impact parameters less than 250 kpc had nebular redshifts (compared to 9% for the remainder of the sample), reducing the amount of change we would expect to see between this study and the previous one.

It is worth mentioning that the latest data resolve some tensions with theory. Figure 7 of Rakic et al. (2013) demonstrates that the observed LOS optical depth values tend to be lower than those seen in simulations for impact parameters 0.013–0.25 pMpc, which is no longer the case with the updated KBSS galaxy sample.

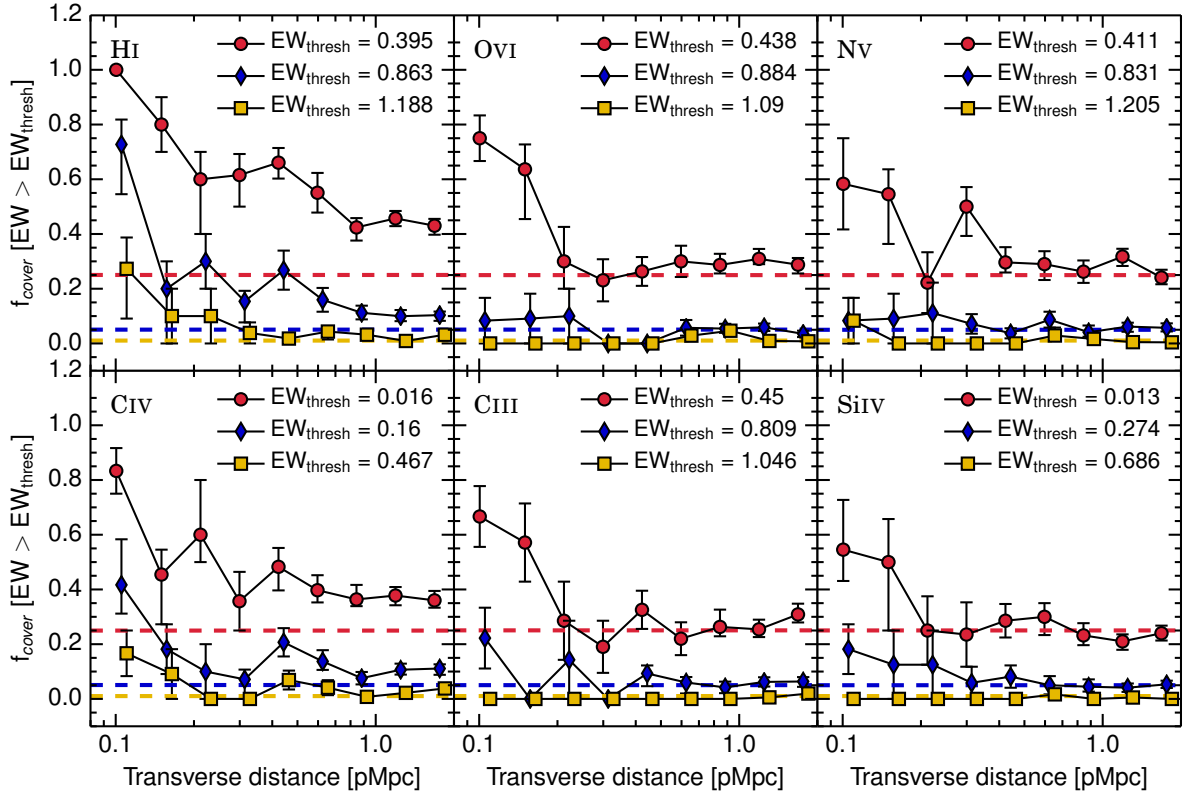


Figure C1. Covering fraction for each ion, defined as the fraction of galaxies within some impact parameter bin (plotted along the y-axis) that have an EW, calculated by integrating the flux decrement over $\pm 170 \text{ km s}^{-1}$, above some threshold value (in Å). These threshold values are set by some multiple of the median EW for 1000 randomly drawn regions integrated over $\pm 170 \text{ km s}^{-1}$. These regions are then used to determine the covering fraction of the $EW_{Z, \text{thresh}}$ values, which are denoted by the dotted horizontal lines. Points determined using different $\tau_{Z, \text{thresh}}$ values have been offset horizontally by 0.2 dex for clarity.

Table C1. Covering fraction and $1\text{-}\sigma$ errors as a function of transverse distance (top row), which is defined as the fraction of galaxies in each impact parameter bin that have an EW within $\pm 170 \text{ km s}^{-1}$ above some threshold value. The threshold values are set by the EWs at which the covering fraction of 1000 random $\pm 170 \text{ km s}^{-1}$ regions, f_{IGM} , are equal to 0.25, 0.05, and 0.01 (second column), and the results are plotted in Figure C1.

| D_{trans} (pMpc) | | 0.04–0.13 | 0.13–0.18 | 0.18–0.25 | 0.25–0.36 | 0.36–0.50 | 0.50–0.71 | 0.71–1.00 | 1.00–1.42 | 1.42–2.00 |
|---------------------------|------------------|------------------------|------------------------|------------------------|------------------------|------------------------|------------------------|------------------------|------------------------|------------------------|
| Ion | f_{IGM} | | | | | | | | | |
| HI | 0.25 | $1.00^{+0.00}_{-0.00}$ | $0.80^{+0.10}_{-0.10}$ | $0.60^{+0.10}_{-0.20}$ | $0.62^{+0.08}_{-0.12}$ | $0.66^{+0.05}_{-0.06}$ | $0.55^{+0.07}_{-0.07}$ | $0.42^{+0.03}_{-0.05}$ | $0.46^{+0.03}_{-0.03}$ | $0.43^{+0.02}_{-0.03}$ |
| | 0.05 | $0.73^{+0.09}_{-0.18}$ | $0.20^{+0.10}_{-0.20}$ | $0.30^{+0.10}_{-0.10}$ | $0.15^{+0.04}_{-0.08}$ | $0.27^{+0.07}_{-0.07}$ | $0.16^{+0.04}_{-0.04}$ | $0.11^{+0.03}_{-0.02}$ | $0.10^{+0.02}_{-0.02}$ | $0.10^{+0.01}_{-0.02}$ |
| | 0.01 | $0.27^{+0.11}_{-0.18}$ | $0.10^{+0.10}_{-0.10}$ | $0.10^{+0.10}_{-0.10}$ | $0.04^{+0.04}_{-0.04}$ | $0.02^{+0.02}_{-0.02}$ | $0.04^{+0.01}_{-0.03}$ | $0.03^{+0.02}_{-0.02}$ | $0.01^{+0.01}_{-0.00}$ | $0.03^{+0.01}_{-0.01}$ |
| OVI | 0.25 | $0.75^{+0.08}_{-0.08}$ | $0.64^{+0.09}_{-0.18}$ | $0.30^{+0.13}_{-0.10}$ | $0.23^{+0.08}_{-0.08}$ | $0.26^{+0.05}_{-0.05}$ | $0.30^{+0.06}_{-0.06}$ | $0.29^{+0.04}_{-0.03}$ | $0.31^{+0.04}_{-0.02}$ | $0.29^{+0.02}_{-0.03}$ |
| | 0.05 | $0.08^{+0.08}_{-0.08}$ | $0.09^{+0.09}_{-0.09}$ | $0.10^{+0.10}_{-0.10}$ | $0.00^{+0.00}_{-0.00}$ | $0.00^{+0.00}_{-0.00}$ | $0.06^{+0.03}_{-0.03}$ | $0.05^{+0.02}_{-0.02}$ | $0.06^{+0.01}_{-0.01}$ | $0.04^{+0.01}_{-0.01}$ |
| | 0.01 | $0.00^{+0.00}_{-0.00}$ | $0.00^{+0.00}_{-0.00}$ | $0.00^{+0.00}_{-0.00}$ | $0.00^{+0.00}_{-0.00}$ | $0.00^{+0.00}_{-0.00}$ | $0.03^{+0.01}_{-0.01}$ | $0.05^{+0.02}_{-0.02}$ | $0.01^{+0.00}_{-0.00}$ | $0.01^{+0.00}_{-0.00}$ |
| NV | 0.25 | $0.58^{+0.17}_{-0.17}$ | $0.55^{+0.09}_{-0.18}$ | $0.22^{+0.11}_{-0.11}$ | $0.50^{+0.07}_{-0.11}$ | $0.30^{+0.06}_{-0.04}$ | $0.29^{+0.05}_{-0.06}$ | $0.26^{+0.04}_{-0.04}$ | $0.32^{+0.03}_{-0.03}$ | $0.24^{+0.03}_{-0.02}$ |
| | 0.05 | $0.08^{+0.08}_{-0.08}$ | $0.09^{+0.09}_{-0.09}$ | $0.11^{+0.11}_{-0.11}$ | $0.07^{+0.04}_{-0.04}$ | $0.04^{+0.02}_{-0.02}$ | $0.09^{+0.03}_{-0.03}$ | $0.04^{+0.02}_{-0.02}$ | $0.06^{+0.01}_{-0.01}$ | $0.06^{+0.02}_{-0.01}$ |
| | 0.01 | $0.08^{+0.08}_{-0.08}$ | $0.00^{+0.00}_{-0.00}$ | $0.00^{+0.00}_{-0.00}$ | $0.00^{+0.00}_{-0.00}$ | $0.00^{+0.00}_{-0.00}$ | $0.03^{+0.03}_{-0.01}$ | $0.02^{+0.01}_{-0.02}$ | $0.00^{+0.00}_{-0.00}$ | $0.00^{+0.00}_{-0.00}$ |
| CIV | 0.25 | $0.83^{+0.08}_{-0.08}$ | $0.45^{+0.09}_{-0.18}$ | $0.60^{+0.20}_{-0.10}$ | $0.36^{+0.11}_{-0.11}$ | $0.48^{+0.07}_{-0.09}$ | $0.40^{+0.05}_{-0.04}$ | $0.36^{+0.05}_{-0.02}$ | $0.38^{+0.03}_{-0.04}$ | $0.36^{+0.03}_{-0.03}$ |
| | 0.05 | $0.42^{+0.17}_{-0.10}$ | $0.18^{+0.09}_{-0.09}$ | $0.10^{+0.10}_{-0.10}$ | $0.07^{+0.04}_{-0.07}$ | $0.21^{+0.05}_{-0.05}$ | $0.14^{+0.04}_{-0.03}$ | $0.08^{+0.02}_{-0.02}$ | $0.11^{+0.02}_{-0.02}$ | $0.11^{+0.02}_{-0.02}$ |
| | 0.01 | $0.17^{+0.08}_{-0.08}$ | $0.09^{+0.09}_{-0.09}$ | $0.00^{+0.00}_{-0.00}$ | $0.00^{+0.00}_{-0.00}$ | $0.07^{+0.03}_{-0.03}$ | $0.04^{+0.03}_{-0.03}$ | $0.01^{+0.01}_{-0.01}$ | $0.02^{+0.01}_{-0.01}$ | $0.04^{+0.01}_{-0.01}$ |
| CIII | 0.25 | $0.67^{+0.11}_{-0.11}$ | $0.57^{+0.14}_{-0.14}$ | $0.29^{+0.14}_{-0.14}$ | $0.19^{+0.10}_{-0.10}$ | $0.33^{+0.07}_{-0.07}$ | $0.22^{+0.06}_{-0.06}$ | $0.26^{+0.06}_{-0.03}$ | $0.25^{+0.04}_{-0.03}$ | $0.31^{+0.04}_{-0.03}$ |
| | 0.05 | $0.22^{+0.11}_{-0.11}$ | $0.00^{+0.00}_{-0.00}$ | $0.14^{+0.14}_{-0.14}$ | $0.00^{+0.00}_{-0.00}$ | $0.09^{+0.03}_{-0.05}$ | $0.06^{+0.02}_{-0.04}$ | $0.04^{+0.02}_{-0.02}$ | $0.06^{+0.02}_{-0.02}$ | $0.06^{+0.02}_{-0.02}$ |
| | 0.01 | $0.00^{+0.00}_{-0.00}$ | $0.00^{+0.00}_{-0.00}$ | $0.00^{+0.00}_{-0.00}$ | $0.00^{+0.00}_{-0.00}$ | $0.00^{+0.00}_{-0.00}$ | $0.00^{+0.00}_{-0.00}$ | $0.00^{+0.00}_{-0.00}$ | $0.01^{+0.01}_{-0.01}$ | $0.02^{+0.01}_{-0.01}$ |
| SiIV | 0.25 | $0.55^{+0.18}_{-0.11}$ | $0.50^{+0.16}_{-0.25}$ | $0.25^{+0.12}_{-0.12}$ | $0.24^{+0.12}_{-0.12}$ | $0.29^{+0.06}_{-0.06}$ | $0.30^{+0.05}_{-0.07}$ | $0.23^{+0.04}_{-0.04}$ | $0.21^{+0.03}_{-0.03}$ | $0.24^{+0.03}_{-0.03}$ |
| | 0.05 | $0.18^{+0.09}_{-0.09}$ | $0.12^{+0.12}_{-0.12}$ | $0.12^{+0.12}_{-0.12}$ | $0.06^{+0.06}_{-0.06}$ | $0.08^{+0.04}_{-0.04}$ | $0.05^{+0.03}_{-0.03}$ | $0.04^{+0.03}_{-0.02}$ | $0.04^{+0.02}_{-0.02}$ | $0.05^{+0.01}_{-0.01}$ |
| | 0.01 | $0.00^{+0.00}_{-0.00}$ | $0.00^{+0.00}_{-0.00}$ | $0.00^{+0.00}_{-0.00}$ | $0.00^{+0.00}_{-0.00}$ | $0.00^{+0.00}_{-0.00}$ | $0.02^{+0.02}_{-0.02}$ | $0.00^{+0.00}_{-0.00}$ | $0.01^{+0.01}_{-0.01}$ | $0.00^{+0.00}_{-0.00}$ |

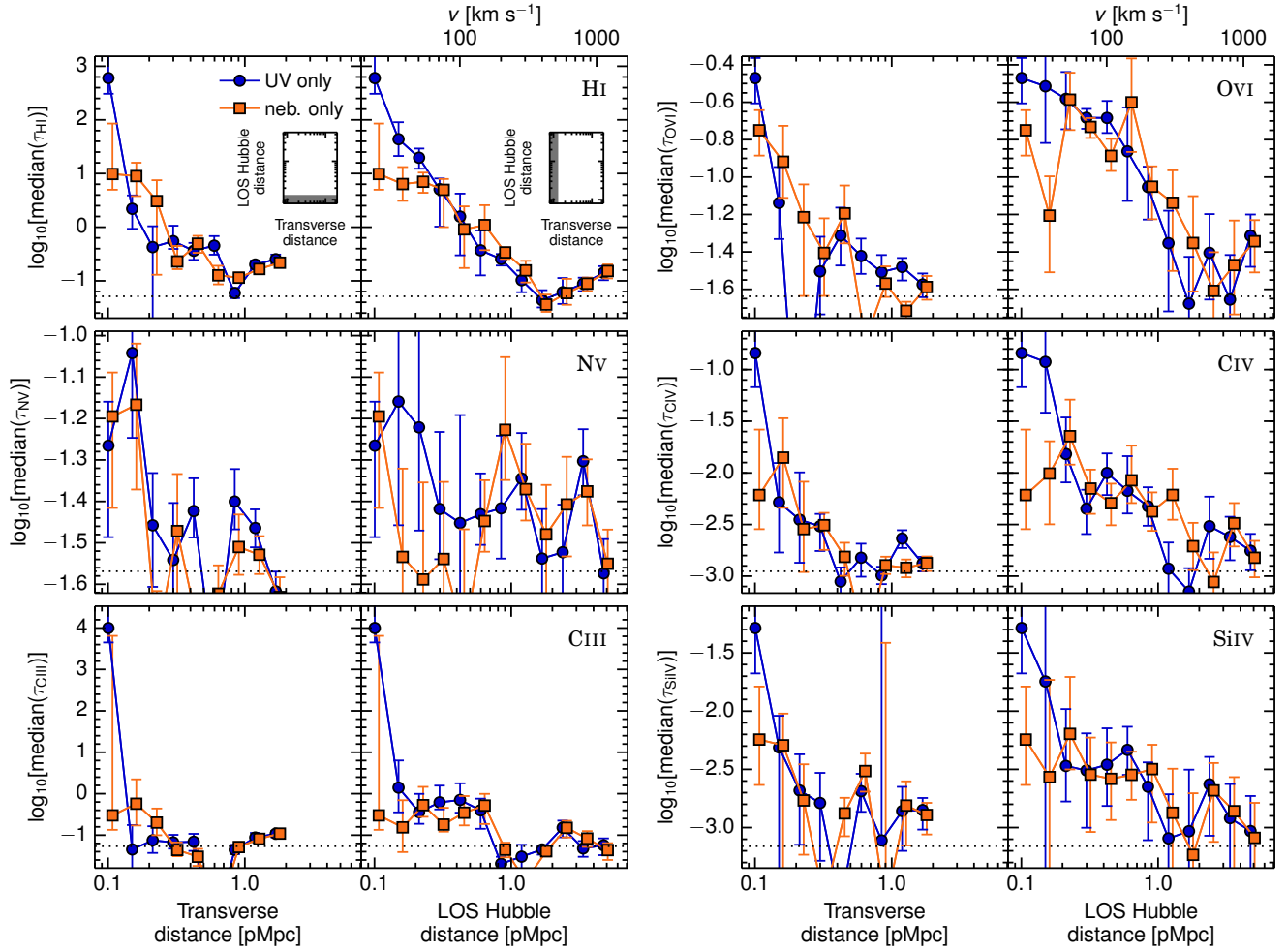


Figure D1. As Figure 12, but for the same 238 galaxies, using either their redshifts measured from rest-frame UV features (blue circles) or from nebular emission lines (orange squares). Except for the first bin of CIV, there are no significant differences between the results based on nebular and rest-frame UV redshifts.

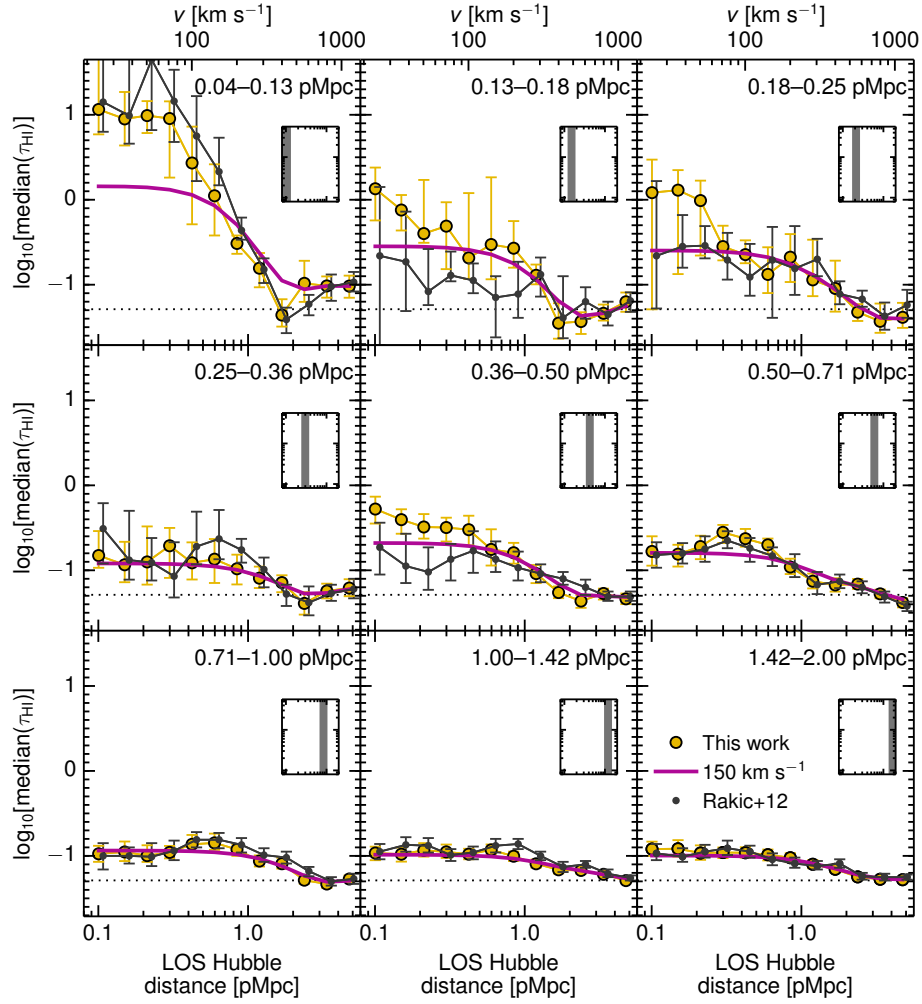


Figure D2. Cuts along the LOS through the unsmoothed HI map from Figure 4 (using the values from Table 5), where each panel shows a different transverse distance bin as denoted by the label and shown by the inset. The yellow circles show the data from this work, and the magenta lines give the values after smoothing with a $\sigma = 150 \text{ km s}^{-1}$ Gaussian, to mimic the effect of larger redshift errors. For comparison, we display the points from Figure 6 and Table 2 of Rakic et al. (2012), whose galaxy sample only had 10% nebular redshifts. Although we find no difference between the two data sets in the first panel (0.04–0.13 pMpc), the second and third panels (0.13–0.18 and 0.18–0.25 pMpc) show that the results from Rakic et al. (2012) are consistent with the current data after convolution with 150 km s^{-1} redshift errors.